TUDelft

Delft University of Technology

Selective Electrocatalytic CO2 Conversion on Metal Surfaces

Ma, Ming

DOI

10.4233/uuid:8b16b984-197d-4486-a139-02cbf9b80e69

Publication date
2017

Document Version
Final published version

Citation (APA)
Ma, M. (2017). *Selective Electrocatalytic CO2 Conversion on Metal Surfaces*. [Dissertation (TU Delft), Delft University of Technology]. https://doi.org/10.4233/uuid:8b16b984-197d-4486-a139-02cbf9b80e69

Important note
To cite this publication, please use the final published version (if applicable).
Please check the document version above.

Selective Electrocatalytic CO₂ Conversion on Metal Surfaces

Ming MA

Selective Electrocatalytic CO$_2$ Conversion on Metal Surfaces

Proefschrift

ter verkrijging van de graad van doctor

aan de Technische Universiteit Delft,

op gezag van de Rector Magnificus prof.ir. K.C.A.M. Luyben;

voorzitter van het College voor Promoties,

in het openbaar te verdedigen op

donderdag 14 september 2017 om 12:30 uur

door

Ming MA

Master of Science in Materials Science and Engineering,

China University of Petroleum

geboren te Shandong, China

This dissertation has been approved by the:

promotor: Prof. dr. B. Dam

copromotor: Dr. W. A. Smith

Composition of the doctoral committee:

Rector Magnificus	chairman
Prof. dr. B. Dam	Technische Universiteit Delft, promotor
Dr. W. A. Smith	Technische Universiteit Delft, copromotor

Independent members:

Prof. dr. M. T. M. Koper	Universiteit Leiden
Prof. dr. F. M. Mulder	Technische Universiteit Delft
Prof. dr. J. J. C. Geerlings	Technische Universiteit Delft
Dr. J. P. Hofmann	Technische Universiteit Eindhoven
Dr. C. Petit	Imperial College London

TUDelft

Cover design by Shenshen He

Table of Contents

1. Introduction

1.1 Background

The global atmospheric concentration of carbon dioxide (CO_2) has increased dramatically due to human activity, particularly after the industrial revolution. The accumulation of CO_2 (greenhouse gas) in the atmosphere is a serious environmental threat and a leading cause of global climate change.[1,2] The increased global mean temperature may trigger the rise of sea levels and the frequency and intensity of extreme weather events. In addition, the increase of the global CO_2 concentration has resulted in an increased ocean acidification,[3,4] leading to the demise of many natural habitats and aquatic species. The oceans are a principal sink for dissolving the anthropogenic CO_2 where it is estimated to have caused a rise of 30% in the concentration of H^+ in the ocean surface waters since the early 1900s, which may adversely affect many marine ecosystems in the near future.[4]

For mitigating the atmospheric CO_2 concentration, carbon capture and sequestration (CCS) at large emission sources such as industrial power plants has been proposed. However, there are some unknown ecological and environmental impacts and risks associated with the sequestration methods including geological and deep sea storage. Thus, carbon capture and utilization (CCU) could be a feasible strategy. For the utilization of the captured CO_2, the electrochemical reduction of CO_2 to fuels and value-added chemicals at mild conditions has attracted considerable attention as a promising solution.[5–10] In this process, the captured CO_2 could be utilized as a chemical feedstock and converted into carbon monoxide (CO), methane (CH_4), ethylene (C_2H_4), and even liquid products such as formic acid (HCOOH), methanol (CH_3OH) and ethanol (C_2H_5OH).[9–11] The high energy density hydrocarbons can be directly and conveniently utilized as fuels within the current energy infrastructure. In addition, the production of CO is very interesting since it can be used as a feedstock in the Fischer–Tropsch process, a well-developed technology that has been widely used in industry to convert syngas (CO and hydrogen (H_2)) into valuable chemicals such as methanol and synthetic fuels (such as diesel fuel).[5,6]

In order to avoid extra CO_2 emissions, the electrocatalytic reduction of CO_2 should be powered by electricity from renewable energy sources such as solar energy, hydropower and wind energy.[6,9] In this way, the anthropogenic carbon cycle can be closed by the conversion

of CO_2 into fuels and useful products (Figure 1.1). A key technological challenge for achieving this goal is to develop cheap and earth-abundant catalysts that are capable of electrochemically reducing CO_2 in cost-effective process with high efficiency, controllable selectivity and long-term stability.[5,9,12–14]
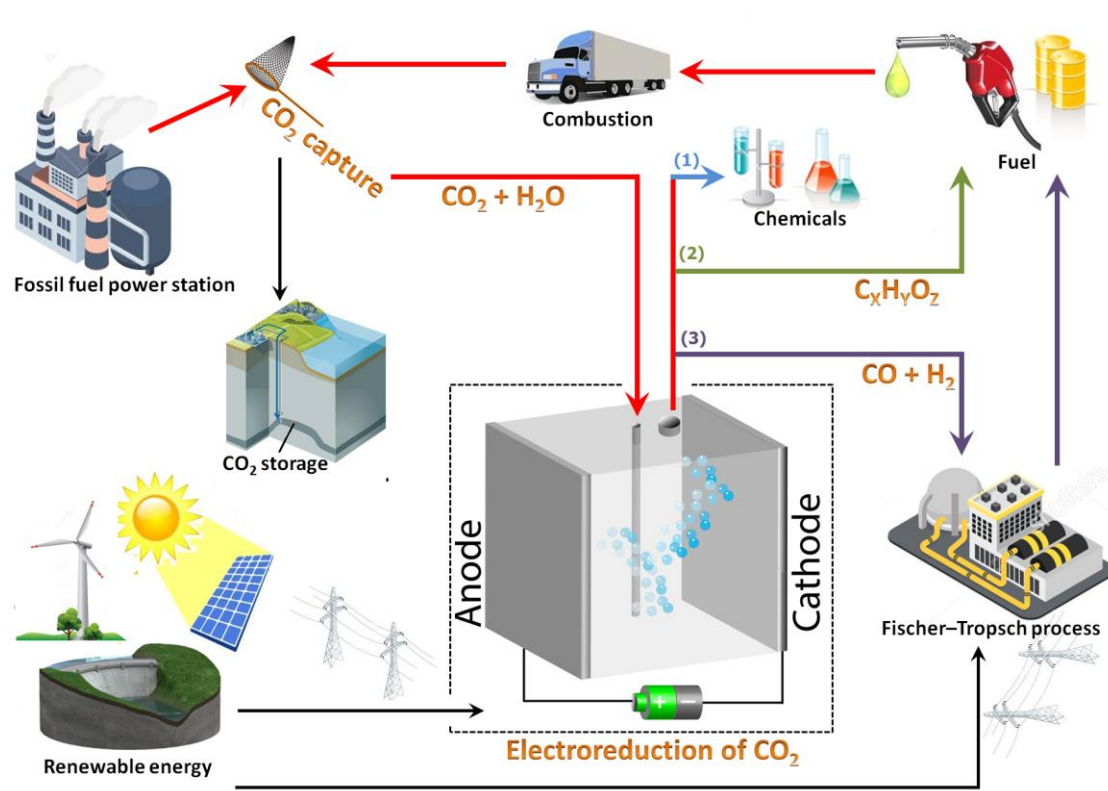
Figure 1.1 The carbon-neutral fuel production from electrochemical reduction of CO_2 powered with renewable energy sources such as solar energy, wind energy and hydropower, offers a promising route to close the anthropogenic carbon cycle. Three options of products via CO_2 conversion, (1) hydrocarbons such as C_2H_4, (2) Chemicals such as ethanol, (3) syngas for F-T process.

Hori and other researchers have extensively investigated the electrocatalytic reduction of CO_2 using various polycrystalline and monocrystalline metal electrodes in CO_2-saturated aqueous solutions to establish the catalytic activity and selectivity of certain metals for this conversion.[8,9,15–20] However, recent studies have focused on utilizing nanostructured metal catalysts, which have proven to have a significant effect on the catalytic selectivity, efficiency and stability in the electrochemical reduction of CO_2.[13,14,21–26] In addition, it has been demonstrated that the nanostructured surface contains more low-coordinated sites (edge sites and corner sites) which are more active for CO_2 reduction in comparison with a planar

metallic surface.[5,14,21,26–28] Thus, these nanostructured platforms offer a promising approach for selective and efficient CO_2 conversion, and are the main focus of this thesis.

A short review of recent developments of nanostructured metal catalysts for the electrocatalytic reduction of CO_2 is presented in this chapter, mainly focusing on the fabrication, characterization and catalytic performance of the nanostructured metal catalysts. In addition, the reaction mechanism of electrochemical CO_2 reduction on these nanomaterial-based catalysts reported previously is also introduced.

1.2 Transition Metal Catalysts for CO_2 Electroreduction

In the electrocatalytic CO_2 reduction process, CO_2 can be converted into many different products when combined with water on metal surfaces, and each product is formed by a different number of electrons at different equilibrium potentials. The electrochemical reduction of CO_2 to CO, CH_4, C_2H_4, HCOOH, CH_3OH and C_2H_5OH with their corresponding equilibrium potentials are given in the following reaction equations (all potentials are given with respect to the reversible hydrogen electrode (RHE)):
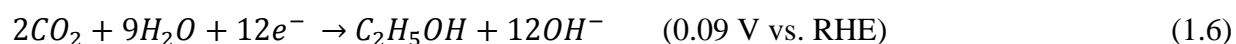
$$CO_2 + H_2O + 2e^- \rightarrow CO + 2OH^- \qquad \text{(-0.11 V vs. RHE)} \qquad (1.1)$$

$$CO_2 + H_2O + 2e^- \rightarrow HCOO^- + OH^- \qquad \text{(-0.03 V vs. RHE)} \qquad (1.2)$$

$$2CO_2 + 8H_2O + 12e^- \rightarrow C_2H_4 + 12OH^- \qquad \text{(0.08 V vs. RHE)} \qquad (1.3)$$

$$CO_2 + 6H_2O + 8e^- \rightarrow CH_4 + 8OH^- \qquad \text{(0.17 V vs. RHE)} \qquad (1.4)$$

$$CO_2 + 5H_2O + 6e^- \rightarrow CH_3OH + 6OH^- \qquad \text{(0.03 V vs. RHE)} \qquad (1.5)$$

$$2CO_2 + 9H_2O + 12e^- \rightarrow C_2H_5OH + 12OH^- \qquad \text{(0.09 V vs. RHE)} \qquad (1.6)$$

H_2 evolution is a competing reaction with CO_2 reduction in CO_2-saturated electrolytes. Thus, water could also be reduced to H_2 during CO_2 reduction according to the following reaction:

$$2H_2O + 2e^- \rightarrow H_2 + 2OH^- \qquad \text{(0 V vs. RHE)} \qquad (1.7)$$

According to the aforementioned reaction equations, it is important to note that the equilibrium potentials for each product formation are very close to that of hydrogen evolution (0 V vs. RHE), which indicates that it theoretically should not add a substantial amount of

extra potential to drive these reactions compared to simple water reduction. However, the practical potentials required for CO_2 reduction reactions are much more negative than the equilibrium ones, indicating that CO_2 reduction is generally more difficult to take place in comparison with H_2 evolution.[8]

To gain insights into the actual potentials required for electrochemical reduction of CO_2, it is critical to understand that numerous electron (or proton coupled electron) transfer steps are involved in the formation of these products. The number of electrons needed to drive each reaction is shown in Equation (1.1-1.7). The number of electrons required to form certain products generally scales with the increased amount of reaction intermediates, and thus the activation energy for each intermediate needs to be overcome to form the final product. Therefore, while the overall equilibrium potential for each product formation seems to be small and reasonable, the formation of multiple intermediates with electron transfer require highly negative potentials to proceed, resulting in much more negative potentials for overall CO_2 reduction in practice compared to the theoretical equilibrium potentials. Thus, based on experimental studies,[8,9,20] an overpotential of ~ 1 V is generally needed to drive the electrocatalytic reduction of CO_2 effectively and selectively in many practical cases. Notably, the actual required overpotentials for driving the reduction of CO_2 are strongly materials dependent.

Hori *et al.* has carried out electrochemical CO_2 reduction over various metal electrodes (Table 1.1) [8], discovering that several transition metal materials have the capability of reducing CO_2. It has been demonstrated that polycrystalline Ag and Zn show relatively high faradaic efficiency (FE) for the electrocatalytic reduction of CO_2 to CO, although these occur at high overpotentials. Au is the most efficient and selective metal surface for the electrocatalytic conversion of CO_2 into CO at a moderate overpotential, as presented in Table 1.1. In contrast, Ni, Pt, and Fe have a very low catalytic activity for CO_2 reduction, instead having a dominant selectivity towards hydrogen evolution. Notably, among the identified transition metals, Cu electrodes can uniquely catalyze the conversion of CO_2 into CH_4, C_2H_4, and alcohols at significant amounts in CO_2-saturated aqueous electrolytes at ambient pressure and temperature.[15,29]

The synthesis of products from CO_2 on metal catalysts is a complex multistep reaction with multiple adsorbed intermediates, most notably adsorbed CO.[10,30,31] The reaction mechanisms for the various products are attributed to the binding strength of intermediates (such as CO,

4

COH, CHO and CH_3) on the catalyst surface during the electrocatalytic reduction of CO_2.[32–34] The catalyst provides the reactive sites, and the product selectivity in the electrocatalytic reduction of CO_2 is influenced by whether the reactants and other related species are adsorbed at the active sites. Au, Ag and Zn exhibit a high faradaic efficiency for reduction of CO_2 to CO due to surface of these metals bind CO weakly.[35] In addition, this weak binding strength of CO also lead to the observation of the fact that further reduction of the CO intermediate to more complex products is rare on Au, Ag and Zn catalysts.[11,35] In contrast, the very strong binding of CO on Ni, Pt and Fe metallic catalysts limits the desorption of CO,[11,35] which implies that the coverage of CO adsorbed on Ni, Pt and Fe blocks the reactive sites for CO_2 reduction, resulting in the suppressed catalytic activity for CO_2 reduction with dominant H_2 evolution, as shown in Table 1.1. Cu, with a moderate CO binding energy, shows a total of 16 different CO_2 reduction products.[9]

Table 1.1 Faradaic efficiencies of products on various metal surfaces in CO_2 reduction at room temperature. Electrolyte: CO_2-saturated 0.1 M $KHCO_3$.[8]

Electrode	V vs. SHE	Faradaic Efficiency (%)							
		CH_4	C_2H_4	Ethanol	n-propanol	CO	HCOOH	H_2	Total
Au	-1.14	0	0	0	0	87.1	0.7	10.2	98.0
Ag	-1.37	0	0	0	0	81.5	0.8	12.4	94.6
Zn	-1.54	0	0	0	0	79.4	6.1	9.9	95.4
Pd	-1.20	2.9	0	0	0	28.3	2.8	26.2	60.2
Ga	-1.24	0	0	0	0	23.2	0	79.0	102.0
Pb	-1.63	0	0	0	0	0	97.4	5.0	102.4
Hg	-1.51	0	0	0	0	0	99.5	0	99.5
Tl	-1.60	0	0	0	0	0	95.1	6.2	101.3
In	-1.55	0	0	0	0	2.1	94.9	3.3	100.3
Sn	-1.48	0	0	0	0	7.1	88.4	4.6	100.1
Cd	-1.63	1.3	0	0	0	13.9	78.4	9.4	103.0
Cu	-1.44	33.3	25.5	5.7	3.0	1.3	9.4	20.5	103.5
Ni	-1.48	1.8	0.1	0	0	0	1.4	88.9	92.4
Fe	-0.91	0	0	0	0	0	0	94.8	94.8
Pt	-1.07	0	0	0	0	0	0.1	95.7	95.8
Ti	-1.60	0	0	0	0	0	0	99.7	99.7

1.3 Nanostructured Metal Catalysts for CO_2 Electroreduction

Catalytic behavior is not only strongly materials-dependent, but also extremely morphology-dependent.[36] The development of nanoscience research provides the opportunity to produce catalysts with controlled morphology such as size and shape, which has led to the discovery of the altered or enhanced catalytic activity that is related to the size and shape of nanostructured catalysts. Researchers have demonstrated that a nanostructured catalyst can exhibit very different behavior compared to its bulk counterpart, and thus much work in the field has focused on the elucidation of the effects of the nanostructured catalysts.

One of the main advantages of using metal nanocatalysts is that nanostructured catalysts are capable of providing more active sites (low-coordinated sites such as edge sites and corner sites) on the high surface area compared to bulk metal catalysts.[21,27] The increased active surface sites on nanocatalysts may cause an enhanced catalytic performance due to the fact that the catalytic activity is proportional to the number of the active surface sites.[21] In addition, the catalytic stability of the electrochemical reduction of CO_2 has been improved on nanostructured catalysts, which can be attributed to the enhanced tolerance to heavy metal impurities in an electrolyte. Hori has demonstrated that unavoidable ppm concentration of heavy metal impurities (such as Fe or Pb) in the electrolytes can be reduced and deposited on the cathodic electrode surface, which could poison a flat catalyst, resulting in a significant influence in the electrocatalytic activity for CO_2 reduction.[8] The large surface area of nanostructured electrocatalysts could adapt the contamination or impurities, having a better catalytic stability.[21]

1.3.1 Nanostructured Metal Catalysts for the Electrochemical Reduction of CO_2 to CO

While several electrocatalyst materials such as Au, Ag and Zn are capable of reducing CO_2 to CO in CO_2-saturated aqueous solutions at ambient temperature and pressure,[8][17] all suffer from one or more of the following problems: high overpotential needed to drive the reaction at a sufficient rate, low current density and rapid deactivation of CO_2 reduction activity in favor of H_2 evolution.[13] The main challenge for the electrochemical production of CO is the development of electrocatalysts that are capable of reducing CO_2 to CO efficiently and selectively at low overpotential over a long period of time.

1.3.1.1 Nanostructured Au Electrocatalysts

Au Nanoparticles

Min *et al.*[37] reported the electrocatalytic CO_2 conversion to CO by nanostructured gold catalysts deposited on carbon papers by an e-beam evaporator using an Au pellet (99.99%) source. The morphology of deposited Au was observed to vary from the small nanoparticles (NPs) to aggregated clusters to layered film (Figure 1.2). The CO faradaic efficiency and production rate were found to increase with increasing the Au amount. The FE for CO formation reached the saturation point at samples thicker than Au-4 (Au-4 represents that Au amount corresponds to 4 nm thick Au film), which is comparable with a commercial Au foil. In addition, Nam *et al.*[38] synthesized a concave rhombic dodecahedron (RD) gold nanoparticle by using 4-aminothiophenol as an additive and demonstrated that this concave RD had a superior electrocatalytic performance for reduction CO_2 to CO in CO_2-saturated aqueous solutions. For instance, concave RD achieved a FE of approximately 52% for CO formation at a potential of -0.26 V vs. RHE, which corresponds to an overpotential of 0.15 V relative to the CO_2/CO equilibrium potential (-0.11 V vs. RHE).
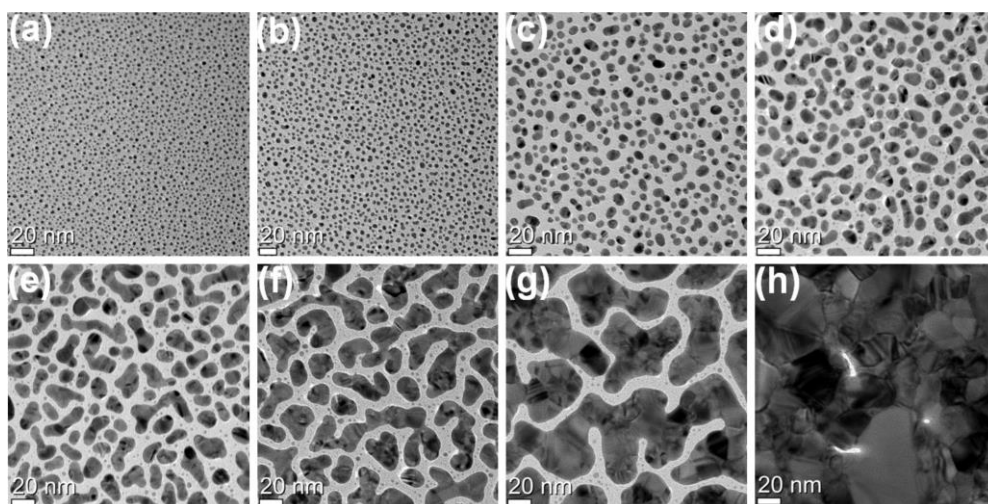
Figure 1.2 TEM images of Au samples. The morphology of Au surfaces changes as a function of Au coverages.[37]

Au clusters have also been explored by the combination of experimental and computational studies, providing insights into the electronic interactions between Au_{25} clusters and weakly bound adsorbates.[39] It was demonstrated that that the Au_{25} clusters performed as electrocatalysts for the electrochemical conversion of CO_2 into CO and exhibited the

reduction of CO_2 to CO could take place within an overpotential of 90 mV, which represents an approximate 200−300 mV reduction in potential compared to the larger Au NPs and bulk Au.
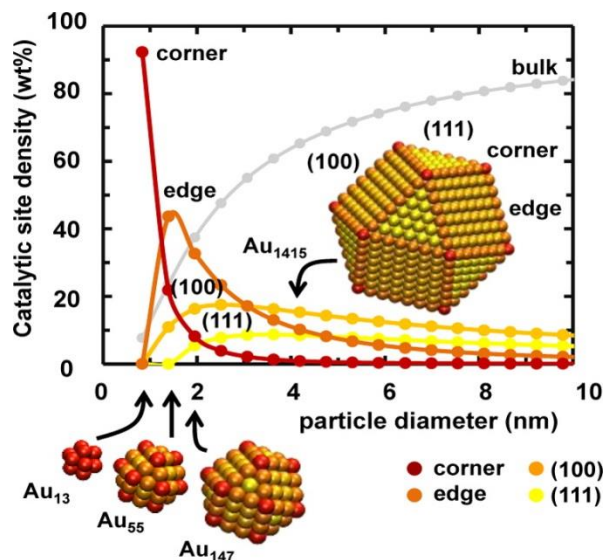
Figure 1.3 Density of adsorption sites ((001), (111), edge, or corner on-top sites are marked with light orange, yellow, dark orange, or red symbols represent, respectively) on closed-shell cuboctahedral Au clusters as a function of the cluster diameter. Gray dots represent the weight fraction of Au bulk atoms.[40]

Recently, Sun *et al.*[40] reported that the electrocatalytic reduction of CO_2 on Au NPs with a series of sizes (4, 6, 8 and 10 nm) in CO_2-saturated 0.5 M $KHCO_3$. The crystallite diameters of 4, 6, 8 and 10 nm NPs were estimated to be 2.0, 2.3, 4.0 and 5.9 nm, respectively. Among 4, 6, 8 and 10 nm Au NPs, the 8 nm NPs exhibited the highest selectivity for the reduction of CO_2 to CO (FE= 90% at -0.67 V vs. RHE). Density functional theory (DFT) calculations on different crystalline faces suggested that edge sites on Au NPs are active for CO formation while corner sites favor the competitive H_2 evolution reaction. To understand the size-dependent electroreduction of CO_2 on Au NPs, the correlation of the density of catalytically active surface sites and the cluster diameter was investigated, as shown in Figure 1.3. It was found that more edge sites than corner sites on the Au NP surface could facilitate the stabilization of $COOH^{\bullet}$ intermediate, resulting in the improved reduction of CO_2 to CO with suppressed H_2 evolution.

Au Nanowires

The previous study on monodispersed Au NPs indicated that the edge sites of Au NPs are favorable for the reduction CO_2 to CO while corner sites are active for the H_2 evolution.[40] Thus, a one-dimensional morphology may offer an abundance of edge sites which is preferred for the reduction of CO_2. Zhu *et al.*[41] demonstrated ultrathin Au nanowires (NWs) for the selective electrochemical reduction of CO_2 to CO. A facile seed-mediated growth method was developed to fabricate the ultrathin Au NWs by reducing $HAuCl_4$ in the presence of 2 nm NPs. These Au NWs were capable of catalyzing CO_2 to CO with FE of 94% at -0.35 V vs. RHE in CO_2-saturated 0.5 M $KHCO_3$. The modeling work (DFT) shows that the excellent catalytic performance for CO_2 reduction to CO on Au NWs is ascribed to a high edge-to-corner ratio in ultrathin Au NWs and the weak CO binding on these reactive edge sites.

1.3.1.2 Nanostructured Ag

Ag has attracted considerable attention as a catalyst for the conversion of CO_2 to CO due to its relatively low cost compared to Au and its high selectivity for CO_2 reduction.[8,11] It has been demonstrated (Table 1.1) that Ag foils are capable of electrochemically reducing CO_2 to CO with a high FE at a relatively smaller overpotential than other metallic counterparts (except for Au). Recently, Jaramillo *et al.*[20] investigated the catalytic activity and selectivity of the electrochemical reduction of CO_2 as a function of potential on metallic silver surfaces under ambient conditions, discovering that the applied potential can significantly influence the selectivity for the two major products (CO and H_2). Specifically, the optimal selectivity for CO formation on the silver electrodes was observed at the range from -1.0 to -1.2 V and hydrogen evolution dominated at very high and low overpotentials (Figure 1.4).

On Ag catalysts, the overpotential (> 0.9 V) required for driving the electrocatalytic reduction of CO_2 efficiently and selectively with suppressed H_2O reduction remains relatively high,[42] which is attributed to the hindrance for the initial electron transfer to a CO_2 molecule for CO_2 activation.[5,12,27,35] It has been demonstrated that the surface of nanostructured Ag catalysts offer low-coordinated surface sites, which are favorable for CO_2 fixation (to stabilize the $COOH^{\bullet}$ intermediate) through reducing the activation energy barrier of the initial electron transfer.[27]

In addition, Hori *et al.*[17] has investigated the electroreduction of CO_2 on single crystalline silver electrodes, showing that the CO_2 conversion to CO is favorable on Ag(110) compared to Ag(111) or Ag(100). Recently, a DFT simulation study (Figure 1.5) exhibited that Ag (110)

or Ag (211) surface has a lower free energy changes for the first proton-coupled electron transfer for $COOH^\bullet$ stabilization than Ag(111) or Ag(100), resulting in better catalytic activity for the reduction of CO_2 to CO on Ag(110) or Ag (211).[27] The authors believed that stepped Ag(110) or Ag (211) surfaces are much prevalent on the nanostructured Ag catalysts than that on bulk Ag electrodes.[27]
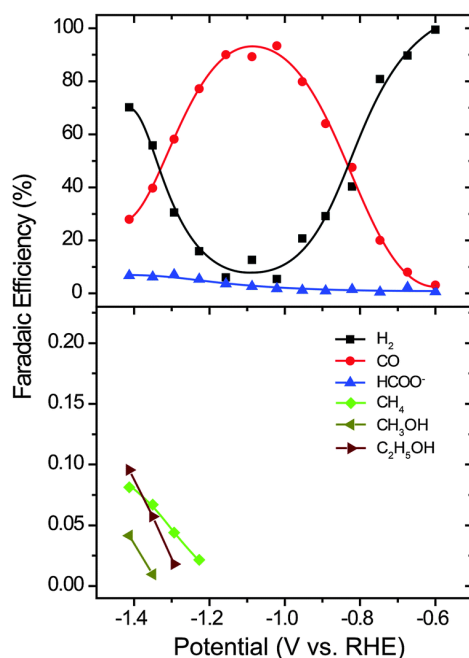
Figure 1.4 Faradaic efficiency of products on polycrystalline Ag foils at various potentials.[20]
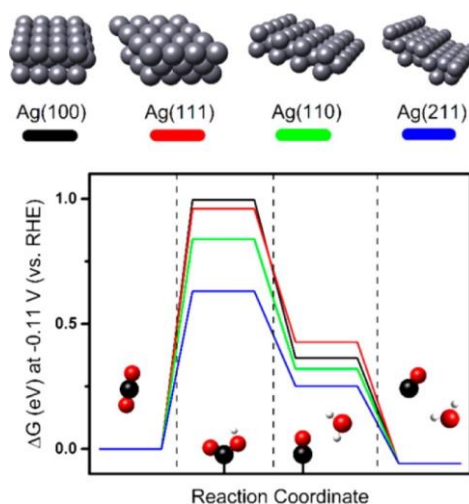
Figure 1.5 Free energy diagrams for the electrocatalytic conversion of CO_2 into CO on flat (Ag(100) and Ag(111)) and edge (Ag(221) and Ag(110)) surfaces at an applied potential of -0.11 V vs. RHE. A proton-coupled electron transfer is involved in the first two reaction steps. Sphere colors: black, C; red, O; white, H.[27]

Ag Nanoparticles

Recently Kim *et al.*[43] have examined silver NPs with different sizes for the electrocatalytic reduction of CO_2 in CO_2-saturated 0.5 M $KHCO_3$. Silver NPs with three different sizes (3 nm, 5 nm and 10 nm) were fabricated on carbon substrates, respectively, by a facile one-pot method using cysteamine as an anchoring agent. The authors discovered that immobilized Ag NPs supported on carbon had an increased FE and a lower overpotential for the selective reduction of CO_2 to CO. Notably, the particle size of 5 nm exhibited the highest catalytic activity for the selective reduction of CO_2 to CO. As shown in Figure 1.6b, a FE of 84.4% and a decrease of the overpotential by 300 mV were observed on NPs with diameter of 5 nm at −0.75 V vs. RHE compared to polycrystalline Ag foil. The DFT studies suggested that the specific interaction (Ag-S interaction) between Ag NPs and the anchoring agents modified the catalyst, inducing a selectively higher affinity to the COOH• intermediate, which effectively lowers the overpotential and improves the catalytic activity for the reduction of CO_2 to CO. In addition, for identifying the carbon source for the CO_2 reduction, a $^{13}CO_2$ isotope experiment was performed, confirming that the carbon source for CO formation completely originates from the dissolved CO_2 in electrolytes.
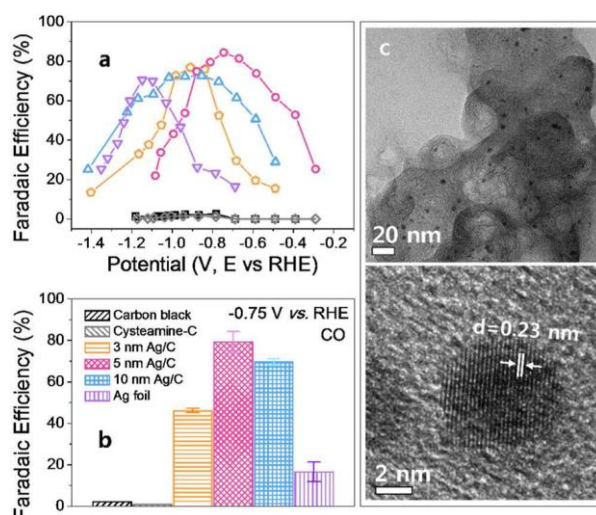
**Figure 1.6** Faradaic efficiency for CO formation in CO_2-saturated 0.5 M $KHCO_3$ (a) at various potentials and (b) at a fixed potential of −0.75 V vs. RHE. (c) TEM images of 5 nm Ag/C after the reduction of CO_2.[43]

A previous report[44] also evaluated the Ag NP size effect, revealing that the catalytic activity increases with decreasing particle size until a certain particle size with 5 nm, and that

the activity decreases with going to even smaller nanoparticle size (1 nm). This observation is consistent with the results from Kim (5 nm NPs offer the maximum catalytic activity for CO_2 reduction).

Nanoporous Ag

Lu *et al.*[5] reported that a nanoporous Ag catalyst, prepared by the de-alloying of an Ag-Al prescursor, is capable of reducing CO_2 electrochemically to CO with a high FE of > 90% at a moderate potential of -0.6 V vs. RHE in CO_2-saturated 0.5 M $KHCO_3$. To explore the electrokinetics of CO_2 reduction, Tafel analysis was performed on the nanoporous Ag catalysts and the polycrystalline Ag electrodes, respectively.
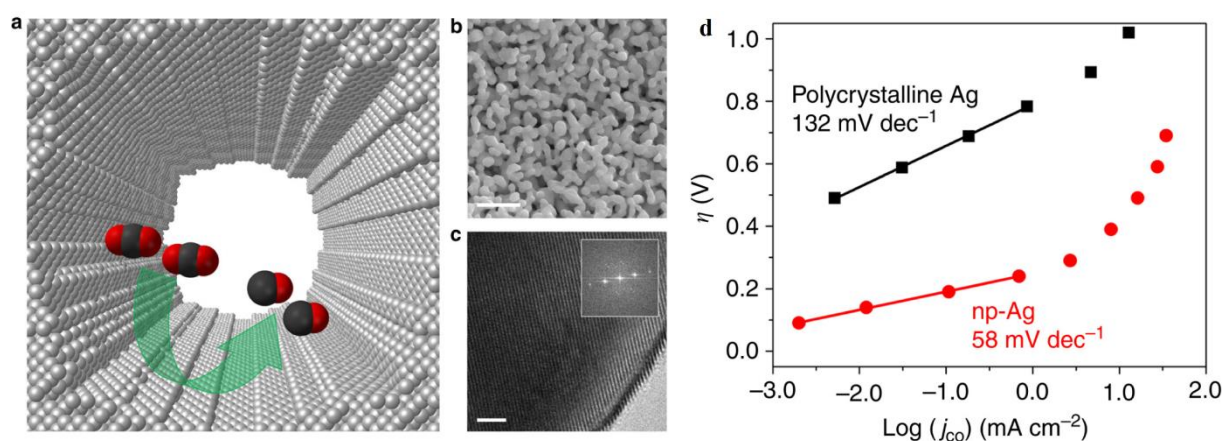
Figure 1.7 (a) A schematic diagram of a nanoporous Ag catalyst with highly curved internal surface. (b) SEM image of nanoporous Ag (scale bar represents 500 nm). (c) Corresponding high-resolution TEM image with visible lattice fringes (scale bar, 2 nm). (d) Tafel plots of the partial current density for CO production.[5]

It is known that a two electron-transfer process is involved in the electroreduction of CO_2 to CO on Ag catalysts. Firstly, one electron is transferred to a CO_2 molecule to produce a $CO_2^{\bullet-}$ intermediate, and then one proton is coupled to form a $COOH^\bullet$ intermediate. Subsequently, the $COOH^\bullet$ intermediate takes another electron and one proton, resulting in the CO formation on catalyst surface. The initial electron transfer to a CO_2 molecule is the rate determining step for the overall process because the first electron transfer requires a much more negative potential compared to the following steps.[5,12,27,35] A Tafel slope of 132 mV/dec for polycrystalline Ag shown in Figure 1.7d indicates that the rate determining step is the initial electron transfer to CO_2 for the formation of the $CO_2^{\bullet-}$ adsorbed on polycrystalline Ag. In contrast, nanoporous Ag with a Tafel slope of 58 mV/dec reveals a fast initial electron-

transfer step, suggesting that a better stabilization for $CO_2^{\bullet-}$ intermediate on nanoporous-Ag in comparison to the polycrystalline Ag. This study directly shows a clear advantage of CO_2 reduction catalysis on nanostructured electrodes.

1.3.1.3 Nanostructured Zn

Zn is an earth-abundant material, which is roughly 3 orders of magnitude more abundant in the Earth's crust than Ag. Hori et al.[8] reported that polycrystalline Zn electrodes are capable of catalytically reducing CO_2 to CO with a FE of 79.4%. However, Zn electrodes require a relatively higher overpotential for driving CO_2 reduction selectively in comparison with Au and Ag (Table 1.1).
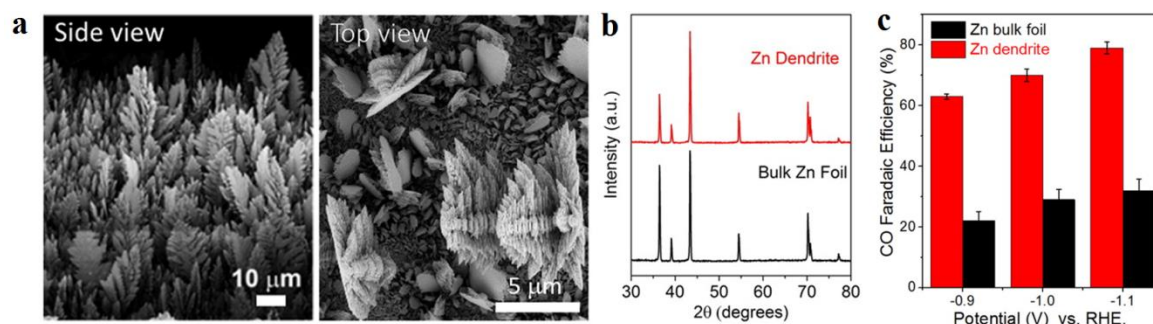
Figure 1.8 (a) SEM image for a Zn dendrite catalyst. (b) XRD patterns of dendritic and bulk Zn electrodes. (c) CO selectivity for bulk and dendritic Zn electrodes.[45]

Nanostructured Zn with more active sites may offer better catalytic performance for CO_2 reduction. Thus, nanostructured Zn dendrite electrodes were synthesized on Zn foil electrodes using an electrochemical Zn deposition.[45] As shown in Figure 1.8a, the scanning electron microscope (SEM) images reveal that the dendrite layer was about 50-100 μm thick and uniformly deposited on Zn foils. The X-ray diffraction (XRD) patterns in Figure 1.8b show that all the diffraction peaks of the nanostructured Zn dendrite and the Zn bulk foil are aligned precisely, indicating a pure metallic Zn. This nanostructured Zn dendrite catalyst was able to electrochemically reduce CO_2 to CO in an aqueous bicarbonate electrolyte, with a CO selectivity of around 3-fold higher than that of bulk Zn counterparts, as displayed in Figure 1.8c.

1.3.1.4 Oxide-Derived Metal Nanocatalysts

In order to improve the electrocatalytic CO_2 reduction performance, an interesting method of preparing catalysts through the electrochemical reduction of metal oxides was recently proposed. In the process, the bulk metal is firstly oxidized, and then the metal oxide layer is directly utilized in the electrochemical CO_2 reduction in CO_2-saturated electrolytes, reducing to metallic nanocatalysts during electrolysis. The recent development and progress of these oxide-derived (OD) catalysts are introduced in the following section.

Oxide–Derived Cu

Kanan *et al.*[14] demonstrated the electrochemical reduction of CO_2 on a metallic Cu catalyst resulting from the reduction of thick Cu_2O films prepared by annealing Cu foil in air. This sample formed by the electroreduction of a Cu_2O layer during the CO_2 reduction electrolysis was analyzed by XRD and XPS, indicating the complete reduction of the copper oxide layer. By systematically varying the original annealing temperature and time, it was found that annealing the Cu foil in air at 500 ºC for 12 hours results in a thick Cu_2O layer, which then forms a nanostructured Cu (OD-Cu) during electrocatalysis that are able to produce CO with ~ 40% FE and HCCOH with ~ 33% FE at -0.5 V vs. RHE (Figure 1.9a,b). Notably, the selectivity for CO (~ 40% FE) was maintained during the whole electrolysis of 7 hours, revealing a dramatically improved catalytic stability for CO_2 reduction on OD-Cu. As shown in Figure 1.9b, the OD-Cu exhibited a high FE for CO_2 reduction at much lower overpotential compared to the bulk Cu electrodes. The Tafel slope of ~ 116 mV/dec for OD-Cu in the low overpotential range (Figure 1.9c) indicates the Cu formed by electrochemical reduction of Cu_2O during electrolysis is in favor of the formation of $CO_2^{\bullet-}$ intermediate.
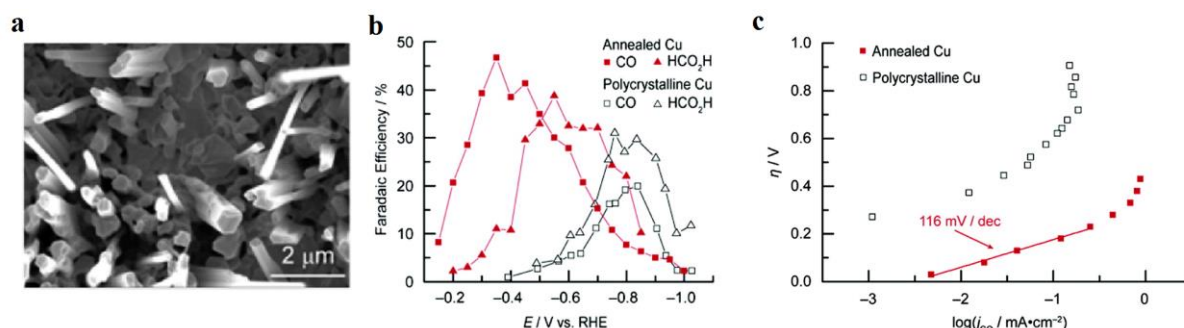
Figure 1.9 (a) SEM image of oxide-derived Cu. (b) Faradaic efficiencies for CO and HCOOH as a function of potential. (c) Tafel plots of CO partial current density for polycrystalline Cu and oxide-derived Cu.[14]

Furthermore, Kas *et al.*[23] investigated the electrocatalytic CO_2 reduction on copper NPs derived from different orientation of electrodeposited Cu_2O ([110][111][100]). The authors reported that the initial crystal orientation of Cu_2O had a minor effect on the catalytic selectivity for CO_2 reduction. However, it was found that the thickness of the initial Cu_2O layer strongly influenced the product selectivity, which is consistent with the previous study on OD-Cu.[14]

The electrochemical reduction of CO_2 into fuels such as hydrocarbons on Cu catalysts is a complex multistep reaction with adsorbed intermediates, most notably adsorbed CO. Thus, CO reduction activity was investigated on OD-Cu, producing liquid products (ethanol, acetate and n-propanol) with nearly 50% FE at moderate potentials.[46] In order to correlate a particular structural feature of oxide–derived Cu with the catalytic activity, the authors proposed that the Cu catalysts electrochemically reduced from copper oxide may obtain a high density of grain boundary surfaces, likely resulting in a highly active sites for CO_2 reduction.[46] A temperature-programmed desorption (TPD) of CO was utilized to probe the surface chemistry of OD-Cu, revealing a high CO reduction activity on OD-Cu is linked to the active sites that bond CO more strongly in comparison with low-index and stepped Cu facets.[47] It was proposed that the strong binding sites with CO are supported by grain boundaries on the OD-Cu, which are only accessible in this nanostructured platform.

Oxide–Derived Au

Similar to the OD-Cu, OD-Au nanocatalysts were also studied for CO_2 reduction.[13] Initially, the Au oxide layers were prepared on Au foil electrodes by applying periodic square-wave pulsed potentials in 0.5 M H_2SO_4. After the pulsed anodization on Au, the Au oxide layers were formed on Au foils.

The Au oxide layers on Au foils were directly utilized for CO_2 reduction in CO_2-saturated electrolytes and were electrochemically reduced to metallic Au at the beginning of electrolysis (Figure 1.10a shows the SEM images of the oxide-derived Au). The significant distinct electrocatalytic activity of CO_2 reduction between OD-Au and polycrystalline Au was observed at low overpotentials, as shown in Figure 1.10b. At a low overpotential of 0.24 V, the FE for CO formation was maintained at ~96% over the course of an 8 hour electrolysis experiment. Furthermore, the Tafel slope of 114 mV/dec (Figure 1.10b) on polycrystalline Au indicates the rate-determining step is the initial electron transfer to form an adsorbed $CO_2^{\bullet-}$

intermediate (Scheme 1.1). The poor stabilization of $CO_2^{\bullet-}$ intermediate is correlated with the high overpotential required on polycrystalline Au. In contrast, the active sites on OD-Au nanocatalysts offer the fast initial electron transfer (low Tafel slope in Figure 1.10b), which results in the dramatically enhanced stabilization of $CO_2^{\bullet-}$ intermediate. In addition, the HCO_3^- concentration dependence studies on OD-Au showed an increase in the CO partial current density with gradually increasing the $NaHCO_3$ concentration, implying that the first proton donation from HCO_3^- is a rate determining step on OD-Au (Scheme 1.1). Furthermore, a study on grain boundary effect showed that the catalytic activity for electroreduction of CO_2 is linearly correlated with the grain boundary density on prepared Au NPs and the high density of grain boundaries on OD-Au was thought to be linked to its catalytic performance.[48]
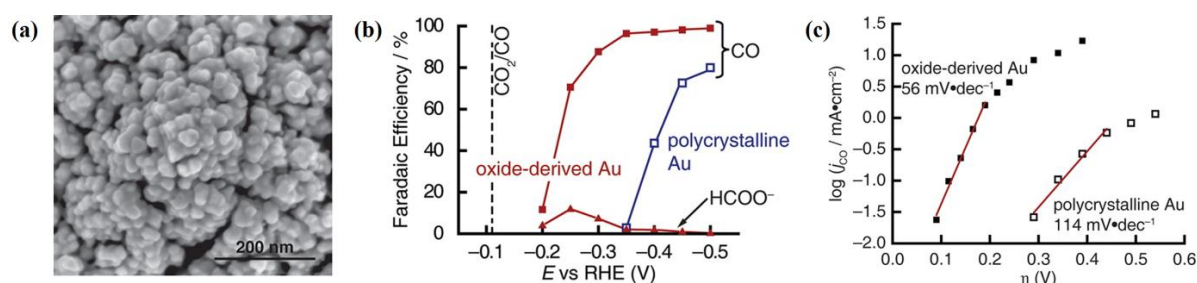
Figure 1.10 (a) SEM image of oxide-derived Au NPs. (b) Faradaic efficiencies for CO and HCOOH, and (c) Tafel plots of CO partial current density of oxide-derived Au NPs and polycrystalline Au.[13]
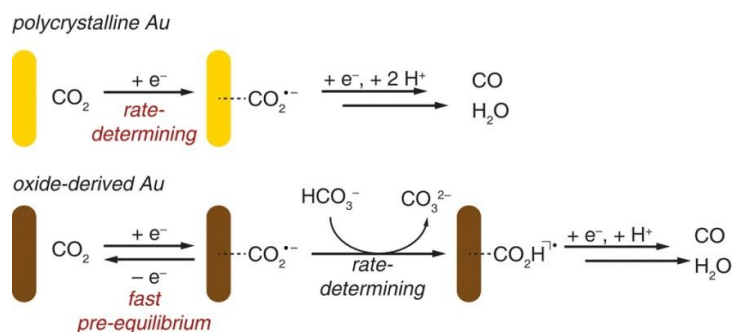
Scheme 1.1 Proposed mechanisms for the electroreduction of CO_2 to CO on polycrystalline Au and oxide-derived Au, respectively.[13]

1.3.2 Nanostructured Metal Catalysts for CO$_2$ Reduction to Hydrocarbons

The conversion of CO_2 and H_2O to hydrocarbons on electrocatalysts has attracted considerable attention recently.[9,13,14,22] The main advantages of directly forming hydrocarbons are their high energy density and the ease of utilization as fuels in our existing

energy infrastructures. However, a major challenge of this goal is to develop electrocatalysts that are capable of reducing CO_2 efficiently and selectively at low overpotentials. Hori and coworkers carried out CO_2 reduction over various metal electrodes (Table 1.1), and it was demonstrated that many electrocatalyst materials such as polycrystalline Cu, Au, Ag and Zn show high FE for the electrochemical reduction of CO_2, although these occur at very high overpotentials.[8] Notably, it was found that copper electrodes can uniquely reduce CO_2 to significant amounts of CH_4, C_2H_4, and alcohols in aqueous electrolytes at ambient pressure and temperature.[15,29] One main reason for this unique catalytic activity of copper is attributed to the appropriate binding strength of intermediates (such as -CO, -COH, -CHO and -CH_3,) on the copper surface during the electrochemical reduction of CO_2.[32–34]

Recently, Jaramillo *et al.*[9] reported new insights into the electrocatalytic reduction of CO_2 on metallic Cu surface, finding as many as 16 different products from the electroreduction of CO_2 (five of them have never been reported previously). At low potential of < -0.75 V vs. RHE, only H_2, CO and HCOOH were detected on Cu. At -0.75 V vs. RHE, C_2H_4 and CH_4 formation started to be observed. In addition, other C_2 and C_3 products were initially detectable at -0.95 V vs. RHE.

Until now, Cu is the only known material with capability of electrocatalytically converting CO_2 into significant amounts of hydrocarbons at high reaction rates in aqueous solutions at ambient conditions of temperature and pressure.[9,23,49] However, controlling the selectivity of the CO_2 reduction and reducing CO_2 effectively at low overpotential with high current density for the formation of hydrocarbons is a major scientific challenge for the practical use of this technology.[12–14,46] It has been demonstrated that the surface morphology and roughness of copper electrodes have a dramatic influence on the catalytic activity and product selectivity for the electrochemical reduction of CO_2 in an aqueous solution.[14,22–25]

1.3.2.1 Cu nanoparticles

Tang *et al.*[25] reported that Cu nanoparticle covered electrodes exhibited a better selectivity towards C_2H_4 and CO formation in comparison with an electropolished Cu electrode and an argon gas sputtered Cu electrode. In that study, the increased catalytic selectivity for C_2H_4 formation in CO_2 reduction performance was explained by the roughened Cu surface which was able to provide a greater abundance of undercoordinated sites. Alivisatos *et al.*[50] have demonstrated that Cu NPs supported on glassy carbon (n-Cu/C) exhibited a 4-fold higher

methanation current densities compared to the high-purity Cu foil counterpart. A FE of 80% for CH_4 was achieved on the n-Cu/C electrocatalysts. The rate-limiting step for CH_4 on Cu foils is a single electron transfer to CO_2 for CO_2 activation, which corresponds to a Tafel slope of 120 mV/dec. The Tafel slope for CH_4 is 60 ± 4.2 mV/dec on the n-Cu/C, which is consistent with the theoretical value of 59 mV/dec, revealing that the methanation process is involved with a one-electron transfer for CO_2 activation followed by a rate-limiting non-electrochemical step for CH_4 formation.
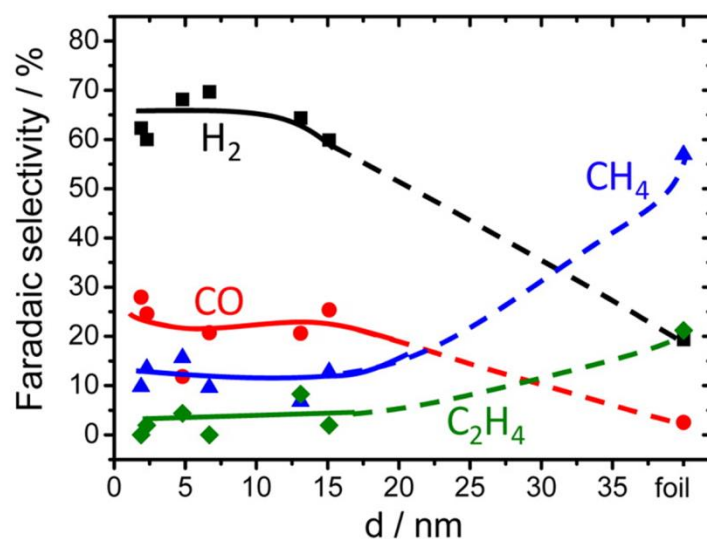
Figure 1.11 Faradic selectivity of reaction products during the CO_2 electroreduction on Cu NPs in CO_2-saturated 0.1 M $KHCO_3$ at -1.1 V vs. RHE under 25 °C.[22]

Recently, the particle size dependence for the electrochemical reduction of CO_2 has been investigated on Cu NPs with the size range from 2 to 15 nm.[22] Cu NPs exhibited that an increase in the catalytic activity and selectivity for CO and H_2 with decreasing Cu particle size, as presented in Figure 1.11. In addition, catalytic selectivity for hydrocarbons (CH_4 and C_2H_4) was suppressed on nanoscale Cu surface compared to the bulk Cu foil. To gain insight into the Cu particle size effect, the atomic coordination of model spherical Cu particles from 1 to 18 nm was utilized, suggesting low-coordinated sites and the strong chemisorption are linked to the acceleration for H_2 evolution and the CO_2 reduction to CO.

1.3.2.2 Cu nanofoam

Sen *et al.*[24] investigated the electrochemical reduction of CO_2 over copper foams with hierarchical porosity. Three-dimensional foams of copper were electrodeposited onto mechanically polished copper substrates. SEM images of copper foams prepared at different amounts of electrodeposition time are shown in Figure 1.12. The electrocatalytic studies exhibited that the copper nanofoams are capable of reducing CO_2 to HCOOH, H_2, and CO as major products along with small amounts of C_2H_4, C_2H_6, CH_4, and propylene (C_3H_6), which indicates a distinct product distribution (C_2H_6 and C_3H_6 were not observed on smooth copper) in comparison with the smooth copper. The authors thought that these differences are attributed to high surface roughness, hierarchical porosity, and confinement of reactive species. In addition, it was observed that a gradual increase in the thickness the copper nanofoams with increasing electrodeposition time enhanced the FE of HCOOH formation by suppressing the electrochemical reduction of adsorbed $H^{\bullet}$ to H_2.
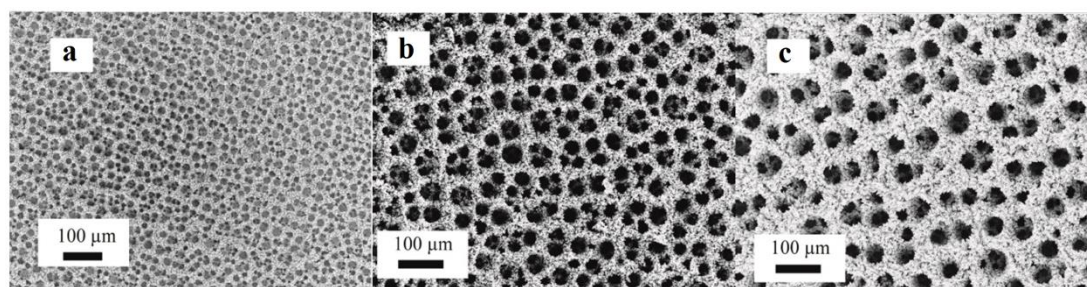
Figure 1.12 SEM images of electrodeposited copper foams on copper substrates for (a) 10s; (b) 15s; (c) 30s.[24]

1.4 Bimetallic catalysts

Great efforts have been devoted to the developments of nanostructured metal electrocatalysts for selective and efficient CO_2 reduction due to the fact that the nanostructured surface contains more edge sites and corner sites that are active for CO_2 reduction.[5,14,21,26–28] However, the currently developed electrocatalysts based on the strategy of nanostructuring materials still cannot meet the requirements for practical applications of CO_2 reduction. Recently, developing the bimetallic alloy electrocatalysts has attracted considerable attention as an alternative and promising strategy for dramatically improving the catalytic activity and selectivity of CO_2 reduction.[51–57]

CO_2 can be electrochemically reduced to CO, HCOOH, and hydrocarbons on metal electrodes in aqueous solution. During this process, electrode surfaces provide the active sites

for CO_2 conversion reaction, and the reactants and the formation of intermediates adsorbed on the surfaces play an important role in the formation of final products in the electrocatalytic CO_2 reduction. Therefore, it is important to know the binding energies of different reaction intermediates on the surface of different metals. Table 1.2 shows a comparison of the binding strength of CO_2 reduction intermediate species on FCC (111) single metal electrodes (adapted from ref.30). The product distribution and selectivity of CO_2 reduction could be influenced by whether or not the related intermediates are adsorbed. Alloying two different metals could change the binding energies of intermediates on the metal surfaces in the electrocatalytic CO_2 reduction, which significantly influences the catalytic activity and selectivity in CO_2 reduction. Practically, bimetallic catalysts have been proven to be effective in reducing overpotentials, and improving selectivity of materials. Below, the recent progress on alloy electrocatalysts, predominantly on nanostructured materials, is introduced.

Table 1.2 Comparison of the binding strength on FCC(111) transition metal facets[58].

Species on FCC(111) transition metal facets	Binding strength
*CO	Rh > Pd > Ni > Pt > Cu > Au > Ag
*COH	Rh > Pt > Pd > Ni > Cu > Au > Ag
*CHO	Rh > Pt > Pd > Ni > Au > Cu > Ag
*OCH$_3$	Ni > Rh > Cu > Ag > Pd > Pt > Au
*CH$_3$	Pt > Rh > Ni > Pd > Cu > Au > Ag

Table 1.3 Faradic efficiencies of main liquid products with different electrodes. [59]

Electrode	Faradaic Efficiency (%)	
	HCOOH	Alcohols (methanol and ethanol)
Bulk Cu	11.5	4.8
Nanostrucutred Cu	27.4	9.7
Cu$_{63.9}$Au$_{36.1}$/NCF	12.6	28
Cu$_{70.6}$Au$_{29.4}$/NCF	18.1	17.2
Cu$_{81.3}$Au$_{19.7}$/NCF	21.2	11.5

Electrocatalytic CO_2 reduction was performed on a nanostructured Cu-Au alloy prepared through electrochemical deposition with a nanoporous Cu film (NCF) as template, showing an improved catalytic selectivity for alcohols (methanol and ethanol).[59] The authors found that the FE for alcohols was dependent on the nanostructured morphology and composition of Cu-Au alloys, as shown in Table 1.3. In addition, the FE of 15.9% for methanol was detected on $Cu_{63.9}Au_{36.1}$/NCF, which was ~ 19 times higher than that of pure Cu.

Yang *et al.*[52] assembled monodisperse Au-Cu bimetallic NPs (Figure 1.13a) with different compositions by implementing the solvent evaporation-mediated self-assembly approach and then the nanoparticle monolayer was transferred onto a glassy carbon substrate for the electrocatalytic reduction of CO_2. With increasing the Cu content, different products were observed and the largest number in product distribution were found on pure Cu NPs. The authors believed the degree of stabilization of the intermediates on these nanoparticle surfaces can be tuned by varying the composition of Au-Cu bimetallic NPs, which results in the different final products (Figure 1.13b). Furthermore, the catalytic activity of these bimetallic catalysts was attributed to two factors: (1) the electronic effect on the binding strength of intermediates, which is linked to the change of electronic structure that is tuned with surface composition of the Au-Cu, and (2) the geometric effect that is correlated with the atomic arrangement at the active site that have a significant influence on the binding strength of intermediates.[60]
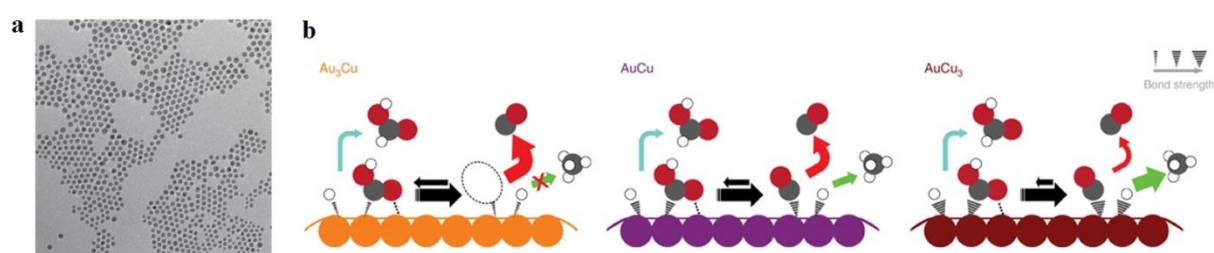
Figure 1.13 (a) TEM image of $AuCu_3$ NPs (scale bar, 100 nm). (b) Schematic illustration of the proposed mechanism for CO_2 reduction on the Au–Cu bimetallic NPs. Filled circles with grey, red and white color represent C, O and H, respectively. On the top right corner, the relative binding strength of intermediate is marked with the stroke weight. A dotted line indicates the additional binding between the COOH and the catalyst surface. Black horizontal arrows show the difference in probability of having COOH intermediate on different catalysts. The pathway towards each product is indicated by colored arrows (red: CO; blue: HCOOH; green: hydrocarbons).[52]

Electrochemical CO_2 reduction on Cu-In bimetallic alloys was evaluated.[51] A nanostructured Cu-In bimetallic alloy was prepared by the in-situ electrochemical reduction of Cu_2O in $InSO_4$ electrolytes, and it was found that the In incorporation exhibited an enhanced selectivity for the electroreduction of CO_2 to CO with high catalytic stability.[51] At potential from -0.3 V to -0.7 V vs. RHE, CO was generated on Cu-In alloy catalysts as almost the only products in CO_2 reduction, and notably a FE of ~ 90% for CO formation was achieved on the alloy catalysts at -0.5 V vs. RHE. A DFT study indicates that the incorporation of In may cause both local electronic effect and local geometric effect. The presence of In atoms has a significant effect on the binding energy of the associated intermediates adsorbed on Cu. After that, the dramatically enhanced FE for the conversion of CO_2 to CO is also achieved on nanostructured Cu-Sn bimetallic electrocatalysts at decreased overpotentials.[53]

Recently, a mesoporous nanostructured Cu-Pd bimetallic electrocatalyst was fabricated by an electrodeposition method for CO_2 reduction and Cu_3-Pd_7 exhibited a faradaic efficiency of more than 80% for selective CO formation at -0.8 V vs. RHE.[61] The mesoporous nanostructure has a roughened surface, which could offer more active sites for the selective reduction of CO_2 to CO. In addition, first principle calculation reveals that Pd atoms on the surface of the bimetallic catalysts act as reactive centers with an increased adsorption ability of CO_2 and COOH, and the presence of Cu could modify the CO desorption ability. The authors believed that the activity of the Cu-Pd binary catalysts is ascribed to the change of electronic structure of their neighboring element and adjustment of atomic arrangement in the active sites.

Koper *et al.*[62] have used bimetallic Pd-Pt NPs for the electrocatalytic CO_2 reduction. They found that Pd-Pt NPs had a low onset potential for the reduction of CO_2 to HCOOH, starting at 0 V vs. RHE for HCOOH formation, which is close to the theoretical equilibrium potential of producing HCOOH (equation (1.2)). In addition, the FE for HCOOH formation was dependent on the composition of the NPs and a high FE of 88% towards HCOOH formation was reached on Pd_{70}-Pt_{30} at an applied potential of -0.4 V vs. RHE.

Until now, most studies on the bimetallic catalysts for CO_2 reduction are nanostructured materials, which makes it difficult to distinguish the effects of binary composition and surface morphology. A better understanding of the catalytic activity of CO_2 reduction on bimetallic catalyst is essential for further improving the catalytic performance, and thus it is crucial to have a well-defined platform to distinguish these two factors for bimetallic catalysts.

1.5 Objectives of this thesis

According to the development and recent trends of the electrocatalytic CO_2 reduction on metallic catalysts (mentioned above in **Chapter 1**), nanostructured catalysts are capable of electrochemically reducing CO_2 with high selectivity and efficiency. It is generally accepted that nanostructured metal catalysts can offer an abundance of low-coordinated surface sites, which are active for certain intermediate formation (e.g. COOH$^{\bullet}$) by reducing the activation energy barrier in CO_2 reduction, resulting in the enhanced catalytic CO_2 reduction performance. In addition, the large surface area (roughened surface) provided by nanostructured catalysts is capable of adapting contamination and enhancing tolerance to heavy metal impurities, leading to a better catalytic stability in the CO_2 reduction on nanostructured catalysts in comparison with bulk counterparts.[21] All the above discussions reveal that the nanostructured catalysts are highly important for CO_2 reduction due to their high catalytic performance, and thus we initially aim to develop selective and efficient electrocatalysts for CO_2 reduction. Based on the developed high-performance electrocatalysts, a fundamental understanding of the reaction mechanism on nanostructured metallic catalysts is systematically investigated in this project.

pH is an important parameter that is associated with certain intermediates formation in the electroreduction of CO_2, and the formation and coverage of intermediates on metal electrodes could affect the reaction pathways that determine the final products.[63] The pH increases locally at the interface between electrode and electrolyte (thus, local pH > bulk pH), due to the OH^- formation in the cathodic reactions, as noted in equations (1-7). The effect of local pH near the catalyst surface on the catalytic selectivity of hydrocarbons has been proposed for the reduction of CO_2 on flat Cu foils by Hori,[64] which indicates that the electroreduction of CO_2 is sensitive to the local reaction environment. Highly nanostructured surface could alter the local environment significantly (local pH) due to the limitation of the diffusion process in nanostructure. However, there is no research about the systematic study on the effect of the local pH created in highly nanostructured catalysts on catalytic activity of CO_2 reduction. Herein, we aim to investigate the effect of local pH created in nanostructured catalysts on intermediates formation in certain reaction pathways and formation of final products by systematically tuning the nanostructured morphology.

Additionally, the interaction of two different metallic atoms in bimetallic alloys could significantly influence binding strength of intermediates which determines the catalytic activity for the electrocatalytic CO_2 reduction (**Chapter 1**). While some significantly

improved catalytic performance for the reduction of CO_2 has been made on the bimetallic alloy catalysts (as presented above), the fundamental understanding of the correlation of the binary composition with the catalytic activity is still unclear, which may limit the capability of rationally designing a bimetallic catalyst with facilitating certain intermediates formation that lead to highly selective and efficient CO_2 reduction for practical application. For a better understanding of the binary composition effect, we aim to build a well-defined platform for exploring the effect of binary composition on the binding strength of intermediates and the formation of final products by systematically varying the composition of bimetallic catalysts at a consistent surface morphology.

1.6 Thesis outline

Within this PhD project, all the following steps are taken for achieving the above objectives.

Chapter 2 presents a new and simple synthesis method to prepare a Cu nanowire array electrocatalyst for selective CO_2 reduction at room temperature and atmospheric pressure. This chapter contains two parts.

In the first part, the electrocatalytic reduction of CO_2 on the Cu nanowire (NW) arrays with fixed NW length and density was investigated at various potentials. It was found that the Cu NW array electrodes were able to convert CO_2 selectively into CO with a faradaic efficiency of 50% at a moderate overpotential of 0.49 V, which is dramatically higher than that of polycrystalline Cu electrodes. In addition, a study of the kinetics for CO_2 reduction on catalysts indicates a fast initial electron transfer for the CO_2 activation step on Cu NWs, which implies that the enhanced catalytic selectivity for the reduction of CO_2 to CO is linked to the better stabilization for the $CO_2^{\bullet-}$ intermediate on Cu NW arrays.

In the second part, Cu NW array electrodes with different length and density were controllably synthesized. The selectivity of hydrocarbon products (ethylene, n-propanol, ethane and ethanol) on Cu NW arrays was able to be tailored at a fixed potential by systematically varying the length and density of the Cu NWs. The morphology effect is correlated with a high local pH formed within the Cu NW arrays, and a detailed reaction mechanism for the local pH-induced formation of C_2 products via a favorable CO dimerization reaction pathway is presented in this chapter.

Chapter 3 describes the selective electrocatalytic reduction of CO_2 to CO on oxide-derived nanostructured Ag electrocatalysts. Nanostructured Ag electrocatalysts prepared through an electrochemical reduction of Ag_2O exhibited a high catalytic activity and selectivity for CO_2 reduction to CO, which was shifted towards a lower overpotential compared to untreated Ag. At a moderate overpotential of 0.49 V, the oxide-derived nanostructured Ag electrocatalysts were capable of electrochemically reducing CO_2 to CO with ~80% catalytic selectivity, which is much higher in comparison with that (4%) of untreated Ag catalysts under identical conditions. Electrokinetic studies for CO_2 reduction were performed on both nanostructured and untreated Ag electrocatalysts, revealing an enhanced stabilization for the $COOH^{\bullet}$ intermediate (CO_2 activation) on the oxide-derived nanostructured Ag. In addition, a high local pH created within the porous-like nanostructured Ag may also play a role in the improved catalytic activity of CO_2 reduction with suppressed H_2 evolution.

Chapter 4 reports the electrocatalytic reduction of CO_2 on Au-Pt bimetallic films with tunable compositions, providing a platform for investigating the relationship between the binary composition and the catalytic activity. The Au-Pt alloy films with controllable compositions were prepared by a magnetron sputtering co-deposition technique, exhibiting an improved catalytic activity for the reduction of CO_2 to CO with increasing the Au content. This tunable selectivity is due to the fact that the adjustable binding strength of the $COOH^{\bullet}$ and $CO^{\bullet}$ intermediates caused by the variation of surface electronic properties (d-band center energy) that is related to the surface binary composition. More importantly, surface valence band XPS spectra reveals a gradual shift of the d-band center away from the Fermi level with increasing the Au content. This change correspondingly lowers the binding strength for $COOH^{\bullet}$ and CO intermediates, resulting in the variation of catalytic activity in the reduction of CO_2 on the compositionally variant Au-Pt bimetallic films. Moreover, we demonstrate a scaling correlation between the binding strength of the intermediates and the binary composition.

Chapter 5 finally draws the conclusions and outlook based on the above CO_2 reduction work in chapter 2, chapter 3 and chapter 4.

References

[1]   S. J. Davis, K. Caldeira, H. D. Matthews, *Science* **2010**, *329*, 1330–1333.

[2]   O. Hoegh-Guldberg, P. J. Mumby, A J. Hooten, R. S. Steneck, P. Greenfield, E. Gomez, C. D. Harvell, P. F. Sale, A. J. Edwards, K. Caldeira, et al., *Science* **2007**, *318*, 1737–42.

[3]   J. C. Orr, V. J. Fabry, O. Aumont, L. Bopp, S. C. Doney, R. a Feely, A. Gnanadesikan, N. Gruber, A. Ishida, F. Joos, et al., *Nature* **2005**, *437*, 681–6.

[4]   J. M. Hall-Spencer, R. Rodolfo-Metalpa, S. Martin, E. Ransome, M. Fine, S. M. Turner, S. J. Rowley, D. Tedesco, M.-C. Buia, *Nature* **2008**, *454*, 96–99.

[5]   Q. Lu, J. Rosen, Y. Zhou, G. S. Hutchings, Y. C. Kimmel, J. G. Chen, F. Jiao, *Nat. Commun.* **2014**, *5*, 3242.

[6]   D. T. Whipple, P. J. a. Kenis, *J. Phys. Chem. Lett.* **2010**, *1*, 3451–3458.

[7]   J. L. DiMeglio, J. Rosenthal, *J. Am. Chem. Soc.* **2013**, *135*, 8798–801.

[8]   Y. Hori, in *Electrochem. CO2 Reduct. Met. Electrodes* (Ed.: E. Vayenas, C. G., White, R. E., Gamboa-Aldeco, M. E.), Springer New York, **2008**, p. Vol. 42, p 89.

[9]   K. P. Kuhl, E. R. Cave, D. N. Abram, T. F. Jaramillo, *Energy Environ. Sci.* **2012**, *5*, 7050–7059.

[10]   J. Qiao, Y. Liu, F. Hong, J. Zhang, *Chem. Soc. Rev.* **2014**, *43*, 631–675.

[11]   M. Gattrell, N. Gupta, A. Co, *J. Electroanal. Chem.* **2006**, *594*, 1–19.

[12]   Y. Chen, M. W. Kanan, *J. Am. Chem. Soc.* **2012**, *134*, 1986–1989.

[13]   Y. Chen, C. W. Li, M. W. Kanan, *J. Am. Chem. Soc.* **2012**, *134*, 19969–19972.

[14]   C. W. Li, M. W. Kanan, *J. Am. Chem. Soc.* **2012**, *134*, 7231–7234.

[15]   Y. Hori, K. Kikuchi, S. Suzuki, *Chem. Lett.* **1985**, 1695–1698.

[16]   Y. Hori, H. Wakebe, T. Tsukamoto, O. Koga, *Electrochim. Acta* **1994**, *39*, 1833–1839.

[17]   N. Hoshi, M. Kato, Y. Hori, *J. Electroanal. Chem.* **1997**, *440*, 283–286.

[18]   Y. Hori, I. Takahashi, O. Koga, N. Hoshi, *J. Phys. Chem. B* **2002**, *106*, 15–17.

[19]   J. Xiao, A. Kuc, T. Frauenheim, T. Heine, *J. Mater. Chem. A* **2014**, *2*, 4885.

[20]   T. Hatsukade, K. P. Kuhl, E. R. Cave, D. N. Abram, T. F. Jaramillo, *Phys. Chem. Chem. Phys.* **2014**, *16*, 13814–13819.

[21]   Q. Lu, J. Rosen, F. Jiao, *ChemCatChem* **2015**, *7*, 38–47.

[22]   R. Reske, H. Mistry, F. Behafarid, B. Roldan Cuenya, P. Strasser, *J. Am. Chem. Soc.* **2014**, *136*, 6978–6986.

[23]   R. Kas, R. Kortlever, A. Milbrat, M. T. M. Koper, G. Mul, J. Baltrusaitis, *Phys. Chem. Chem. Phys.* **2014**, *16*, 12194.

[24]   S. Sen, D. Liu, G. T. R. Palmore, *ACS Catal.* **2014**, *4*, 3091–3095.

[25]   W. Tang, A. a Peterson, A. S. Varela, Z. P. Jovanov, L. Bech, W. J. Durand, S. Dahl, J. K. Nørskov, I. Chorkendorff, *Phys. Chem. Chem. Phys.* **2012**, *14*, 76–81.

[26]   M. Liu, Y. Pang, B. Zhang, P. De Luna, O. Voznyy, J. Xu, X. Zheng, C. T. Dinh, F. Fan, C. Cao, et al., *Nature* **2016**, *537*, 382–386.

[27]   J. Rosen, G. S. Hutchings, Q. Lu, S. Rivera, Y. Zhou, D. G. Vlachos, F. Jiao, *ACS Catal.* **2015**, *5*, 4293–4299.

[28]   M. Ma, B. J. Trześniewski, J. Xie, W. A. Smith, *Angew. Chemie Int. Ed.* **2016**, *55*, 9748–9752.

[29]   Y. Hori, K. Kikuchi, A. Murata, S. Suzuki, *Chem. Lett.* **1986**, 897–898.

[30]   Y. Li, S. H. Chan, Q. Sun, *Nanoscale* **2015**, *7*, 8663–83.

[31]   R. Kortlever, J. Shen, K. J. P. Schouten, F. Calle-Vallejo, M. T. M. Koper, *J. Phys. Chem. Lett.* **2015**, *6*, 4073–4082.

[32]   A. a. Peterson, F. Abild-Pedersen, F. Studt, J. Rossmeisl, J. K. Nørskov, *Energy Environ. Sci.* **2010**, *3*, 1311.

[33]   A. A. Peterson, J. K. Nørskov, *J. Phys. Chem. Lett.* **2012**, *3*, 251–258.

[34]   W. Tang, A. a Peterson, A. S. Varela, Z. P. Jovanov, L. Bech, W. J. Durand, S. Dahl, J.

K. Nørskov, I. Chorkendorff, *Phys. Chem. Chem. Phys.* **2012**, *14*, 76–81.

[35]   H. A. Hansen, J. B. Varley, A. A. Peterson, J. K. Nørskov, *J. Phys. Chem. Lett.* **2013**, *4*, 388–392.

[36]   R. M. Mohamed, D. L. McKinney, W. M. Sigmund, *Mater. Sci. Eng. R Reports* **2012**, *73*, 1–13.

[37]   E. B. Nursanto, H. S. Jeon, C. Kim, M. S. Jee, J. H. Koh, Y. J. Hwang, B. K. Min, *Catal. Today* **2016**, *260*, 107–111.

[38]   H.-E. Lee, K. D. Yang, S. M. Yoon, H.-Y. Ahn, Y. Y. Lee, H. Chang, D. H. Jeong, Y.-S. Lee, M. Y. Kim, K. T. Nam, *ACS Nano* **2015**, *9*, 8384–8393.

[39]   D. R. Kauffman, D. Alfonso, C. Matranga, H. Qian, R. Jin, *J. Am. Chem. Soc.* **2012**, *134*, 10237–10243.

[40]   W. Zhu, R. Michalsky, Ö. Metin, H. Lv, S. Guo, C. J. Wright, X. Sun, A. a Peterson, S. Sun, *J. Am. Chem. Soc.* **2013**, *135*, 16833–16836.

[41]   W. Zhu, Y.-J. Zhang, H. Zhang, H. Lv, Q. Li, R. Michalsky, A. a Peterson, S. Sun, *J. Am. Chem. Soc.* **2014**, *136*, 16132–16135.

[42]   K. P. Kuhl, T. Hatsukade, E. R. Cave, D. N. Abram, J. Kibsgaard, T. F. Jaramillo, *J. Am. Chem. Soc.* **2014**, *136*, 14107–14113.

[43]   C. Kim, H. S. Jeon, T. Eom, M. S. Jee, H. Kim, C. M. Friend, B. K. Min, Y. J. Hwang, *J. Am. Chem. Soc.* **2015**, *137*, 13844–13850.

[44]   A. Salehi-Khojin, H. M. Jhong, B. A. Rosen, W. Zhu, S. Ma, P. J. A. Kenis, R. I. Masel, *J. Phys. Chem. C* **2013**, *117*, 1627–1632.

[45]   J. Rosen, G. S. Hutchings, Q. Lu, R. V. Forest, A. Moore, F. Jiao, *ACS Catal.* **2015**, *5*, 4586–4591.

[46]   C. W. Li, J. Ciston, M. W. Kanan, *Nature* **2014**, *508*, 504–507.

[47]   A. Verdaguer-Casadevall, C. W. Li, T. P. Johansson, S. B. Scott, J. T. McKeown, M. Kumar, I. E. L. Stephens, M. W. Kanan, I. Chorkendorff, *J. Am. Chem. Soc.* **2015**, *137*, 9808–9811.

[48] X. Feng, K. Jiang, S. Fan, M. W. Kanan, *J. Am. Chem. Soc.* **2015**, *137*, 4606–4609.

[49] Y. Hori, R. Takahashi, Y. Yoshinami, A. Murata, *J. Phys. Chem. B* **1997**, *101*, 7075–7081.

[50] K. Manthiram, B. J. Beberwyck, A. P. Alivisatos, *J. Am. Chem. Soc.* **2014**, *136*, 13319–13325.

[51] S. Rasul, D. H. Anjum, A. Jedidi, Y. Minenkov, L. Cavallo, K. Takanabe, *Angew. Chemie Int. Ed.* **2015**, *54*, 2146–2150.

[52] D. Kim, J. Resasco, Y. Yu, A. M. Asiri, P. Yang, *Nat. Commun.* **2014**, *5*, 4948.

[53] S. Sarfraz, A. T. Garcia-Esparza, A. Jedidi, L. Cavallo, K. Takanabe, *ACS Catal.* **2016**, *6*, 2842–2851.

[54] Y. Zhao, C. Wang, G. G. Wallace, *J. Mater. Chem. A* **2016**, *4*, 10710–10718.

[55] M. Li, J. Wang, P. Li, K. Chang, C. Li, T. Wang, B. Jiang, H. Zhang, H. Liu, Y. Yamauchi, et al., *J. Mater. Chem. A* **2016**, *4*, 4776–4782.

[56] Z. Yin, D. Gao, S. Yao, B. Zhao, F. Cai, L. Lin, P. Tang, P. Zhai, G. Wang, D. Ma, et al., *Nano Energy* **2016**, *27*, 35–43.

[57] D. A. Torelli, S. A. Francis, J. C. Crompton, A. Javier, J. R. Thompson, B. S. Brunschwig, M. P. Soriaga, N. S. Lewis, *ACS Catal.* **2016**, *6*, 2100–2104.

[58] C. Shi, H. a Hansen, A. C. Lausche, J. K. Nørskov, *Phys. Chem. Chem. Phys.* **2014**, *16*, 4720.

[59] F. Jia, X. Yu, L. Zhang, *J. Power Sources* **2014**, *252*, 85–89.

[60] S. Siahrostami, A. Verdaguer-Casadevall, M. Karamad, D. Deiana, P. Malacrida, B. Wickman, M. Escudero-Escribano, E. a Paoli, R. Frydendal, T. W. Hansen, et al., *Nat. Mater.* **2013**, *12*, 1137–1143.

[61] M. Li, J. Wang, P. Li, K. Chang, C. Li, T. Wang, B. Jiang, H. Zhang, H. Liu, Y. Yamauchi, et al., *J. Mater. Chem. A* **2016**, *4*, 4776–4782.

[62] R. Kortlever, I. Peters, S. Koper, M. T. M. Koper, *ACS Catal.* **2015**, *5*, 3916–3923.

[63] K. J. P. Schouten, E. Pérez Gallent, M. T. M. Koper, *J. Electroanal. Chem.* **2014**, *716*, 53–57.

[64] Y. Hori, A. Murata, R. Takahashi, *J. Chem. Soc. Faraday Trans. 1 Phys. Chem. Condens. Phases* **1989**, *85*, 2309.

2. Electrocatalytic CO_2 Reduction on Cu Nanowire Arrays

This chapter demonstrates a new and simple synthesis method to prepare a Cu nanowire array catalyst for the electrocatalytic reduction of CO_2. This chapter contains two parts, (i) the electrocatalytic reduction of CO_2 on the Cu nanowire (NW) arrays with fixed NW length and density, (ii) Cu NW array electrodes with different length and density were controllably synthesized for the reduction of CO_2.

2.1 Selective Electrochemical Reduction of CO_2 to CO on CuO-derived Cu Nanowires

In this work, we report a new synthesis method to prepare a Cu nanowire electrocatalyst for selective CO_2 reduction at room temperature and atmospheric pressure. Cu nanowire array electrodes were prepared through a two-step synthesis of $Cu(OH)_2$ and CuO nanowire arrays on Cu foil substrates and a subsequent electrochemical reduction of the CuO nanowire arrays. The Cu nanowire arrays are able to electrochemically reduce CO_2 to CO with a faradaic efficiency of ~50% at a moderate overpotential of 490 mV, which is significantly higher than that of polycrystalline Cu foil catalysts at identical conditions. The improved faradaic efficiency for the reduction of CO_2 to CO is ascribed to the enhanced stabilization for the $CO_2^{\bullet-}$ intermediate on the high surface area Cu nanowire arrays.

Graphical Abstract

$$CO_2 + H_2O \longrightarrow CO, HCOOH, H_2$$
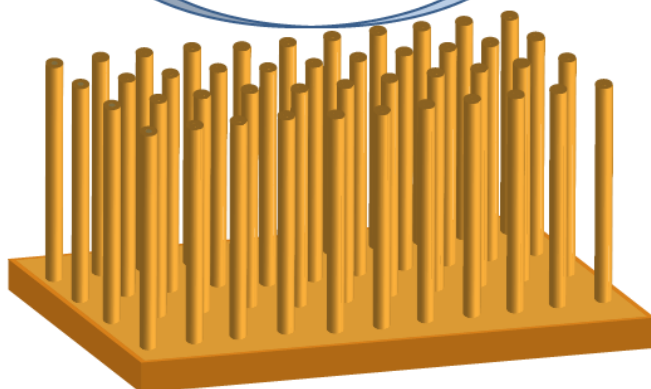
Cu nanowire array electrode

2.1.1 Introduction

The increasing global CO_2 concentration is a serious environmental threat that is responsible for climate change[1] and ocean acidification[2]. To reduce anthropogenic CO_2 emissions into the atmosphere, the capture and sequestration of CO_2 at large emission sources such as industrial power plants has been proposed.[3,4] However, sequestration methods including geological and deep sea storage has some unknown ecological and environmental impacts and risk. For the utilization of the captured CO_2, the electrochemical reduction of CO_2 has attracted considerable attention as an attractive solution.[4–14] In this process, CO_2 could be employed as a chemical feedstock and converted into high energy density fuels such as syngas (CO and H_2) and other hydrocarbons.[7–9] In order to avoid extra CO_2 emission, the process of the electrochemical reduction of CO_2 can be coupled to renewable energy sources such as solar energy, wind energy and hydropower.[4,7]

The selective electrochemical reduction of CO_2 to CO at room temperature is a particularly interesting reaction, which can be a potential key step in the development of a clean and sustainable energy supply. Traditionally, CO is produced at an industrial scale from a wide variety of materials that includes natural gas, residual oil, petroleum coke and coal.[15] CO can be used as chemical feedstock in the Fischer–Tropsch process, a well-developed technology that has been used in industry to generate chemicals (such as methanol) and synthetic fuels (such as diesel fuel) from syngas (CO and H_2) for many decades.[4,5] A key technological challenge for the electroreduction of CO_2 to CO is to develop a suitable catalyst that is capable of achieving a stable and cost-effective process with high efficiency and selectivity at low overpotentials.[5,7,16–18]

Researchers have investigated the electrochemical reduction of CO_2 using various metal electrodes in CO_2-saturated aqueous solutions at ambient temperature.[4–10,16–24] As many as 16 different products have been reported from the electroreduction of CO_2,[7] thus it is necessary to find catalyst materials with a high selectivity towards a desired product formation. It has been demonstrated that polycrystalline Au and Ag are capable of reducing CO_2 to CO with high efficiency in CO_2-saturated aqueous electrolytes.[6,9,19,21] However, Au and Ag are not suitable catalyst materials for large-scale applications due to their high cost and low abundance. Developing cheap and earth-abundant catalysts with a simple and scalable method for fabrication and high selectivity for CO production is essential for achieving large-scale utilization of CO_2 reduction.

The focus of most CO_2 reduction studies has concentrated on Cu electrodes because Cu is capable of reducing CO_2 to CO and hydrocarbons such as CH_4 and C_2H_4, in CO_2 saturated-aqueous electrolytes at ambient pressure and temperature, as first reported by Y. Hori.[25,26] It has been demonstrated that the surface morphology and roughness of copper electrodes have a dramatic influence on the catalytic activity and product selectivity during the electrochemical reduction of CO_2.[10,18,27–29] Tang *et al.* reported that Cu nanoparticle covered electrodes showed better selectivity towards ethylene and CO formation compared with the other two electrodes, an electropolished Cu electrode and an argon gas sputtered Cu electrode.[29] In that study, the improvement in CO_2 reduction performance was explained by the high surface area which was able to provide a greater abundance of undercoordinated sites on the roughened Cu surface.[29] Kanan et al. have shown that a modified Cu electrode (thick Cu_2O film-derived Cu) prepared by annealing Cu foil in air at 500 °C for 12 h has a large roughness factor, resulting in a very high selectivity for CO formation at low potentials, though the exact mechanism for the improved selectivity was not well established.[18] In addition, it was reported that Cu nanofoams exhibited a better selectivity to HCOOH production compared to polycrystalline Cu during electrochemical CO_2 reduction.[10] Recently, the effect of the size of Cu nanoparticles on CO_2 electroreduction has been demonstrated, showing an increase in the catalytic activity and selectivity for CO and H_2 with decreasing Cu particle size.[27] All the above studies indicate that a nanostructured surface morphology has a significant effect on the catalytic activity and selectivity for the electrochemical reduction of CO_2. However, there is little reported research on high surface area Cu nanowires for electrochemical reduction of CO_2.[18,30]

Here, we show the first example of the electrochemical reduction of CO_2 on Cu nanowires reduced from CuO with a simple fabrication method. The Cu nanowire arrays are able to electrochemically reduce CO_2 to different products, with a predominant formation of CO with a significantly higher faradaic efficiency (FE) than polycrystalline Cu at moderate overpotentials ($\eta < 500$ mV). Compared to the Cu electrode prepared by annealing Cu foil in air at 500 °C for 12 h (FE for CO is ~45% at $\eta < 390$ mV)[18], the Cu nanowire arrays prepared at 150 °C for 2 h has a comparable FE of ~50% for CO production at a moderate overpotential ($\eta = 490$ mV). Furthermore, a Tafel plot for the Cu nanowires prepared by a simple synthesis method was found to have a slope of ~110 mV/dec at low overpotential ($\eta < 0.3$ V), which is consistent with that (116 mV/dec) of Cu electrodes prepared at 500 °C for 12 h,[18] implying a favorable formation of the $CO_2^{\bullet-}$ intermediate while suppressing

hydrogen evolution. Therefore, this study shows that an easily fabricated CuO-derived Cu nanowire array offers a highly selective platform for the electrochemical reduction of CO_2 to CO.

2.1.2 Experimental section

Fabrication of CuO Nanowires

$Cu(OH)_2$ nanowires were first synthesized on Cu foils using a simple wet chemical method.[31,32] The Cu foils were ultrasonically cleaned in acetone and ethanol and then rinsed with de-ionized water. The cleaned Cu foils were dried with nitrogen and then immersed into a solution mixture containing 0.133 M $(NH_4)_2S_2O_8$ and 2.667 M NaOH for 15 min. After this time the Cu foils turned a deep blue color (the blue color is indicative of the formation of $Cu(OH)_2$ nanowires.[31]) and were taken out from the solution, rinsed with de-ionized water and absolute ethanol, and dried with nitrogen. After that, CuO nanowires were fabricated by annealing the $Cu(OH)_2$ nanowire arrays at 150 °C for 2 hours under an air atmosphere.

Physical Characterization

The morphology and nanostructure of the samples before and after electrochemical reduction of CO_2 were characterized by using scanning electron microscope (SEM, JEOL JSM-6010LA). The crystal structure of the samples was measured by X-ray diffraction (XRD) using a diffractometer (Bruker AXS GmbH-D8 Discover) with Co-Kα radiation (λ = 1.7903 Å). X-ray photoelectron spectroscopy (XPS, Thermo Scientific™ K-Alpha™) was used to confirm the oxidation states of Cu in the samples before and after the electrolysis.

Surface Area Measurements

Surface roughness factors of the Cu nanowires and polycrystalline Cu foils were determined by measuring electrochemical double-layer capacitance.[28,33,34] The cyclic voltammograms (CVs) were measured in N_2 bubbled 0.1 M phosphate buffer for a potential range in which no faradaic processes were occurring (Figure S2.1.6 and Figure S2.1.7). The geometric current density (j_{tot}) was plotted against the scan rate of the CV and the slope of the linear regression was used to determine the capacitance (C). The surface roughness factor can

be obtained by normalizing the capacitance value to that of polycrystalline Cu foil (the surface roughness factor of polycrystalline Cu is used as the standard reference)
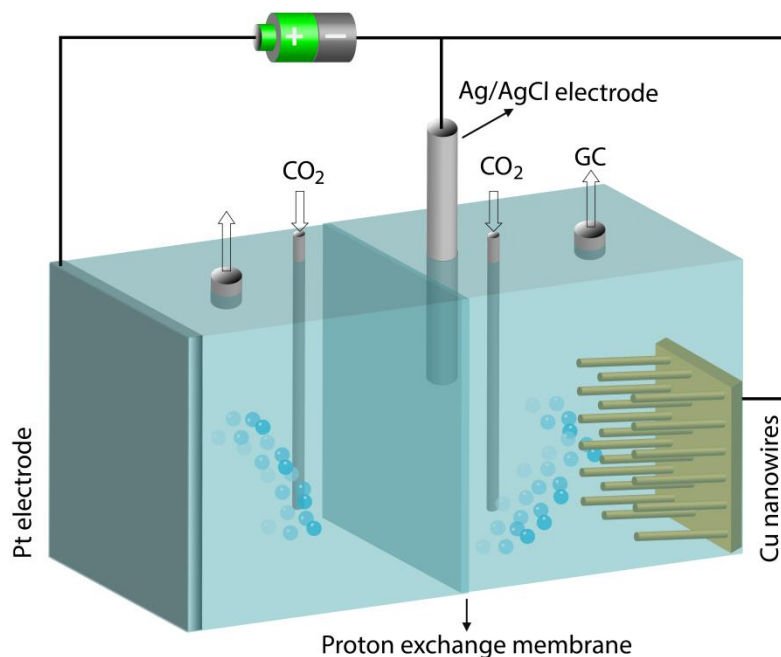
Electrochemical CO$_2$ Reduction

CO$_2$ electrolysis experiments were performed in an electrochemical cell made from Teflon (Figure 2.1) using a three electrode configuration at ambient temperature and pressure. The cell consists of two compartments (working and counter electrode compartments), which is separated by a Nafion-115 proton exchange membrane to prevent the oxidation of CO$_2$ reduction products. In the three-electrode configuration measurement, the counter electrode was a Pt film (~160 nm) deposited on Ti foil by using direct current magnetron sputtering (XRD pattern of the Pt film sputtered on Ti foil is shown in Figure S2.1.1) and an Ag/AgCl electrode (XR300, saturated KCl + AgCl solution (KS120), Radiometer Analytical) was used as the reference electrode (RE). The applied potentials vs. Ag/AgCl were converted to the reversible hydrogen electrode (RHE) using the equation:

$$V_{RHE} = V_{Ag/AgCl} + V^0_{Ag/AgClvs.NHE} + 0.059 pH \tag{2.1}$$

where $V^0_{Ag/AgClvs.NHE}$ is 0.199 V at 25 °C. The electrochemical reduction of CO$_2$ was performed in a 0.1 M KHCO$_3$ (Sigma Aldrich, 99.95%) electrolyte saturated with CO$_2$ (pH = 6.83) at ambient temperature and pressure.

The cathodic compartment was continuously purged with a constant CO$_2$ flow rate and vented directly into the gas-sampling loop of a gas chromatograph (GC, Interscience) in order to enable periodic quantification of the gas-phase products. Liquid products formed during the CO$_2$ reduction were identified and quantified by nuclear magnetic resonance (NMR) after completion of the electrolysis.

Figure 2.1 The schematic illustration of the electrochemical cell used for reduction of CO_2.

NMR Data Analysis

NMR measurements were performed by an Agilent MR400DD2 NMR spectrometer operating at 400 MHz. Samples were prepared by mixing 450 μL of the electrolyte solutions with 50 μL of D2O containing internal reference t-BuOH with a known concentration. 1H NMR spectra were acquired by applying a hard pulse solvent pre-saturation pulse sequence with 2 s saturation delay, 2 s relaxation delay, 2.5 s acquisition time, and spectral window of 6400 Hz. Typically, 8 scans were collected and the peak areas were integrated in order to calculate the concentration of the solutes by taking into account the difference in the number of protons in the reference compound with respect to the product.

2.1.3 Results and discussion

Synthesis of CuO Nanowires

A typical SEM image of the prepared $Cu(OH)_2$ nanowires is shown in Figure 2.2a. The Cu substrate was uniformly covered with $Cu(OH)_2$ nanowires, which were observed to have an average diameter of around 100-250 nm and length of approximately 5-10 μm. The XRD pattern shown in Figure 2.2c confirms the presence of $Cu(OH)_2$ in this sample, in addition to the presence of the Cu foil substrate. After this initial characterization, the $Cu(OH)_2$ nanowires were annealed to form CuO. The annealing temperature and time were adjusted to dehydrate the $Cu(OH)_2$ nanowires in air and argon, respectively (shown in Figure S2.1.3), and the optimal conditions were found to be 150 ℃ for 2 hours in an air atmosphere. While the copper oxide nanowires retained their nanostructured morphology after annealing, a slight bundling of the nanowires was observed, as shown in Figure 2.2b. The XRD pattern in Figure 2.2d reveals the $Cu(OH)_2$ nanowires were dehydrated to form CuO after annealing in air at 150 ℃ for 2 hours, with no more indication of any remaining $Cu(OH)_2$.
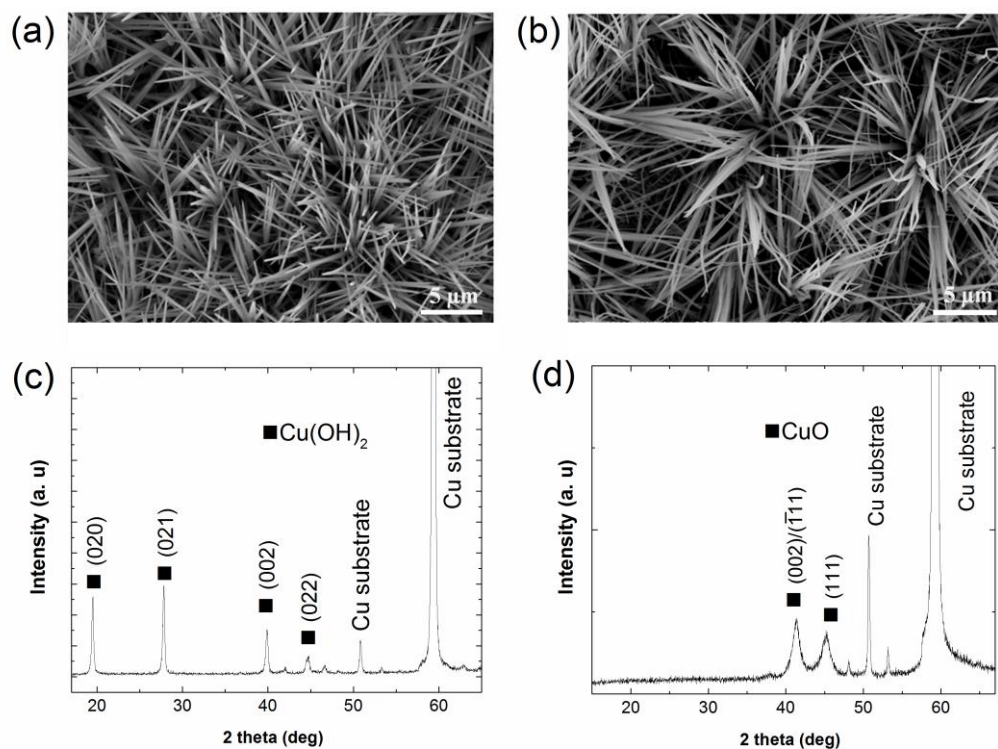
Figure 2.2 SEM images and XRD patterns of $Cu(OH)_2$ nanowires before (a) (c) and after (b) (d) annealing in air at 150 ℃ for 2 h, respectively.

CuO-derived Cu Nanowires

The resulting CuO nanowire arrays were directly utilized in electrochemical reduction of CO_2 in CO_2-saturated 0.1 M $KHCO_3$ electrolytes, and were reduced to Cu nanowires during electrolysis. In order to confirm the formation of the Cu nanowires, further characterization of the samples was performed. The SEM images of CuO nanowires after CO_2 reduction electrolysis at -0.6 V vs. RHE reveals the nanowires structure, as shown in Figure S2.1.4, therefore we conclude that all CO_2 electrochemical reduction experiments occurred on nanowire structured substrates.
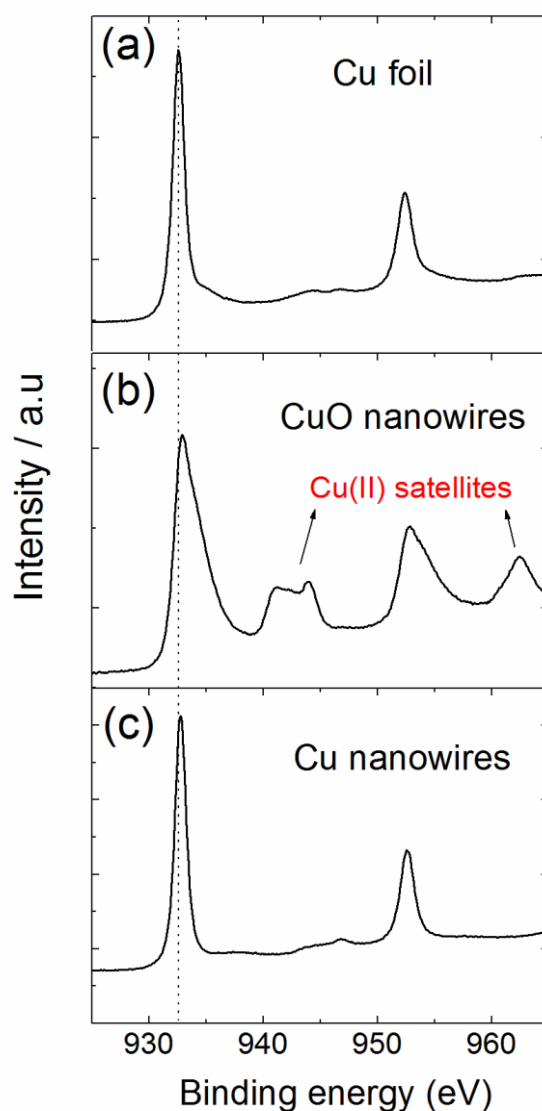
Figure 2.3 XPS spectrum of the polycrystalline Cu foil (a) and CuO nanowires on Cu foil before (b) and after (c) CO_2 reduction electrolysis at -0.6 V vs. RHE.

To confirm the oxidation states of the samples before and after CO_2 reduction, XPS measurements were performed. The Cu 2p XPS spectrum of the polycrystalline Cu foil (before CO_2 reduction electrolysis) and the CuO nanowires on the Cu foil substrate before and after CO_2 reduction electrolysis are shown in Figure 2.3. The Cu $2p_{3/2}$ peak at 932.58 eV was observed for the polycrystalline Cu foil, shown in Figure 2.3a. For the CuO nanowire sample, the Cu $2p_{3/2}$ peak shifted to a higher binding energy (932.98 eV) and was much broader compared to that of Cu foil, which is consistent with the Cu $2p_{3/2}$ peak analysis of CuO and Cu in previous reports.[35] In addition to the shift of the Cu $2p_{3/2}$ peak between CuO and Cu, the Cu oxidation states can be further distinguished by observing satellite features in the Cu2p XPS spectrum.[35] Cu^{2+} satellite peaks at 941.3, 943.9 and 962.5 eV in Figure 2.3b indicate the presence of CuO, which is consistent with the observation from the XRD pattern shown in Figure 2.2d. After CO_2 reduction electrolysis, the Cu $2p_{3/2}$ peak shifted back to a lower binding energy of 932.78 eV, and the Cu^{2+} satellite peaks were no longer observed, as shown in Figure 2.3c, indicating the presence of Cu^0 or Cu^{1+} after CO_2 reduction. The Cu 2p XPS spectrum of the nanowires after CO_2 reduction is almost identical to that of the polycrystalline Cu foil. In addition, we only observed Cu^0 peaks in the XRD pattern of the nanowires after CO_2 reduction electrolysis (Figure S2.1.5). These data indicate that the CuO nanowires in this study were reduced to Cu during the electrochemical reduction of CO_2. Thus, we can confirm that the electrochemical reduction of CO_2 in our study occurred on Cu nanowire arrays.

CO_2 Reduction Performance on CuO-derived Cu Nanowires

The electrocatalytic CO_2 reduction results on Cu nanowires and Cu foils are presented in Figure 2.4. It was found that the Cu nanowire array electrodes exhibited an initial high geometric current density (for instance, Figure S2.1.8 shows $j_{tot} > 1$ mA/cm^2 for 390 seconds at -0.6 V vs. RHE) as the CuO nanowires were reduced to Cu nanowires, and subsequently a stable current density was observed during electrolysis. At a negative potential of -0.35 V vs. RHE, the Cu nanowire arrays revealed a stable j_{tot} with a FE of ~ 18% for CO production. At a more negative potential of -0.5 V vs. RHE, Cu nanowire arrays exhibited an increased j_{tot} in Figure 2.4b, and a FE of ~ 30% for CO and a FE of ~ 7.5% for HCOOH (Figure 2.5) were observed. Notably, a peak FE of ~ 50% for CO production (the FE for HCOOH was ~ 30% in Figure 2.5) on Cu nanowires was reached at -0.6 V vs. RHE shown in Figure 2.4a, corresponding to an overpotential of 490 mV relative to the CO_2/CO equilibrium potential

(-0.11 V vs. RHE). Furthermore, a relatively stable FE for CO production on Cu nanowire arrays was observed in Figure 2.4, indicating the catalytic activity for CO_2 reduction on Cu nanowire arrays was relatively stable during that time.
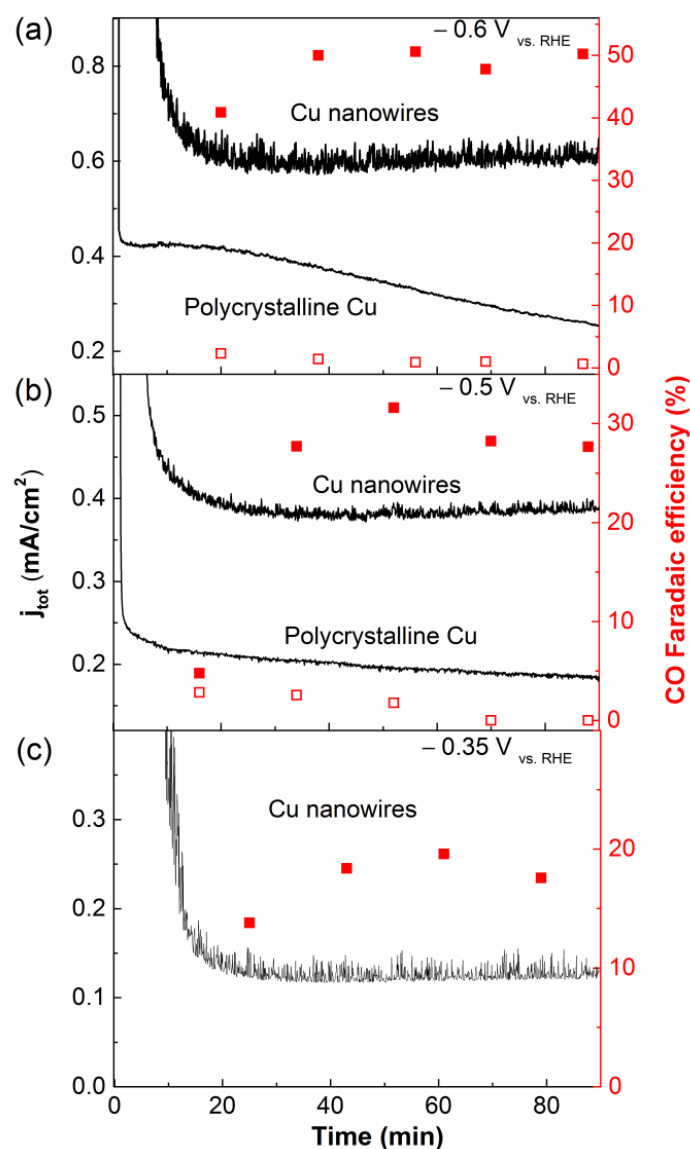
Figure 2.4 CO_2 reduction performance of CuO-derived Cu nanowires. CO_2 reduction activity of CuO-derived Cu nanowires and polycrystalline Cu foil at (a) -0.6 V and (b) -0.5 V, and CuO-derived Cu nanowires at (c) -0.35 V vs. RHE in CO_2-saturated 0.1 M $KHCO_3$ electrolytes (no CO production was observed for polycrystalline Cu at -0.35 V vs. RHE). The geometric current density is shown on the left axis and the faradaic efficiency for CO is shown on the right axis (■ and □ represent CO faradaic efficiency on Cu nanowires and Cu foil respectively).

In contrast, the polycrystalline Cu electrodes experienced a decrease in current density over time under identical conditions, as shown in Figure 2.4a and b. In addition, the polycrystalline Cu substrates showed a low faradaic efficiency for CO (FE < 3% at -0.5 V and -0.6 V vs. RHE), and the FE for CO decreased over time shown in Figure 2.4a and b, which indicates a fast decrease in catalytic activity for CO_2 reduction. It was found that the FE for HCOOH on the polycrystalline Cu foils was only ~11.6% at -0.6 V vs. RHE (Figure 2.5). It was reported that the performance of CO_2 reduction on polycrystalline Cu foil in electrolytes without stringent purification could not be observed due to rapidly complete deactivation of catalytic activity.[18,28] Indeed, in our study, at less negative potentials than -0.5 V vs. RHE, the CO production on polycrystalline Cu did not reach the detection limit of our GC.
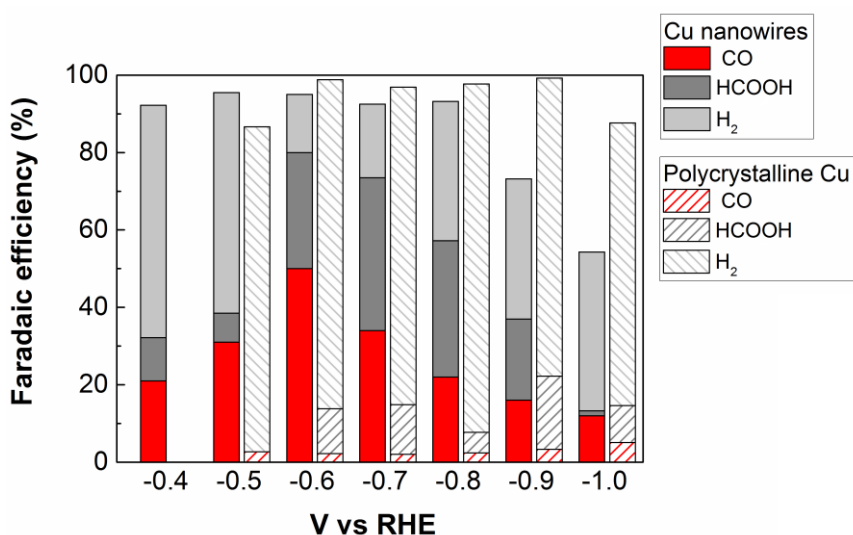
Figure 2.5 Faradaic efficiency for CO, HCOOH and H_2 at various potentials in CO_2-saturated 0.1 M $KHCO_3$ electrolytes at ambient temperature and pressure.

CO_2 reduction on Cu nanowire arrays and Cu foils was also performed at more negative potentials in order to investigate the FE for products (HCOOH, CO and H_2) as a function of potentials, as shown in Figure 2.5. The FE for CO on Cu nanowire arrays obviously increased with increasing overpotentials at potentials of ≥ -0.6 V vs. RHE and then evidently declined with further increasing overpotentials at potentials of ≤ -0.6 V vs. RHE. Similarly, the FE for formic acid on Cu nanowire arrays also experienced an increase at potentials of ≥ -0.7 V vs. RHE and a decrease at potentials of ≤ -0.7 V vs. RHE. It can be readily found that highest FE of ~ 50% for CO production on Cu nanowire arrays was obtained at -0.6 V vs. RHE, while the

peak FE of ~ 40% for HCOOH on Cu nanowire arrays was reached at a more negative potential (-0.7 V vs. RHE).

Because H_2 evolution is always a competing reaction with CO_2 reduction in CO_2-saturated electrolytes, H_2 was also identified and quantified as a function of potentials during CO_2 reduction electrolysis shown in Figure 2.5. As we note in Figure 2.5, the total faradaic efficiencies for all the reduction products of CO_2 (the FE for CO is ~ 50% and the FE for HCOOH is ~ 30%) on Cu nanowire arrays add up to ~ 80% at -0.6 V vs. RHE. Only 15% FE for H_2 is produced on Cu nanowire arrays at this potential. As a comparison, the majority of the current on the polycrystalline Cu foils is used for H_2 evolution at various potentials (Figure 2.5), which is consistent with previous studies for Cu foil in CO_2-saturated electrolytes.[6,18]

At less negative potentials (-0.4 V and -0.5 V vs. RHE), the decrease in total faradaic efficiencies for CO and HCOOH on Cu nanowire arrays corresponds to an increase of faradaic efficiency for H_2 evolution with lower overpotentials, as shown in Figure 2.5, which is attributed to the fact that the overpotential is not high enough to drive CO_2 reduction efficiently which is directly competing with H_2 evolution that requires a relatively small overpotential to occur.[5] At more negative potentials than -0.6 V vs. RHE, the total faradaic efficiencies for CO and HCOOH decreases with increasing overpotentials and the corresponding faradaic efficiency for H_2 evolution increases. Furthermore, hydrocarbon gas phase products (ethylene and ethane) are observed at more negative potentials (-0.8 V, -0.9 V and -1.0 V vs. RHE) in Figure S2.1.9. At more negative potentials, the rate of CO2 reduction ($\mu mol/s/cm^2$) shows a dramatic increase up to ~ -0.7 V vs. RHE, and then increases much slower with increasing potentials (shown in Figure S2.1.10), which indicates mass transfer limitations at higher overpotentials.[18] Thus, with more negative potentials (< -0.6 V vs. RHE), the observed decrease in the total faradaic efficiencies for CO_2 reduction and the increase in faradaic efficiency for H_2 evolution reflect the mass transport limitations at relatively high current densities.[18]

Enhanced Performance Mechanism

The surface roughness factor for the Cu nanowires arrays relative to polycrystalline Cu foils were determined by measuring the electrochemical double-layer capacitance.[28,33,34] In Figure S2.1.6, Cu nanowire arrays show a capacitance of 3.5 mF, which means that the surface roughness factor is ~ 80 times larger than that of the smooth polycrystalline Cu foil (the capacitance of 0.043 mF in Figure S2.1.7). Thus, the increase of the geometric current density (Figure 2.4) for Cu nanowire arrays during the electrochemical reduction of CO_2 can be explained taking into account the higher surface area of the Cu nanowire arrays. Furthermore, the high catalytic selectivity (high FE for CO and HCOOH) for CO_2 reduction on Cu nanowire arrays may be attributed to the high surface area of Cu nanowire arrays that may provide more active sites for CO_2 reduction electrolysis. It is interesting to note, however, the roughness factor difference (~ 80×) is considerably larger than the difference in j_{tot} between the two electrodes (~ 2×). The discrepancy between the increased surface area and increased j_{tot} seems to show that all of the increased surface area is not active for CO_2 reduction. One possible mechanism is the coverage of active CO_2 reduction sites caused by product formation, where the reaction products block active sites. This coverage of active sites is most likely to reduce the overall efficiency, because the long length of the nanowires may make product diffusion very difficult.

In order to compare the catalytic activity, cyclic voltammetry of Cu nanowires and smooth Cu in CO_2-saturated 0.1 M $KHCO_3$ electrolytes were shown in Figure S2.1.11. The corresponding potentials at the electroreduction current density of 0.5 mA/cm^2 for smooth Cu and Cu nanowires are observed at -0.69 V and -0.51 V vs. RHE, respectively. This positive shift from -0.69 V to -0.51V may indicate the improved catalytic activity for CO_2 reduction on Cu nanowire arrays.

Further insight into the kinetics of CO_2 reduction on catalysts can be examined by a Tafel plot analysis.[5,9,17,18] Here, a Tafel plot of Cu nanowire arrays (overpotential versus log of the partial current density for CO production) is shown in Figure 2.6. Y. Hori has proposed that a two-electron transfer is involved in the electrochemical reduction of CO_2 to CO, as shown in Scheme 2.1.[6,21] In the initial step, a $CO_2^{\bullet-}$ intermediate adsorbed on metal surface is formed by a one-electron transfer to a CO_2 molecule.[6,9,21] Subsequently, the $CO_2^{\bullet-}$ on the surfaces takes two protons and one electron to form a CO and a H_2O molecule.[5,6,21] It is generally accepted that the first electron transfer for the formation of the $CO_2^{\bullet-}$ is the rate determining

step for the whole process because the first electron transfer requires a much more negative potential compared to the following steps.[5]

Figure 2.6 Tafel plots of the CO partial current density for polycrystalline Cu and Cu nanowires.

Scheme 2.1 Proposed mechanism for reduction of CO_2 to CO on metals.[6,21]

A Tafel relationship between CO current i_{co} and overpotential η can be written as follows:[36]

$$i_{co} \propto P_{CO_2} \exp\left(\alpha \frac{F\eta}{RT}\right) \tag{2.2}$$

where F is Faraday constant, R is the gas constant, T is the absolute temperature, P_{CO_2} is the partial pressure of CO_2, and α is the transfer coefficient.

From Henry's law, the concentration of the dissolved CO_2 in electrolytes can be expressed as:

$$C_{CO_2} = KP_{CO_2} \tag{2.3}$$

where K is constant. Then, equation (2.2) can be written as:[36]

$$i_{co} = nFkC_{CO_2} \exp\left(\alpha \frac{F\eta}{RT}\right) \tag{2.4}$$

where n is the total number of electron transfer needed to convert CO_2 to CO, and k is the rate constant for converting CO_2 to CO (incorporating K).[36] The Tafel slope is given by the partial derivative of the overpotential with respect to the log of the current. Thus, equation (2.4) can be rewritten as:

$$1 = \frac{\alpha F}{2.3RT}\left(\frac{\partial \eta}{\partial \log i_{co}}\right) \tag{2.5}$$

According to the equation (2.5), the Tafel slope $\left(\frac{\partial \eta}{\partial \log i_{co}}\right)$ of ~110 mV/dec for Cu nanowire arrays (η < 0.3 V) shown in Figure 2.6 corresponds to the transfer coefficient of 0.54, which is consistent with the concept that the rate determining step of the reaction is the initial electron transfer to CO_2 on metal electrodes.[6] According to previous studies[5,9,17,18], the low Tafel slope indicates a fast initial electron transfer to a CO_2 molecule (the rate determining step), which implies that the formation of the adsorbed $CO_2^{\bullet-}$ intermediate may be favored on Cu nanowire arrays. Therefore, according to these results, it appears that CuO-derived Cu nanowires are able to provide the enhanced stabilization for the $CO_2^{\bullet-}$ intermediate.

2.1.4 Conclusions

In summary, CuO-derived Cu nanowire array electrodes prepared by a simple method were capable of reducing CO_2 selectively to CO and HCOOH with high faradaic efficiencies (~ 50% and ~30%, respectively) at a moderate potential of -0.6 V vs. RHE. This high faradaic efficiency for CO_2 reduction may be due to the more active sites on the high surface area of Cu nanowires, and the high catalytic selectivity for the reduction of CO_2 to CO is attributed to the dramatically enhanced stabilization for the $CO_2^{\bullet-}$ intermediate. This study shows the surface morphology of Cu electrocatalysts could dramatically influence the catalytic selectivity for CO_2 reduction, making them an excellent platform for future studies of electrochemical reduction of CO_2.

References

[1]   S. J. Davis, K. Caldeira, H. D. Matthews, *Science* **2010**, *329*, 1330–1333.

[2]   J. M. Hall-Spencer, R. Rodolfo-Metalpa, S. Martin, E. Ransome, M. Fine, S. M. Turner, S. J. Rowley, D. Tedesco, M.-C. Buia, *Nature* **2008**, *454*, 96–99.

[3]   R. S. Haszeldine, *Science* **2009**, *325*, 1647–1652.

[4]   D. T. Whipple, P. J. a. Kenis, *J. Phys. Chem. Lett.* **2010**, *1*, 3451–3458.

[5]   Q. Lu, J. Rosen, Y. Zhou, G. S. Hutchings, Y. C. Kimmel, J. G. Chen, F. Jiao, *Nat. Commun.* **2014**, *5*, 3242.

[6]   Y. Hori, in *Electrochem. CO2 Reduct. Met. Electrodes* (Ed.: E. Vayenas, C. G., White, R. E., Gamboa-Aldeco, M. E.), Springer New York, **2008**, p. Vol. 42, p 89.

[7]   K. P. Kuhl, E. R. Cave, D. N. Abram, T. F. Jaramillo, *Energy Environ. Sci.* **2012**, *5*, 7050–7059.

[8]   J. Qiao, Y. Liu, F. Hong, J. Zhang, *Chem. Soc. Rev.* **2014**, *43*, 631–675.

[9]   M. Gattrell, N. Gupta, A. Co, *J. Electroanal. Chem.* **2006**, *594*, 1–19.

[10]   S. Sen, D. Liu, G. T. R. Palmore, *ACS Catal.* **2014**, *4*, 3091–3095.

[11]   O. A. Baturina, Q. Lu, M. A. Padilla, L. Xin, W. Li, A. Serov, K. Artyushkova, P. Atanassov, F. Xu, A. Epshteyn, et al., *ACS Catal.* **2014**, *4*, 3682–3695.

[12]   C. H. Lee, M. W. Kanan, *ACS Catal.* **2015**, *5*, 465–469.

[13]   Y. Zhang, V. Sethuraman, R. Michalsky, A. A. Peterson, *ACS Catal.* **2014**, *4*, 3742–3748.

[14]   K. J. P. Schouten, E. Pérez Gallent, M. T. M. Koper, *ACS Catal.* **2013**, *3*, 1292–1295.

[15]   D. J. Wilhelm, D. R. Simbeck, A. D. Karp, R. L. Dickenson, *Fuel Process. Technol.* **2001**, *71*, 139–148.

[16]   Y. Chen, M. W. Kanan, *J. Am. Chem. Soc.* **2012**, *134*, 1986–1989.

[17]   Y. Chen, C. W. Li, M. W. Kanan, *J. Am. Chem. Soc.* **2012**, *134*, 19969–19972.

[18]   C. W. Li, M. W. Kanan, *J. Am. Chem. Soc.* **2012**, *134*, 7231–7234.

[19]   T. Hatsukade, K. P. Kuhl, E. R. Cave, D. N. Abram, T. F. Jaramillo, *Phys. Chem. Chem. Phys.* **2014**, *16*, 13814–13819.

[20]   D. Plana, J. Flórez-Montaño, V. Celorrio, E. Pastor, D. J. Fermín, *Chem. Commun. (Camb).* **2013**, *49*, 10962–10964.

[21]   Y. Hori, H. Wakebe, T. Tsukamoto, O. Koga, *Electrochim. Acta* **1994**, *39*, 1833–1839.

[22]   Y. Hori, H. Wakebe, T. Tsukamoto, O. Koga, *Surf. Sci.* **1995**, *335*, 258–263.

[23]   K. J. P. Schouten, Z. Qin, E. Pérez Gallent, M. T. M. Koper, *J. Am. Chem. Soc.* **2012**, *134*, 9864–9867.

[24]   F. Calle-Vallejo, M. T. M. Koper, *Angew. Chemie* **2013**, *125*, 7423–7426.

[25]   Y. Hori, K. Kikuchi, S. Suzuki, *Chem. Lett.* **1985**, 1695–1698.

[26]   Y. Hori, K. Kikuchi, A. Murata, S. Suzuki, *Chem. Lett.* **1986**, 897–898.

[27]   R. Reske, H. Mistry, F. Behafarid, B. Roldan Cuenya, P. Strasser, *J. Am. Chem. Soc.* **2014**, *136*, 6978–6986.

[28]   R. Kas, R. Kortlever, A. Milbrat, M. T. M. Koper, G. Mul, J. Baltrusaitis, *Phys. Chem. Chem. Phys.* **2014**, *16*, 12194.

[29]   W. Tang, A. a Peterson, A. S. Varela, Z. P. Jovanov, L. Bech, W. J. Durand, S. Dahl, J. K. Nørskov, I. Chorkendorff, *Phys. Chem. Chem. Phys.* **2012**, *14*, 76–81.

[30]   J. Xie, Y. Huang, H. Yu, *Front. Environ. Sci. Eng.* **2014**, 1–6.

[31]   W. Zhang, X. Wen, S. Yang, Y. Berta, Z. L. Wang, *Adv. Mater.* **2003**, *15*, 822–825.

[32]   C. Lin, Y. Lai, D. Mersch, E. Reisner, *Chem. Sci.* **2012**, *3*, 3482–3487.

[33]   C. C. L. McCrory, S. Jung, J. C. Peters, T. F. Jaramillo, *J. Am. Chem. Soc.* **2013**, *135*, 16977–16987.

[34]   C. W. Li, J. Ciston, M. W. Kanan, *Nature* **2014**, *508*, 504–507.

[35]   M. C. Biesinger, L. W. M. Lau, A. R. Gerson, R. S. C. Smart, *Appl. Surf. Sci.* **2010**,

257, 887–898.

[36]   Y. Hori, S. Suzuki, *J. Electrochem. Soc.* **1983**, *130*, 2387.

2.2 Controllable Hydrocarbon Formation via Electrochemical Reduction of CO_2 on Cu Nanowire Arrays

In this work, the effect of Cu nanowire morphology on the selective electrocatalytic reduction of CO_2 is presented. Cu nanowire arrays were prepared through a two-step synthesis of $Cu(OH)_2$ and CuO nanowire arrays on Cu foil substrates and a subsequent electrochemical reduction of the CuO nanowire arrays to Cu nanowire arrays. By this simple synthesis method, Cu nanowire array electrodes with different length and density were able to be controllably synthesized. We show that the selectivity for hydrocarbons (ethylene, n-propanol, ethane and ethanol) on Cu nanowire array electrodes at a fixed potential can be tuned by systematically altering the Cu nanowire length and density. The nanowire morphology effect is linked to the increased local pH in the Cu nanowire arrays and a reaction scheme detailing the local pH induced formation of C_2-products is also presented via a preferred CO dimerization pathway.

This part has been published:

Graphical Abstract
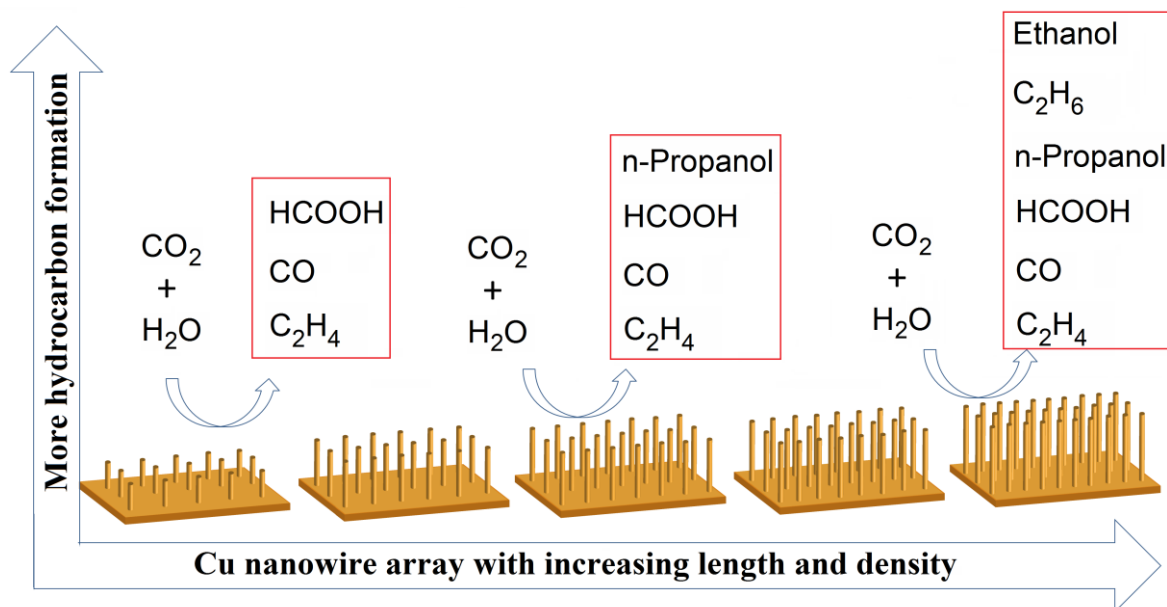
2.2.1 Introduction

The electrochemical reduction of CO_2 to fuel by using renewable energy has attracted considerable attention for closing the anthropogenic carbon cycle.[1–6] From electroreduction of CO_2, the captured CO_2 at the large emission sources could be used as a sustainable feedstock to be electrochemically reduced to high energy density hydrocarbons (such as CH_4 and C_2H_4).[6–9] Hydrocarbon products can be conveniently utilized as fuels within the existing energy infrastructure.[7] For achieving this goal, it is critical to develop a stable and cost-effective catalyst with high selectivity and efficiency. Researchers have identified various electrocatalyst materials that are capable of reducing CO_2 electrochemically in CO_2 saturated-aqueous solutions.[6–14] Among currently identified catalyst materials, Cu is the only known material that is capable of catalyzing the formation of significant amounts of hydrocarbons at high reaction rates in CO_2 saturated-aqueous solutions at ambient temperature and pressure.[8,10] However, controlling the selectivity of the catalytic reduction of CO_2 to a desired hydrocarbon product on a Cu catalyst remains a significant scientific challenge.

The electrochemical reduction of CO_2 to hydrocarbons on Cu catalysts is a complex process with many adsorbed intermediates (such as CO and COH) that could influence the formation of final products.[11,15] One of the important parameters in the electroreduction of CO_2 is the pH that is related to the formation of intermediates in certain reaction pathways, which could have a significant effect on products formation. The effect of local pH at the electrode/electrolyte interface on the selectivity of hydrocarbon products in the electroreduction of CO_2 was proposed by Hori in 1989,[16] showing that a locally high pH formed near Cu electrodes could facilitate the reduction of the intermediate CO to C_2H_4 and alcohols. Recently, Koper *et al.*[17–19] demonstrated that the electrolyte pH could play a key role in the product selectivity towards different hydrocarbons and proposed a CO coupling mechanism, indicating that C_2H_4 could be formed from a CO dimer adsorbed on Cu catalysts. Furthermore, Mul *et al.* reported that the formation of C_2H_4 from a CO coupling mechanism is favorable at a high local pH.[20]

Recently, we showed that CuO-derived Cu nanowire (NW) array electrodes are capable of reducing CO_2 to CO at a moderate overpotentials.[21] At more negative potentials, hydrocarbon gas phase products on Cu NW arrays were observed.[21] In this work, we tailor the selectivity of hydrocarbon products on Cu NW arrays by systematically varying the length and density of the Cu NWs which can offer a high local pH within the NW arrays. In addition,

this study provides further insight into the mechanism of the hydrocarbon formation due to the enhanced CO dimerization afforded by the NW morphology.

2.2.2 Experimental section

Cu(OH)$_2$ NWs were first synthesized on Cu foils by immersing Cu foils into a solution mixture containing 0.133 M (NH$_3$)$_2$S$_2$O$_8$ and 2.667 M NaOH.[22,23] The increased length of Cu(OH)$_2$ NWs was obtained by immersing Cu foils in the solution mixture for longer times. After a discrete synthesis time, the Cu foils were taken out from the solution, rinsed with de-ionized water and absolute ethanol, and dried with nitrogen. CuO NWs were then fabricated by annealing the Cu(OH)$_2$ NW arrays at 150 ℃ for 2 hours in air.[21] The resulting CuO NW arrays were directly used in the electroreduction of CO$_2$, and were electrochemically reduced to Cu NW arrays during electrolysis.[21] Thus, the annealed Cu(OH)$_2$ NWs with gradually increased length and density were electrochemically reduced to Cu NWs with corresponding increased length and density.

2.2.3 Results and discussion

Figure 2.7 shows typical SEM images of Cu(OH)$_2$ NW arrays synthesized under different synthesis time. The corresponding length of Cu(OH)$_2$ NWs prepared at different synthesis time were characterized by SEM (Figure S2.2.3), and the NW length as a function of synthesis time is shown in Table S2.2.1. The increase of NW length follows an enhanced NW density with increasing synthesis time (Figure S2.2.6). For simplification, the change of overall morphology as a function of synthesis time are expressed by using 'nanowire length' in this study.

The electrocatalytic reduction of CO$_2$ on Cu NWs with different lengths were measured at -1.1 V versus the reversible hydrogen electrode (RHE) for 5 h in CO$_2$-saturated 0.1 M KHCO$_3$ (99.95%) electrolytes (pH = 6.83) at ambient temperature and pressure. CO$_2$ electrolysis experiments were performed in an electrochemical cell (Figure 2.1) consisting of working and counter electrode compartments, separated by a Nafion-115 proton exchange membrane to prevent the oxidation of CO$_2$ reduction products. The cathodic compartment was continuously purged with a constant CO$_2$ flow rate and vented directly into the gas-sampling loop of a gas chromatograph (GC) in order to enable periodic quantification of the gas-phase products.

Liquid products formed during the CO_2 reduction were identified and quantified by nuclear magnetic resonance (NMR) after completion of the electrolysis experiments.
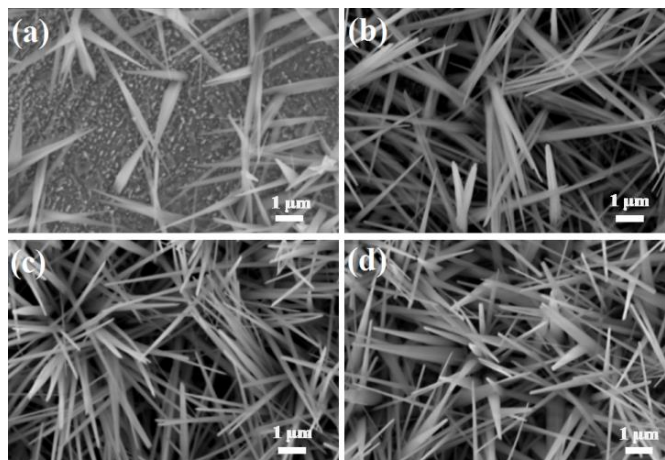

Figure 2.7 SEM images (a-d) of $Cu(OH)_2$ nanowires with synthesis time of 1, 3, 5, 8 min, respectively.

The untreated polycrystalline Cu electrodes (i.e. with no NWs) had an obvious decrease in geometric current density (j_{tot}) with a faradaic efficiency (FE) for C_2H_4 that declined from 2% at the start of electrolysis to 0 % during electrolysis (Figure S2.2.7). In contrast, Cu NW arrays exhibited an initially high j_{tot} (< 3 min) as the CuO NWs were reduced to Cu NWs, and subsequently a stable j_{tot} was observed over electrolysis of 5 h (Figure S2.2.7).

The faradaic efficiency of products in the electrocatalytic CO_2 reduction reaction as a function of Cu NW length is presented in Figure 2.8. It is well established that H_2 evolution is a competing reaction with CO_2 reduction in CO_2-saturated electrolytes, therefore the production of H_2 was also measured during electrolysis. We found that as the Cu NW arrays grew longer and more dense, the FE for H_2 production steadily decreased as the amount of CO_2 reduction products increased. In addition, the FE for C_2H_4 gradually increased with increasing the length of Cu NWs, as shown in Figure 2.8. Notably, the peak FE for C_2H_4 on 8.1-µm-length Cu NW arrays was maintained at 17.4% throughout the electrolysis (Figure S2.2.7), implying not only enhanced selectivity for C_2H_4 formation but also the stable catalytic activity for CO_2 reduction on Cu NWs. As we note in Figure 2.8, while HCOOH formation was observed on all different lengths of Cu NWs, n-propanol was detected on Cu catalysts with NW length of $\geq 2.4 \pm 0.56$ µm. With further increasing the length of Cu NWs, C_2H_6 formation (FE=2%) was observed, accompanying with the formation of ethanol. All the above

findings indicate that the selectivity for electrochemical reduction of CO_2 to hydrocarbons can be tuned on Cu NW arrays by varying the Cu NW length and density.
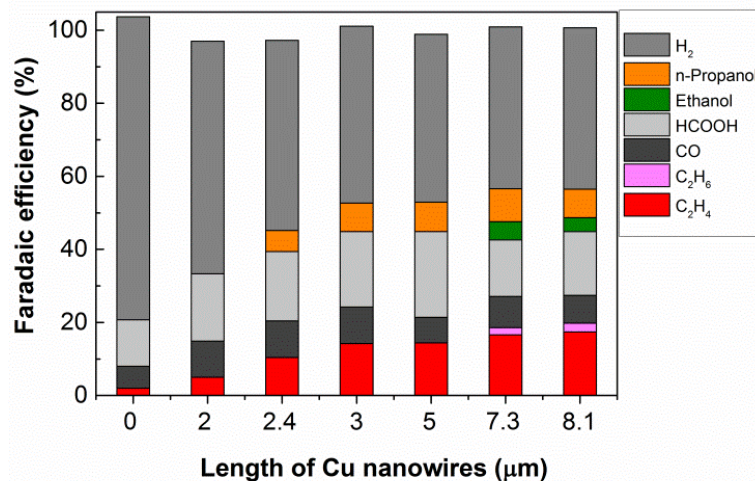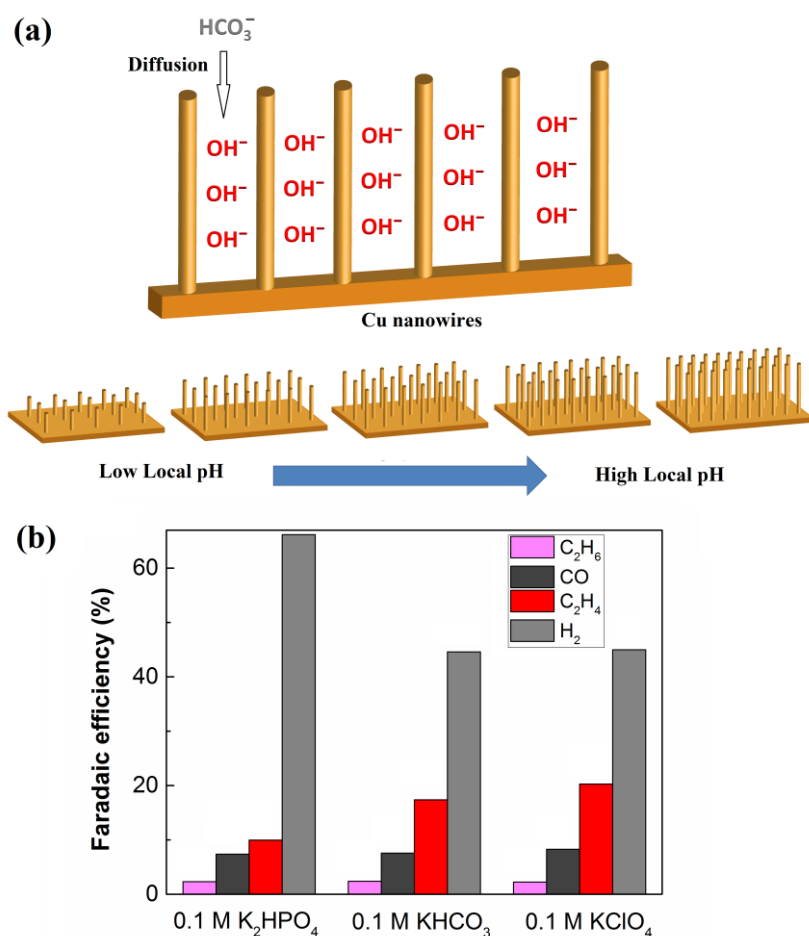

Figure 2.8 Faradaic efficiency for C_2H_4, C_2H_6, CO, HCOOH, Ethanol, n-Propanol and H_2 on Cu nanowire arrays with different lengths at -1.1 V vs. RHE in CO_2-saturated 0.1 M $KHCO_3$ electrolytes (0 µm nanowire represents Cu foil).

In order to understand the products distribution as a function of Cu NW length, a local pH effect is proposed. It is known that the pH rises locally at the electrode/electrolyte interface due to OH^- generation in the cathodic reactions (equations S(2.2.1-2.2.4)).[16] Thus, the local pH value close to the electrode becomes higher than the bulk pH.[11,16] However, HCO_3^- can neutralize the OH^- due to the reaction: $HCO_3^- + OH^- = CO_3^{2-} + H_2O$.[16] In this study, the increase of NW length also corresponds to an enhanced NW density with increasing synthesis time of the NWs (Figure S2.2.6). Thus, Cu NW arrays with an increase in nanowire length and density may cause a decrease in the diffusion of HCO_3^- into the Cu NW arrays and the diffusion of generated OH^- out of the Cu NW arrays, as shown in Figure 2.9a. This limitation of the diffusion process means a decreased amount of the neutralization reaction for OH^- generated near the catalyst surface, resulting in a higher local pH within the Cu NW arrays with increasing NW length and density.

To provide evidence of the local pH effect, CO_2 reduction was performed on 8.1-µm-length Cu NWs in 0.1 M K_2HPO_4, 0.1 M $KHCO_3$ and 0.1 M $KClO_4$ electrolytes, as shown in Figure 2.9b. These three electrolytes were chosen due to the difference in their buffer ability.

The buffer action of CO_2-saturated 0.1 M K_2HPO_4 can easily neutralize OH^-, keeping the local pH at a relatively low value. While HCO_3^- can neutralize the OH^-,[16] the buffer action of HCO_3^- is weaker than the previous one. ClO_4^- does not have any buffer ability, leading to a high local pH. In this study, the diffusion ability of the three different anionic species into the NW arrays is considered to be identical due to the same concentration of anionic species (0.1 M). Thus, the local pH at the electrode/electrolyte interface could be affected by the buffer ability of different electrolytes for Cu NWs (i.e. the local pH can be estimated as: $KClO_4 >$ $KHCO_3 > K_2HPO_4$).

**Figure 2.9** (a) Schematic illustration of the diffusion of electrolytes into Cu nanowire arrays. (b)Faradaic efficiency for C_2H_4, C_2H_6, CO and H_2 on Cu nanowire arrays (8.1 ± 1.3 µm) at -1.1 V vs. RHE in CO_2-saturated 0.1 M K_2HPO_4 (pH= 6.5), CO_2-saturated 0.1 M $KHCO_3$ (pH= 6.8) and CO_2-saturated 0.1 M $KClO_4$ (pH= 5.9) electrolytes, respectively.

We found that the product distribution on Cu NWs was significantly influenced by the different electrolytes. H_2 evolution (FE = 66%) was dramatically promoted in K_2HPO_4 electrolytes with suppressed CO_2 reduction, in contrast, $KHCO_3$ and $KClO_4$ solutions favored CO_2 reduction with a reduced FE for H_2 evolution. In addition, the FE of CO and C_2H_6 were roughly equal in the three different electrolytes. Interestingly, while the enhanced FE of 17.4% for C_2H_4 (FE for C_2H_4 is 10% in 0.1 M K_2HPO_4) was observed in 0.1 M $KHCO_3$, the highest FE of 20.3% for C_2H_4 was obtained in 0.1 M $KClO_4$ solutions (Figure 2.9b). Furthermore, the highest and lowest FE for ethanol formation were discovered in 0.1 M $KClO_4$ and 0.1 M K_2HPO_4, respectively (Figure S2.2.10). These observations (FE for C_2H_4 and ethanol: $KClO_4$ > $KHCO_3$ > K_2HPO_4) are consistent with previous studies on the Cu foil electrodes reported by Hori.[11,16] Thus, a locally high pH formed at Cu catalysts could favor the formation of C_2H_4 and alcohols. In addition, the low pH value at the electrode/electrolyte interface favors H_2 evolution.[11] We therefore conclude the enhanced selectivity for C_2H_4 with suppressed H_2 evolution on the longer and more dense Cu NW arrays is attributed to the high local pH formed in the Cu NW arrays (Figure 2.9a). In addition, the enhanced local pH on Cu NWs may contribute to the observed ethanol formation on the longer Cu NW length ($\geq$ 7.3 $\pm$ 1.3 μm)

To gain further insight into the mechanism of the products distribution on Cu NW arrays, we propose a reaction pathway for electrocatalytic CO_2 reduction, as shown in Scheme 2. It is generally accepted that CO is a key intermediate for the formation of hydrocarbons in the electrochemical reduction of CO_2.[11,24] However, it is generally accepted that the first electron transfer for the formation of the $CO_2^{\bullet-}$ shown in Scheme 2 is the rate determining step (RDS) in the electrochemical reduction of CO_2 to CO because the first electron transfer requires a much more negative potential compared to the following steps.[25] We have previously reported the enhanced stabilization for the $CO_2^{\bullet-}$ intermediate on Cu NW arrays.[21] The more active sites that are provided by longer Cu NWs may lead to the enhanced stabilization of the $CO_2^{\bullet-}$. In addition, the suppressed CO_2 reduction with enhanced H_2 evolution at low local pH caused by strong buffer action of K_2HPO_4 electrolytes (Figure 2.9b) may indicate the local pH formed in the Cu NW arrays may play a significant role in the CO_2 activation.
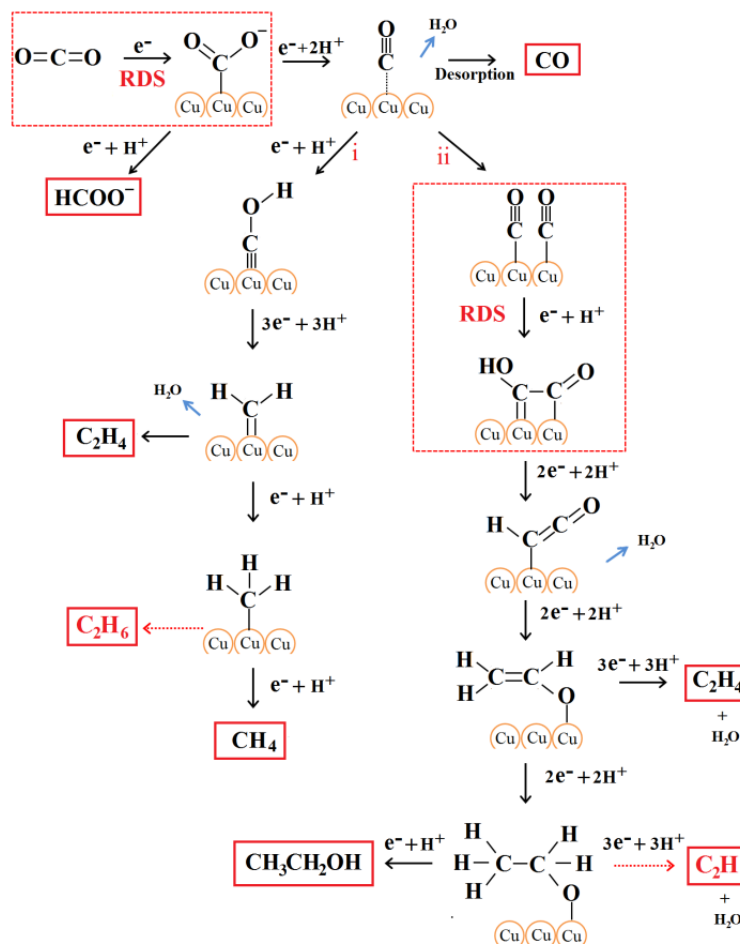
Scheme 2.2 Proposed reaction paths for electrocatalytic reduction of CO_2 on Cu nanowire arrays, with path (i), left, showing COH formation, and path (ii), right, showing CO dimerization. In path (i), 2 CH_2 and 2 CH_3 intermediates are required for C_2H_4 and C_2H_4 formation, respectively.
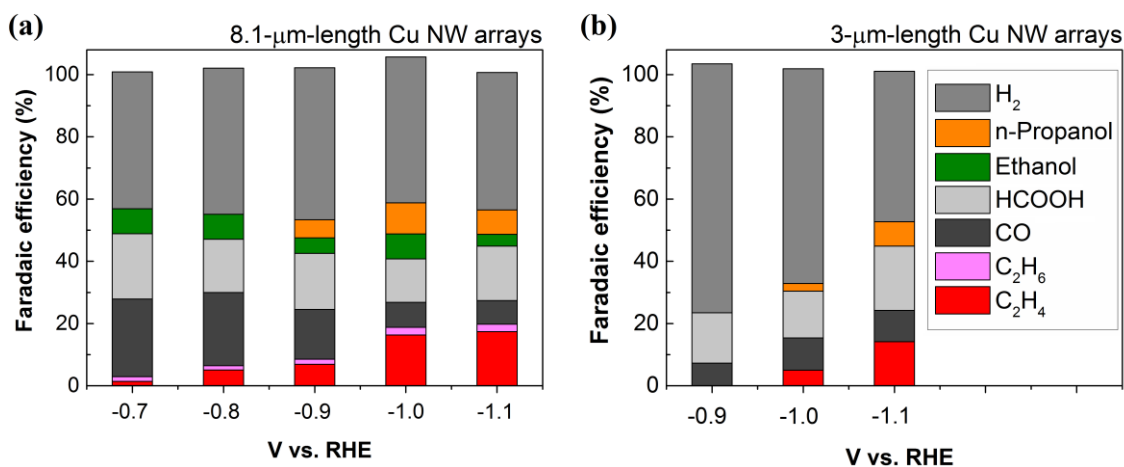
Figure 2.10 Faradaic efficiency of the products at various potentials in CO_2-saturated 0.1 M $KHCO_3$.

Furthermore, the FE of products as a function of potential was plotted for 8.1-µm-length Cu NWs (Figure 2.10a). We found that the FE for CO decreased from -0.7 V to -1.1 V vs. RHE, along with enhanced FE for C_2H_6 and C_2H_4. In addition, the n-propanol was detected at potentials of $\leq$ -0.9 V. These observations imply that the formation of hydrocarbons from the CO intermediate is more favorable at more negative potentials.

It was reported that one possible reaction path for C_2H_4 formation is through a CH_2 dimerization.[10] Furthermore, more detailed reaction pathway for C_2H_4 has been investigated theoretically by density functional theory (DFT), which provides a pathway through a COH intermediate shown in Scheme 2.2 (path i, left).[26] Recently, a CO coupling mechanism[18,19,24] has been suggested as an alternative route to C_2H_4 through a CO dimer adsorbed on Cu, as shown in Scheme 2.2 (path ii, right). Thus, C_2H_4 formation could have two potential pathways, (i) via a COH intermediate and (ii) via a CO dimerization pathway. It is critical to understand which pathway is preferred for the Cu NW arrays to determine the mechanism of the selectivity for hydrocarbons. When comparing the two pathways, it can be seen that CH_4 is only formed through the COH intermediate pathway (path i). In all our experiments, C_2H_4 was observed without any detected CH_4 formation, which may indicate that C_2H_4 formation on Cu NWs is mainly from the CO dimerization reaction path (path ii).

In addition, the formation of C_2H_6 has not been reported in the electrocatalytic reduction of CO_2 on smooth Cu,[7,8,11] but was observed as a minor product on nanostructured Cu catalysts.[3,27,28] However, a reaction pathway towards C_2H_6 has never been reported. Here we propose two possible routes for C_2H_6 formation via CH_3 dimerization and CH_3CH_2O intermediate in Scheme 2.2. In our research, C_2H_6 formation appeared on longer Cu NWs (NW $\geq$ 7.3±1.3 µm), and was always accompanied with the formation of ethanol without any observed CH_4 formation (Figure 2.8), which implies that C_2H_6 and ethanol may be formed through the same intermediate (CH_3CH_2O) in the CO dimerization pathway[18], as we proposed in Scheme 2.2.

As discussed above, the formation of C_2H_4, C_2H_6 and ethanol could be mainly from the CO dimerization reaction pathway in this study. The rate determining step for the formation of C_2H_4 in the CO dimerization pathway is CO coupling (Scheme 2.2).[24] It has been demonstrated that the CO coupling step is favored at a high local pH near the catalyst surface.[20] In addition, more products (such as C_2H_6 and ethanol) are detected on longer Cu NW arrays at various potentials shown in Figure 2.10, indicating that the enhanced local pH

on Cu NWs may contribute to the observation of C_2H_6 and ethanol. Therefore, the higher local pH in the Cu NW arrays with an increase in nanowire length and density could improve the formation of C_2H_4, C_2H_6 and ethanol through the enhanced CO coupling mechanism which is formed in a high local pH due to the nanowire morphology.

2.2.4 Conclusions

In summary, the effect of Cu nanowire morphology has been explored for the electrochemical reduction of CO_2. With increasing the Cu nanowire length ($\geq$2.4 $\pm$0.56 µm), the formation of n-propanol was detected along with CO, HCOOH and C_2H_4. Furthermore, C_2H_6 formation appeared on longer Cu nanowires ($\geq$ 7.3 $\pm$ 1.3 µm), accompanying with the formation of ethanol. We propose a route to C_2H_6 from the intermediate (CH_3CH_2O) in the CO dimerization pathway. More importantly, Cu nanowire arrays exhibited an increased selectivity for C_2H_4 with increasing the Cu nanowire length and density, which is ascribed to the improved formation of C_2H_4 through a CO coupling mechanism caused by an enhanced local pH in the Cu nanowire arrays. This study shows that the selectivity in the electrocatalytic reduction of CO_2 to hydrocarbons could be tuned on Cu nanowire arrays by varying the Cu nanowire length, providing a promising efficient approach for systematically controlling hydrocarbon formation via the electrochemical reduction of CO_2.

References

[1]   D. T. Whipple, P. J. a. Kenis, *J. Phys. Chem. Lett.* **2010**, *1*, 3451–3458.

[2]   J. L. DiMeglio, J. Rosenthal, *J. Am. Chem. Soc.* **2013**, *135*, 8798–801.

[3]   C. W. Li, M. W. Kanan, *J. Am. Chem. Soc.* **2012**, *134*, 7231–7234.

[4]   Y. Chen, C. W. Li, M. W. Kanan, *J. Am. Chem. Soc.* **2012**, *134*, 19969–19972.

[5]   Y. Chen, M. W. Kanan, *J. Am. Chem. Soc.* **2012**, *134*, 1986–1989.

[6]   J. Qiao, Y. Liu, F. Hong, J. Zhang, *Chem. Soc. Rev.* **2014**, *43*, 631–675.

[7]   M. Gattrell, N. Gupta, A. Co, *J. Electroanal. Chem.* **2006**, *594*, 1–19.

[8]   K. P. Kuhl, E. R. Cave, D. N. Abram, T. F. Jaramillo, *Energy Environ. Sci.* **2012**, *5*, 7050–7059.

[9]   K. Manthiram, B. J. Beberwyck, A. P. Alivisatos, *J. Am. Chem. Soc.* **2014**, *136*, 13319–13325.

[10]   Y. Hori, R. Takahashi, Y. Yoshinami, A. Murata, *J. Phys. Chem. B* **1997**, *101*, 7075–7081.

[11]   Y. Hori, in *Electrochem. CO2 Reduct. Met. Electrodes* (Ed.: E. Vayenas, C. G., White, R. E., Gamboa-Aldeco, M. E.), Springer New York, **2008**, p. Vol. 42, p 89.

[12]   S. Zhang, P. Kang, S. Ubnoske, M. K. Brennaman, N. Song, R. L. House, J. T. Glass, T. J. Meyer, *J. Am. Chem. Soc.* **2014**, *136*, 7845–7848.

[13]   S. Zhang, P. Kang, T. J. Meyer, *J. Am. Chem. Soc.* **2014**, *136*, 1734–1737.

[14]   H.-E. Lee, K. D. Yang, S. M. Yoon, H.-Y. Ahn, Y. Y. Lee, H. Chang, D. H. Jeong, Y.-S. Lee, M. Y. Kim, K. T. Nam, *ACS Nano* **2015**, *9*, 8384–8393.

[15]   A. A. Peterson, J. K. Nørskov, *J. Phys. Chem. Lett.* **2012**, *3*, 251–258.

[16]   Y. Hori, A. Murata, R. Takahashi, *J. Chem. Soc. Faraday Trans. 1 Phys. Chem. Condens. Phases* **1989**, *85*, 2309.

[17]   K. J. P. Schouten, Z. Qin, E. Pérez Gallent, M. T. M. Koper, *J. Am. Chem. Soc.* **2012**,

134, 9864–9867.

[18]   F. Calle-Vallejo, M. T. M. Koper, *Angew. Chemie* **2013**, *125*, 7423–7426.

[19]   K. J. P. Schouten, E. Pérez Gallent, M. T. M. Koper, *J. Electroanal. Chem.* **2014**, *716*, 53–57.

[20]   R. Kas, R. Kortlever, H. Yılmaz, M. T. M. Koper, G. Mul, *ChemElectroChem* **2015**, *2*, 354–358.

[21]   M. Ma, K. Djanashvili, W. A. Smith, *Phys. Chem. Chem. Phys.* **2015**, *17*, 20861–20867.

[22]   W. Zhang, X. Wen, S. Yang, Y. Berta, Z. L. Wang, *Adv. Mater.* **2003**, *15*, 822–825.

[23]   C. Lin, Y. Lai, D. Mersch, E. Reisner, *Chem. Sci.* **2012**, *3*, 3482–3487.

[24]   K. J. P. Schouten, Y. Kwon, C. J. M. van der Ham, Z. Qin, M. T. M. Koper, *Chem. Sci.* **2011**, *2*, 1902.

[25]   Q. Lu, J. Rosen, Y. Zhou, G. S. Hutchings, Y. C. Kimmel, J. G. Chen, F. Jiao, *Nat. Commun.* **2014**, *5*, 3242.

[26]   X. Nie, M. R. Esopi, M. J. Janik, A. Asthagiri, *Angew. Chemie* **2013**, *125*, 2519–2522.

[27]   W. Tang, A. a Peterson, A. S. Varela, Z. P. Jovanov, L. Bech, W. J. Durand, S. Dahl, J. K. Nørskov, I. Chorkendorff, *Phys. Chem. Chem. Phys.* **2012**, *14*, 76–81.

[28]   S. Sen, D. Liu, G. T. R. Palmore, *ACS Catal.* **2014**, *4*, 3091–3095.

Supplementary information for Chapter 2 (2.1)
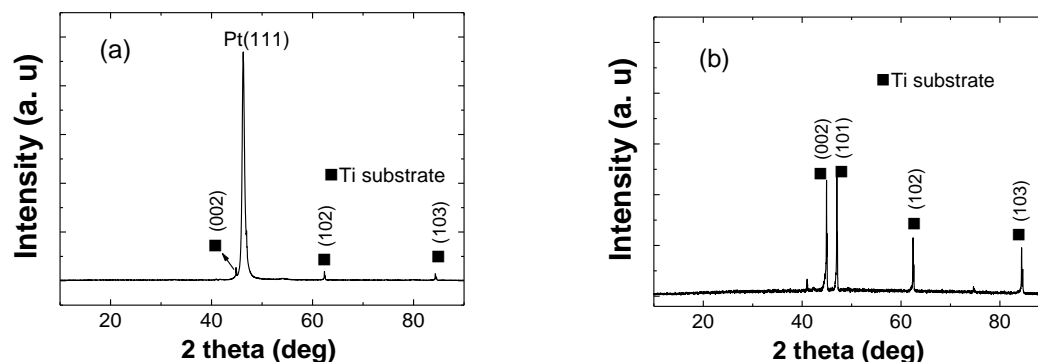
Pt counter electrode

Figure S2.1.1 XRD patterns of Pt film (a) deposited by magnetron sputtering and Ti foil (b).

Pt films (~160 nm) were deposited on Ti foils by using direct current magnetron sputtering (60 W) at 0.3 Pa for 20 min (deposition rate is 0.133 nm/s). The XRD pattern of the Pt film sputtered on Ti foil was shown in Figure S2.1.1 (a). The Pt film coated on Ti foil was used as the counter electrode (anode) in the three-electrode configuration measurement.

Surface preparation of polycrystalline Cu

It is important to remove impurities on the surface of Cu foil.[1,2] SEM images of the copper electrode surface are displayed after polishing by sandpaper in Figure S2.1.2 (a) and subsequent electropolishing in Figure S2.1.2 (b) in order to have a surface free of impurities. In our study the Cu foils were electropolished at 4.0 V for 5 min in 85% phosphoric acid.[3]
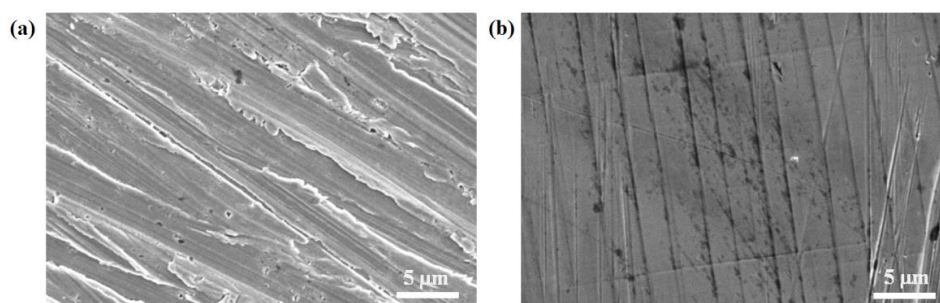
Figure S2.1.2 SEM images of Cu foil before (a) and after (b) electropolishing in 85 % phosphoric acid.

The annealing temperature and time

Some examples of annealed $Cu(OH)_2$ nanowires at different annealing conditions were shown in Figure S2.1.3.

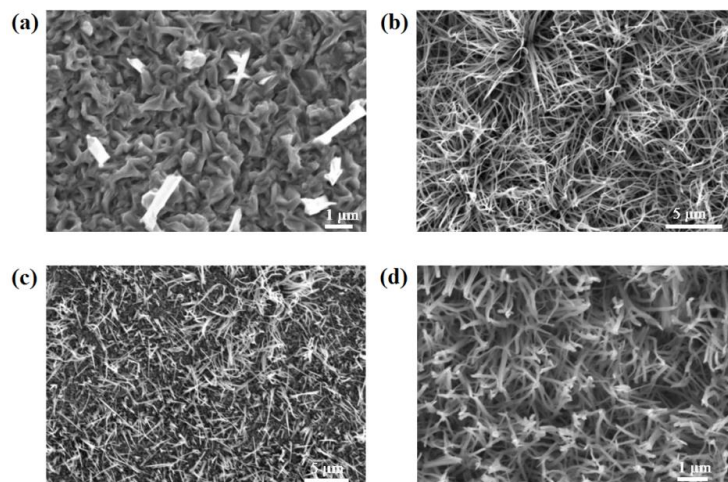Figure S2.1.3 SEM images of annealed $Cu(OH)_2$ nanowires in argon at 500 ℃ (a) and 300 ℃ (b) for 1 hour, and in air at 450 ℃ for 1 hour (c) and 230 ℃ in air for 2 hours (d), respectively.
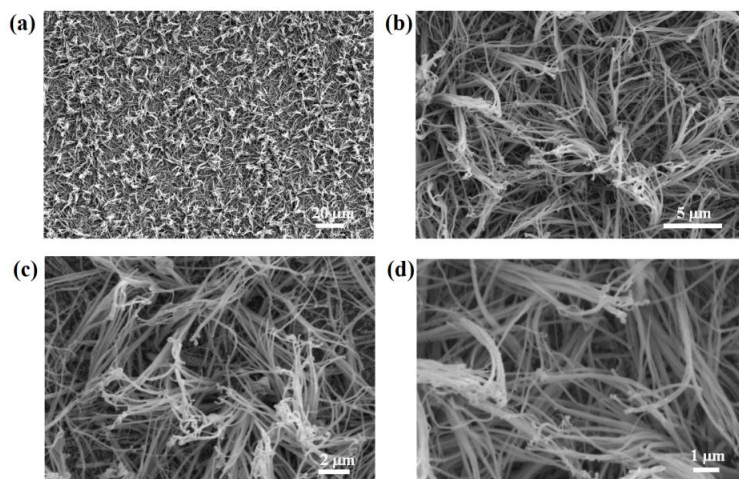
SEM images of nanowires after electrolysis.

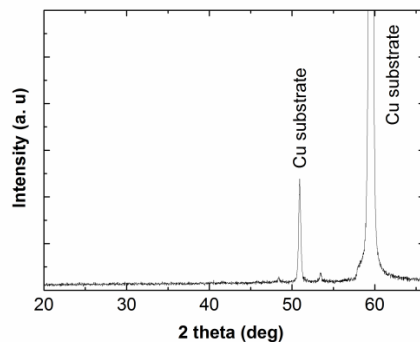Figure S2.1.4 SEM images of CuO nanowires after CO_2 reduction electrolysis.

Figure S2.1.5 XRD pattern of the CuO nanowire arrays after CO$_2$ reduction electrolysis.
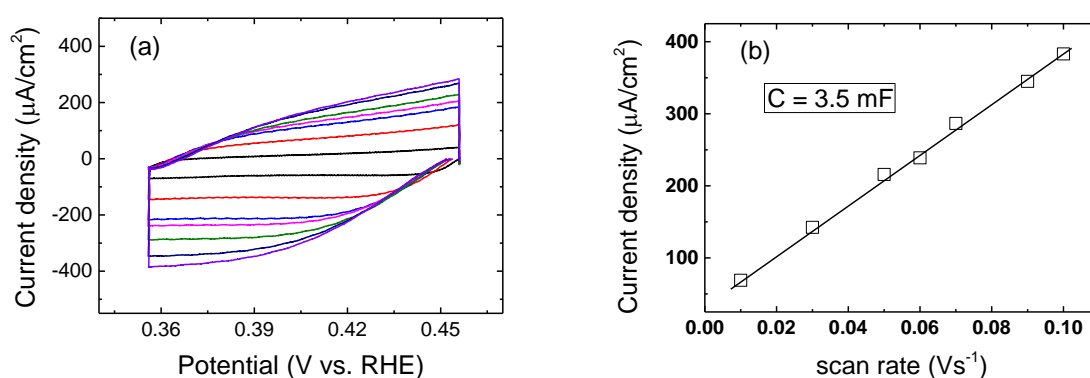

Figure S2.1.6 Determination of double-layer capacitance for the Cu nanowire arrays. (a) the cyclic voltammograms were measured in a non-faradaic region of the voltammogram at the following scan rate: 0.01, 0.03, 0.05, 0.06, 0.07, 0.09 and 0.1 V/s in N$_2$ bubbled 0.1 M phosphate buffer. The working electrode was held at each potential vertex for 15 s before starting the next sweep. (b) The relationship between the current density and the CV scan rate.
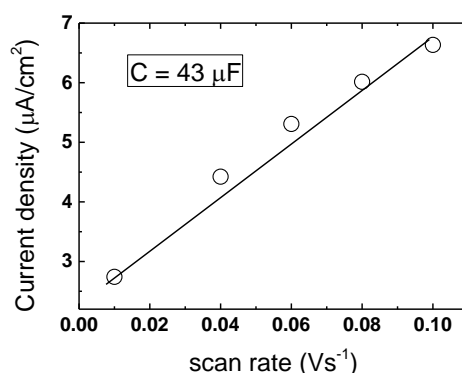

Figure S2.1.7 The relationship between the current density and the CV scan rate for polycrystalline Cu.
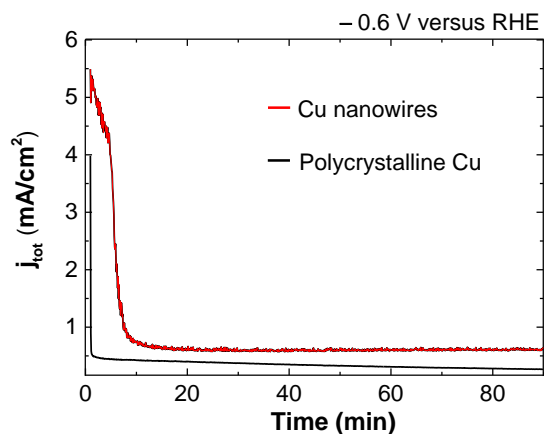
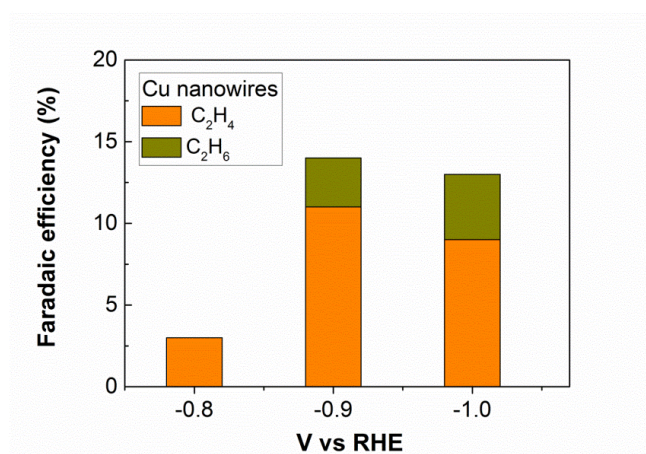Figure S2.1.8 CO_2 reduction current as a function of time at -0.6 V vs. RHE.

Figure S2.1.9 Faradaic efficiency for C_2H_4 and C_2H_6 at various potentials in CO_2-saturated 0.1 M $KHCO_3$ electrolytes at ambient temperature and pressure.
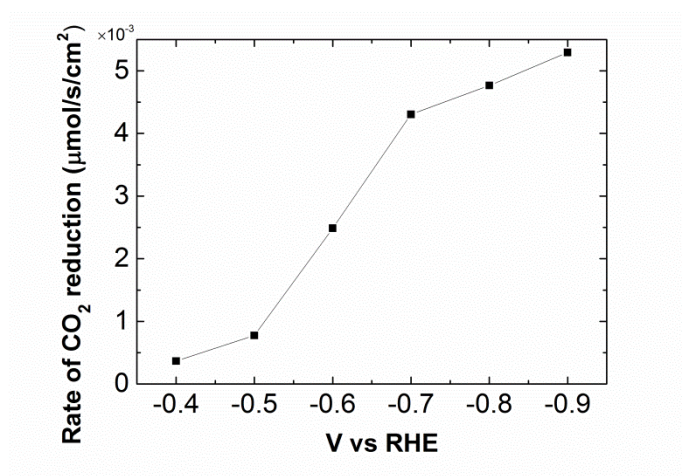

Figure S2.1.10 Total rate of CO_2 reduction as a function of potentials.

The total rate of CO_2 reduction is calculated at a given potential as follow:

$$RR_{CO_2} = \frac{J_{CO}}{2F} + \frac{J_{HCOOH}}{2F} + \frac{J_{C_2H_4}}{6F} + \frac{J_{C_2H_6}}{7F} \qquad \text{(S2.1.1)}$$

where J_{CO}, J_{HCOOH}, $J_{C_2H_4}$ and $J_{C_2H_6}$ are the partial current density for each reduction product (CO, $HCOOH$, C_2H_4 and C_2H_6) of CO_2, and F is the faraday constant. The partial current density for each reduction product of CO_2 is calculated through multiplying the total geometric current density by the faradaic efficiency for each product at a given potential.
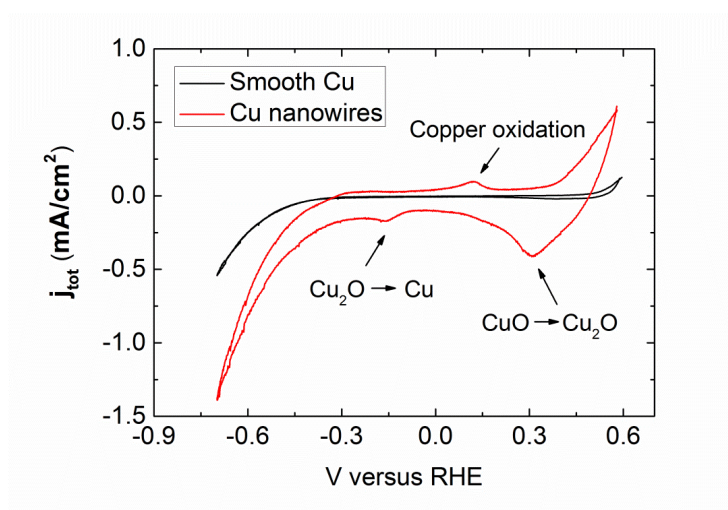

Figure S2.1.11 Cyclic voltammetry (CV) of smooth Cu and Cu nanowire arrays in CO_2-saturated 0.1 M $KHCO_3$ electrolytes at ambient temperature and pressure (scan rate is 0.02 V/s).

References

[1]   K. P. Kuhl, E. R. Cave, D. N. Abram, T. F. Jaramillo, *Energy Environ. Sci.* **2012**, *5*, 7050–7059.

[2]   M. Gattrell, N. Gupta, A. Co, *J. Electroanal. Chem.* **2006**, *594*, 1–19.

[3]   C. W. Li, M. W. Kanan, *J. Am. Chem. Soc.* **2012**, *134*, 7231–7234.

Supplementary information for Chapter 2 (2.2)

Materials

(NH$_4$)$_2$S$_2$O$_8$ ($\geq$98.0%), NaOH (99.99%), KHCO$_3$ ($\geq$99.95%), KClO$_4$ ($\geq$99.99%) and K$_2$HPO$_4$ ($\geq$99.999%) were purchased from Sigma Aldrich. All chemicals were used in this study without further purification. Copper foil (99.9999%) were purchased from Alfa Aesar.

Local pH

CO$_2$ is electrochemically reduced to a variety of major products in CO$_2$ saturated-aqueous solutions according to the reactions:

$$CO_2 + H_2O + 2e^- \rightarrow CO + 2OH^- \qquad \text{(-0.11 V vs. RHE)} \qquad \text{(S2.2.1)}$$

$$CO_2 + H_2O + 2e^- \rightarrow HCOO^- + OH^- \qquad \text{(-0.03 V vs. RHE)} \qquad \text{(S2.2.2)}$$

$$2CO_2 + 8H_2O + 12e^- \rightarrow C_2H_4 + 12OH^- \qquad \text{(0.08 V vs. RHE)} \qquad \text{(S2.2.3)}$$

H$_2$ evolution is a competing reaction with CO$_2$ reduction in CO$_2$-saturated electrolytes. Thus, water could be reduced to H$_2$ on Cu according to the following reaction:

$$2H_2O + 2e^- \rightarrow H_2 + 2OH^- \qquad \text{(0 V vs. RHE)} \qquad \text{(S2.2.4)}$$

OH$^-$ ions are released at the electrode in cathodic reactions according to the above reactions, resulting in the fact that the pH rises locally at the electrode/electrolyte interface.[1,2] Thus, the actual pH near the electrode is higher that of the bulk owing to the release of OH$^-$ in the electrode reactions.[1,2]
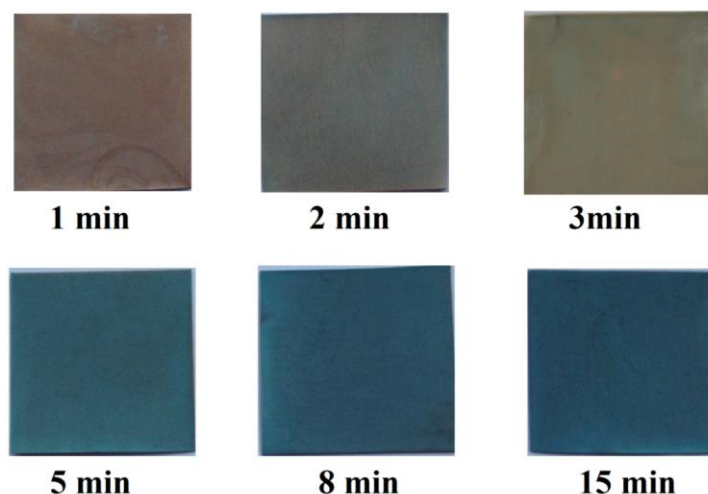
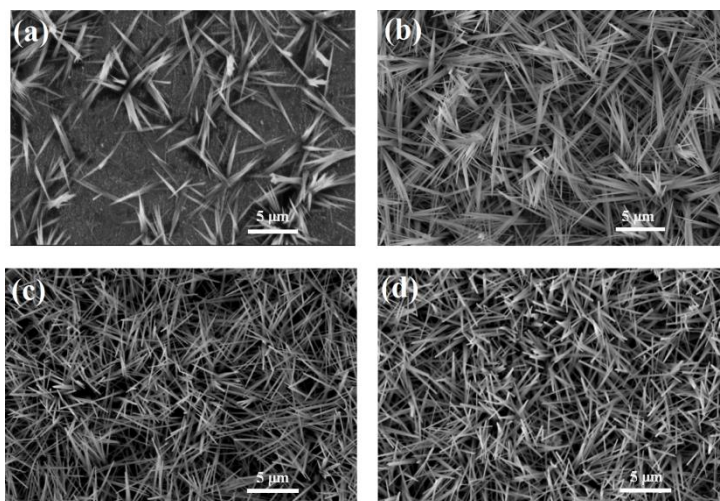Figure S2.2.1 Digital images of Cu(OH)$_2$ nanowires with synthesis time of 1, 2, 3, 5, 8, 15 min, respectively.

Figure S2.2.2 SEM images of Cu(OH)$_2$ nanowires on Cu foils with synthesis time of 0.5 (a), 3 (b), 5 (c) and 8 min (d).

The measurement of Cu(OH)$_2$ nanowire length

Cu(OH)$_2$ nanowire was removed from the surface of Cu foil to carbon tapes (double sides carbon tape) by pressing Cu foil (nanowires on the surface of Cu foil) on carbon tape, and the nanowires stuck to the surface of carbon tapes. Thus, the length of Cu(OH)$_2$ nanowire was measured by using scanning electron microscope (SEM, JEOL JSM-6010LA). Figure S2.2.3 shows the nanowires on carbon tape substrates. Here, I measured more than 100 different nanowires for each sample to get the length histograms of Cu(OH)$_2$ nanowires, as presented in Figure S2.2.4.
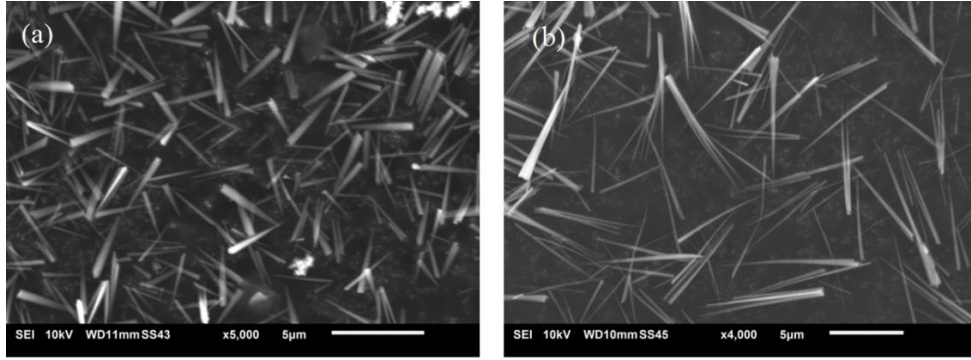
Figure S2.2.3 SEM images of Cu(OH)$_2$ nanowires with synthesis time of 2 (a) and 5 min (b).
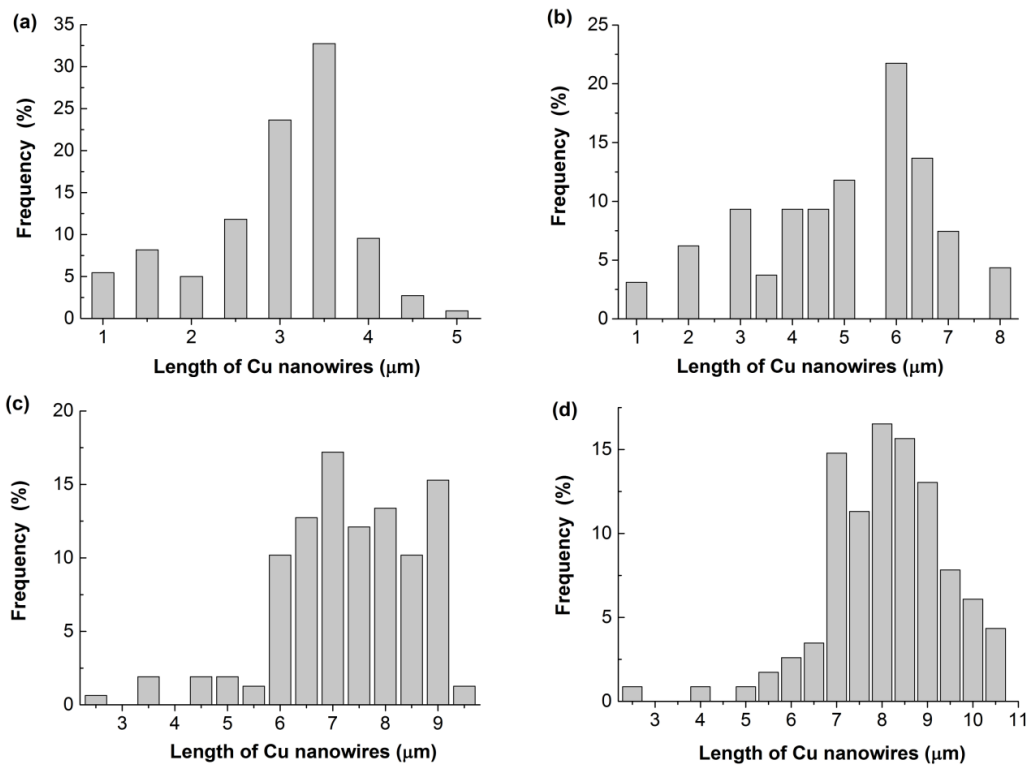
Figure S2.2.4 Length histograms of Cu(OH)$_2$ nanowires in the samples with fabrication time of (a) 2 min, (b) 3 min, (c) 5 min, (d) 8 min.

The average length of nanowire can be calculated as follow:

$$l = \sum (L_x \times F_x) \qquad\qquad (S2.2.5)$$

where l, L_x and F_x are the average length of nanowire, the specific length of nanowire measured from SEM and the percentage of the specific length of nanowire.

The standard deviation of the length of nanowire can be obtained from equation:

$$\partial = \sqrt{\sum F_x(L_x - l)^2} \qquad (S2.2.6)$$

Table S2.2.1 The average length of $Cu(OH)_2$ nanowire under different fabrication time.

Synthesis time (min)	Average Length (µm)	Standard Deviation (µm)
0.5	2.0	1
1	2.4	0.56
2	3	0.87
3	5	1.68
5	7.3	1.3
8	8.1	1.3
15	8.5	1.1

The density of nanowire arrays

CuO nanowires were fabricated by annealing the $Cu(OH)_2$ nanowire arrays at 150 °C for 2 hours in air.[3] The resulting CuO nanowire arrays were directly used in electrochemical reduction of CO_2, and were electrochemically reduced to Cu nanowires during electrolysis.[3] The charge used for the reduction of CuO to Cu can be calculated by equation:

$$Q = 2F \times \left(\frac{m}{M}\right) \qquad (S2.2.7)$$

where, F, M and m are Faraday constant, the molar mass and the mass of CuO, respectively. This equation (S2.2.7) can be rewritten as:

$$Q = 2F \times \left(\frac{\rho \times n \times l \times A}{M}\right) \qquad (S2.2.8)$$

Where, ρ is mass density of CuO. The n is the total number of nanowire involved in electrolysis (geometric surface area involved in electrolysis is constant). The l and A are the length and cross-section area of CuO nanowires, respectively. Here, Cu nanowire length is identical to the corresponding $Cu(OH)_2$ nanowire length and we assume that the A is constant for all different samples.

The electrodes exhibited an initially high current density as the CuO nanowires were reduced to Cu nanowires, and subsequently a stable current density during electrolysis, as shown in Figure S2.2.5. Thus, we can get the total charge used for reducing CuO to Cu according to the initial high current in Figure S2.2.5. $Q_{3\mu m}$ and $Q_{7.3\mu m}$ are 0.71 C and 1.93 C, respectively. From the equation (S2.2.8), we can get

$$\frac{Q_{7.3\mu m}}{Q_{3\mu m}} = \frac{n_{7.3\mu m}l_{7.3\mu m}}{n_{3\mu m}l_{3\mu m}} \qquad (S2.2.9)$$

According to the equation (S2.2.9), $n_{7.3\mu m}/n_{3\mu m}$ is 1.12

$$\frac{n_{8.1\mu m}}{n_{7.3\mu m}} = \frac{l_{7.3\mu m}}{l_{8.1\mu m}} \times \frac{Q_{8.1\mu m}}{Q_{7.3\mu m}} = \frac{7.3\mu m}{8.1\mu m} \times \frac{2.28\ C}{1.93\ C} \qquad (S2.2.10)$$

Here, $n_{8.1\mu m}/n_{7.1\mu m}$ is 1.06.

$$\frac{n_{8.5\mu m}}{n_{8.1\mu m}} = \frac{l_{8.1\mu m}}{n_{8.5\mu m}} \times \frac{Q_{8.5\mu m}}{Q_{8.1\mu m}} = \frac{8.1\mu m}{8.5\mu m} \times \frac{3.03\ C}{2.28\ C} \qquad (S2.2.11)$$

Thus, $n_{8.5\mu m}/n_{8.1\mu m}$ is 1.27.

In this way, we can get the nanowire density as a function of synthesis time, as shown in Figure S2.2.6. The color of the sample is getting darker blue with increasing synthesis time of nanowires (Figure S2.2.1), which is consistent with the fact that the higher density and longer length of nanowire with increased synthesis time.

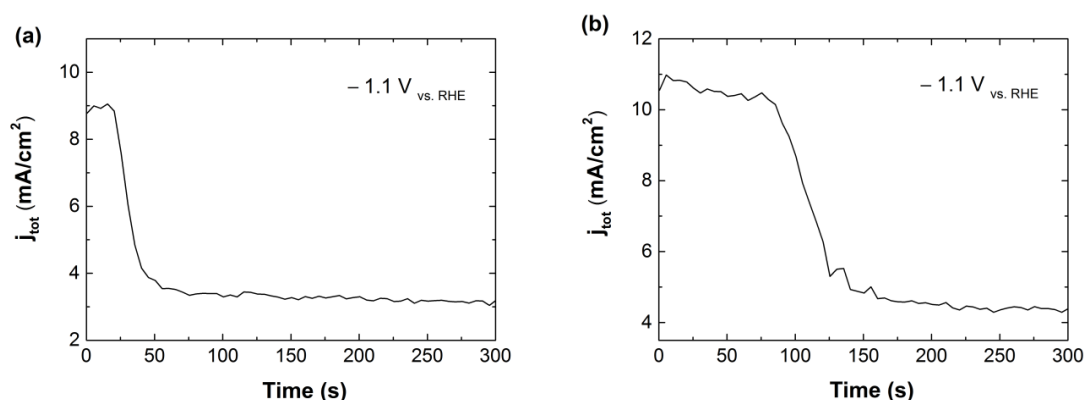Figure S2.2.5 CO_2 reduction current as a function of time on CuO-derived Cu nanowires with length of (a) 3 µm and (b) 7.3 µm at -1.1 V vs. RHE, respectively.
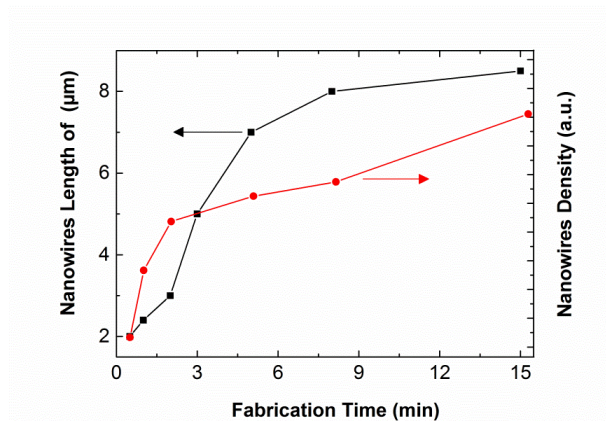
Figure S2.2.6 Cu(OH)$_2$ nanowire length and density as a function of synthesis time.

CO₂ reduction performance
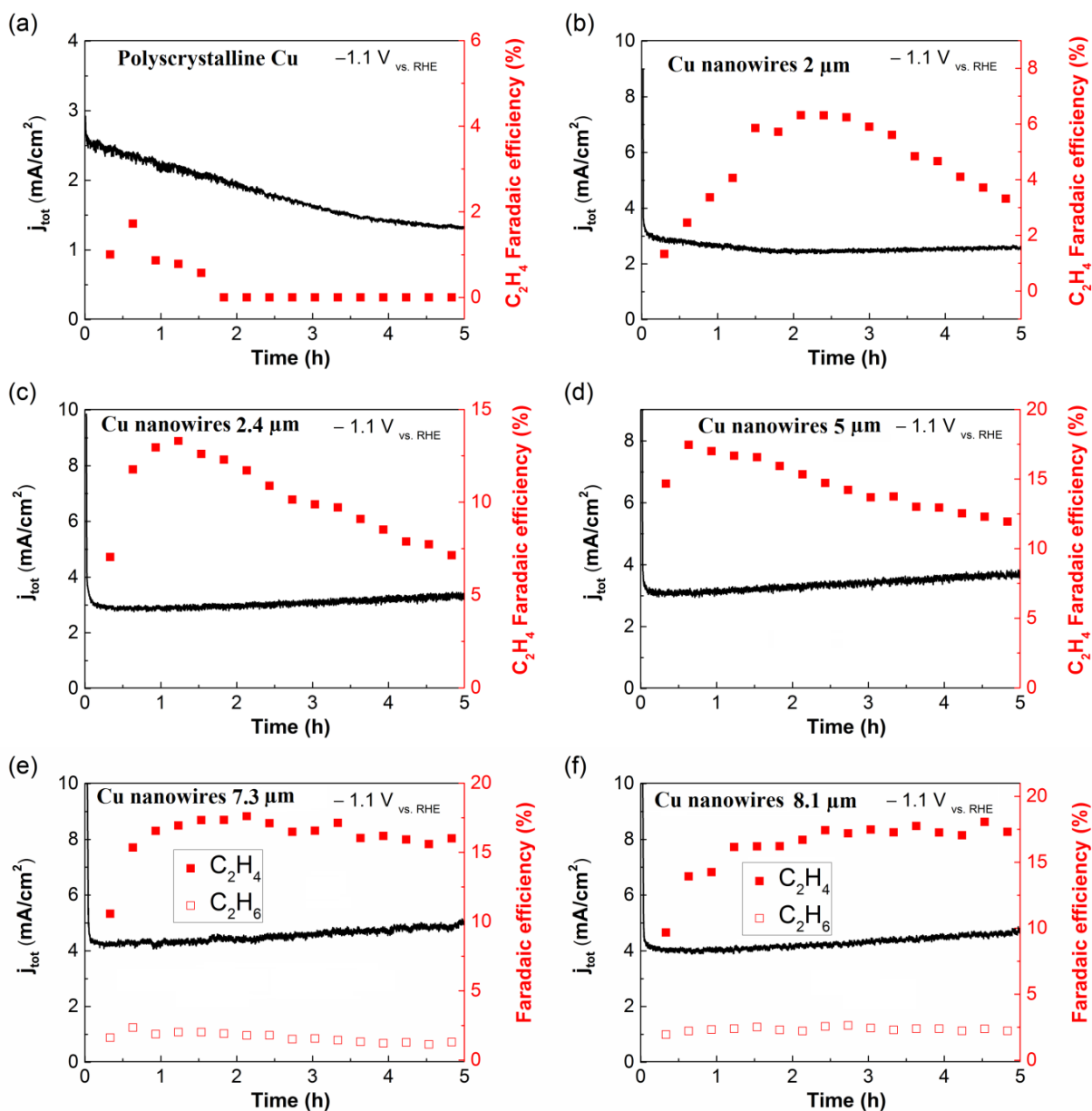
Figure S2.2.7 CO$_2$ reduction performance of Cu nanowires. CO$_2$ reduction activity of polycrystalline Cu (a) and Cu nanowires with increased length (b-f) at -1.1 V vs. RHE in CO$_2$-saturated 0.1 M KHCO$_3$ electrolytes. The geometric current density is shown on the left axis and the faradaic efficiency is shown on the right axis (■ and □ represent faradaic efficiency for C$_2$H$_4$ and C$_2$H$_6$ respectively).

Figure S2.2.8 Faradaic efficiency for C_2H_4 (a) and H_2 (b) on Cu nanowire arrays as a function of nanowire length at -1.1 V vs. RHE in CO_2-saturated 0.1 M $KHCO_3$ electrolytes.
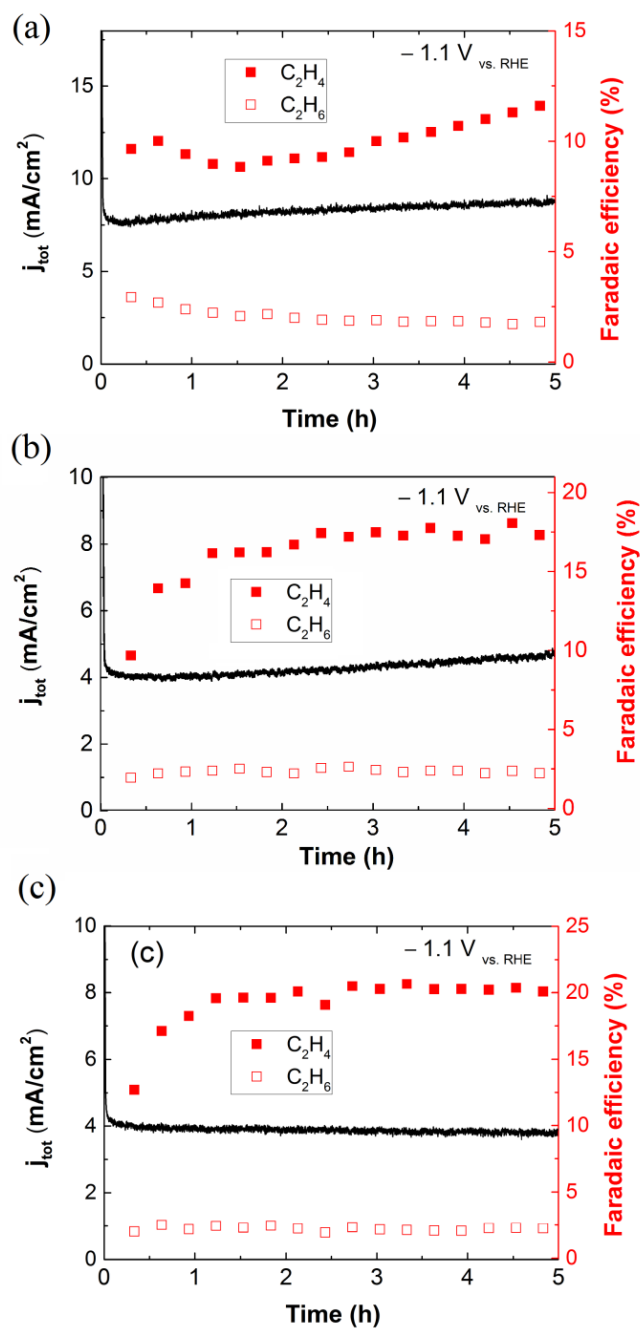
Figure S2.2.9 CO_2 reduction performance of 8.1-µm-length Cu nanowire arrays at -1.1 V vs. RHE in CO_2-saturated 0.1 M K_2HPO_4 (a), CO_2-saturated 0.1 M $KHCO_3$ (b) and CO_2-saturated 0.1 M $KClO_4$ (c), respectively. The geometric current density is shown on the left axis and the faradaic efficiency is shown on the right axis (■ and □ represent faradaic efficiency for C_2H_4 and C_2H_6 respectively).
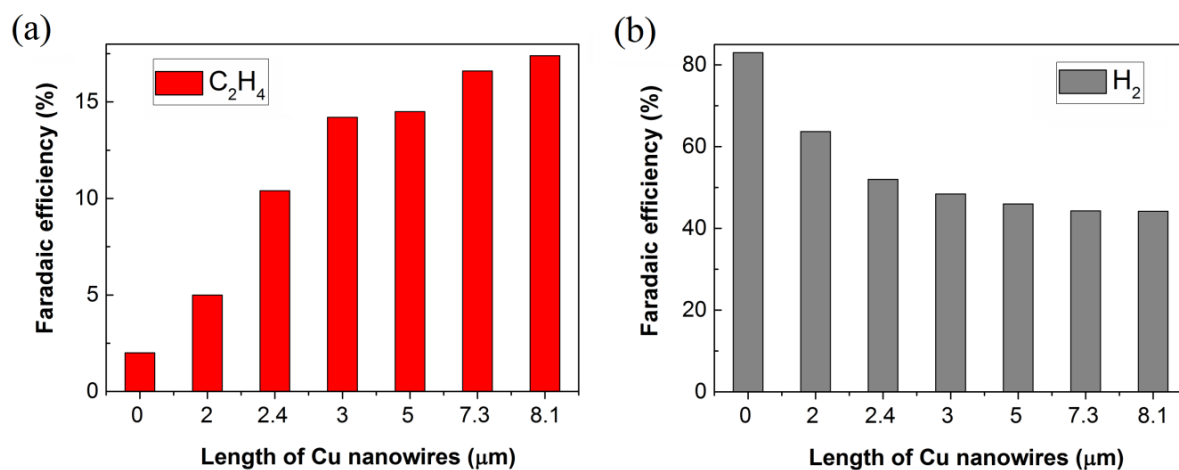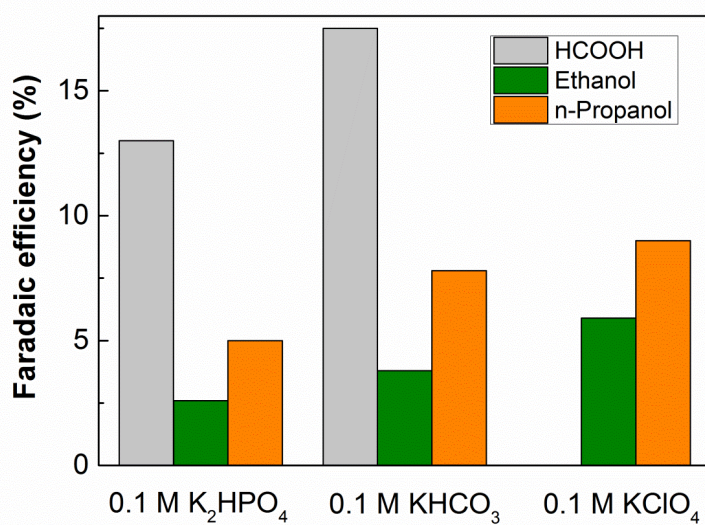
Figure S2.2.10 Faradaic efficiency for HCOOH, Ethanol and n-Propanol on Cu nanowire arrays (8.1 ± 1.3 μm) at -1.1 V vs. RHE in CO_2-saturated 0.1 M K_2HPO_4 (pH= 6.5), CO_2-saturated 0.1 M $KHCO_3$ (pH= 6.8) and CO_2-saturated 0.1 M $KClO_4$ (pH= 5.9) electrolytes, respectively.

Figure S2.2.11 The geometric current density as a function of potential in CO_2-saturated 0.1 M $KHCO_3$ (pH= 6.8).

NMR analysis

NMR spectra were obtained at Agilent MR400DD2 NMR spectrometer operating at 400 MHz. For the preparation of the samples, 50 μL of D_2O containing a known concentration of internal reference t-BuOH were added to 450 μL the electrolyte solutions. Water suppression hard pulse sequence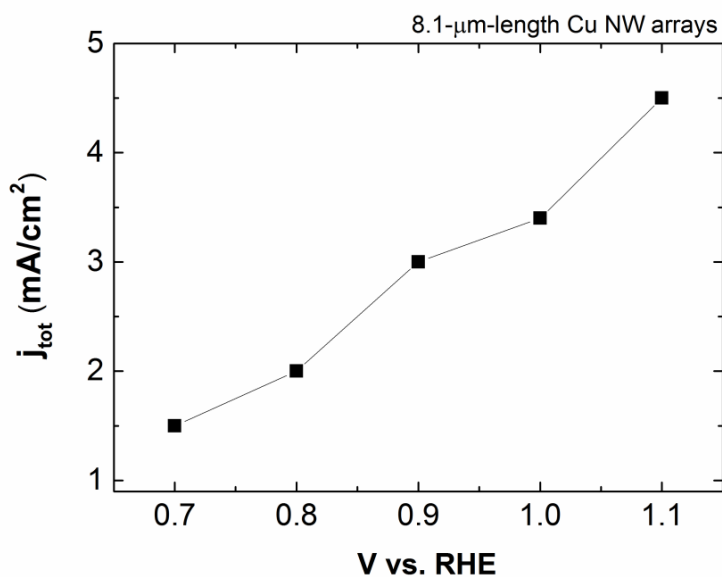 was applied during the acquisition of the ^{1}H NMR spectra with 2 s saturation delay, 2 s relaxation delay, 2.5 s acquisition time, and spectral window of 6400 Hz. After collection of 8 scans, peak areas were integrated and the concentration of the solutes can be calculated by considering the difference in the number of protons in the reference compound and that of the product. Chemical shifts (δ) are reported in ppm with respect to internal standard set at 1.2 ppm. Thus, the ^{1}H NMR spectra (Figure S2.2.12) allows for the identification of products.

Table S2.2.2 NMR data used for the calculation of concentration of the products.

Compound	Number of H (n)	Chemical Shift (δ)	Multiplicity	Coupling constant (Hz)
t-BuOH (ref)	9	1.2	singlet	-
Formic Acid	1 (HCO)	8.45	singlet	-
Ethanol	3 (CH_3)	1.13	triplet	7.24
	2 (CH_2-O)	3.52	quartet	7.24
n-Propanol	3 (CH_3)	0.84	triplet	7.76
	2 (CH_2)	1.41	multiplet	7.44
	2 (CH_2-O)	3.43	triplet	6.66

The concentration of products can be calculated by equation:

$$\frac{9 \times C_{Ref}}{(Peak\ area)_{Ref}} = \frac{n \times C_{product}}{(Peak\ area)_{product}} \qquad (S2.2.12)$$

where $C_{product}$ and n are the concentration of product and the number of corresponding protons in the of related product (Table S2.2.2), respectively. C_{Ref} is the concentration of reference t-

BuOH (0.0825 mM). (Peak area)$_{Ref}$ and (Peak area)$_{product}$ represent the integrals for *t*-BuOH (reference) and product in the ^{1}H NMR spectra, respectively. Thus, *n* will be 9 (3xCH$_3$) for tBuOH and 1 (COH), 3 (CH$_3$), and 3 (CH$_3$) at chemical shifts of 8.45, 1.13 and 0.84, respectively.
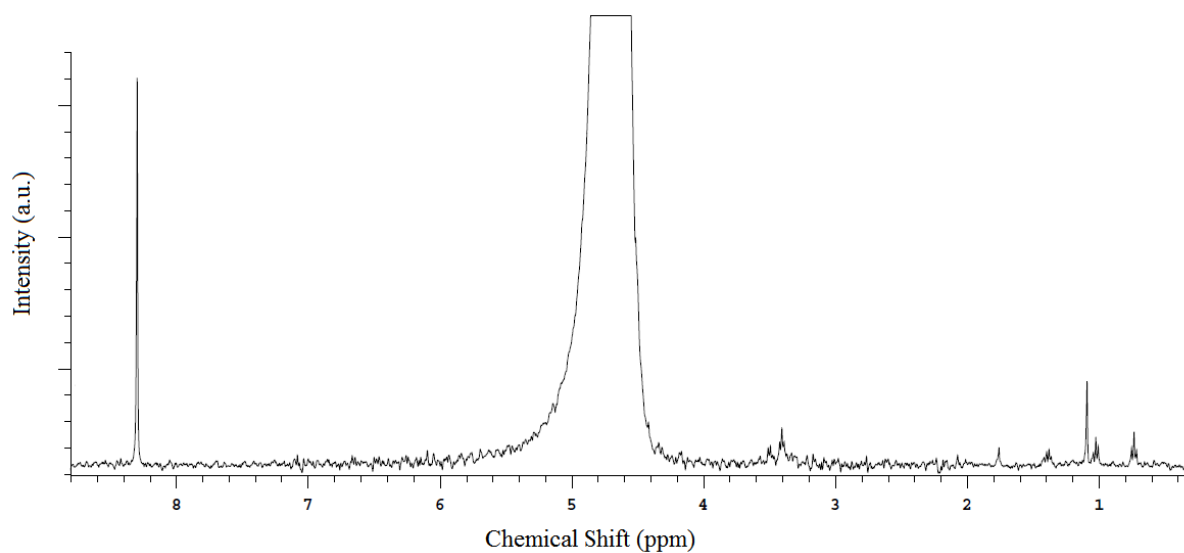
Figure S2.2.12 ^{1}H NMR spectra of electrolytes after reduction of CO$_2$ on 7.3-μm-length Cu nanowires in CO$_2$-saturated 0.1 M KHCO$_3$ electrolytes.

Faradaic efficiency for products

Table S2.2.3 Faradaic efficiency for C_2H_4, C_2H_6, CO, HCOOH, Ethanol, n-Propanol and H_2 on Cu nanowire arrays with different lengths at -1.1 V vs. RHE in CO_2-saturated 0.1 M $KHCO_3$ electrolytes (0 μm nanowire represents Cu foil).

Average Length	Faradaic efficiency (%)						
(μm)	C_2H_4	C_2H_6	CO	HCOOH	Ethanol	n-Propanol	H_2
0 (flat Cu)	2		6	12.7			83
2.0	5		9.9	18.4			63.7
2.4	10.4		10	19		5.8	52
3	14.2		10	20.7		7.8	48.4
5	14.4		7	23.5		8	46
7.3	16.6	2	8.5	15.5	5	9	44.3
8.1	17.4	2.4	7.6	17.5	3.8	7.8	44.2

References

[1]   Y. Hori, in *Electrochemical CO2 Reduction on Metal Electrodes* (Ed.: E. Vayenas, C. G., White, R. E., Gamboa-Aldeco, M. E.), Springer New York, **2008**, p. Vol. 42, p 89.

[2]   Y. Hori, A. Murata, R. Takahashi, *Journal of the Chemical Society, Faraday Transactions 1: Physical Chemistry in Condensed Phases* **1989**, *85*, 2309.

[3]   M. Ma, K. Djanashvili, W. A. Smith, *Phys. Chem. Chem. Phys.* **2015**, *17*, 20861–20867.

3. Selective and Efficient Reduction of CO$_2$ to CO on Oxide-Derived Nanostructured Ag Electrocatalysts

In this work, the selective electrocatalytic reduction of CO$_2$ to CO on oxide-derived Ag electrocatalysts is presented. By a simple synthesis technique, the overall high faradaic efficiency for CO production on the oxide-derived Ag was shifted by >400 mV towards a lower overpotential compared to that of untreated Ag. Notably, the Ag resulting from Ag oxide is capable of electrochemically reducing CO$_2$ to CO with approximately 80% catalytic selectivity at a moderate overpotential of 0.49 V, which is much higher than that (~4%) of untreated Ag at identical conditions. Electrokinetic studies show that the improved catalytic activity is ascribed to the enhanced stabilization of COOH$^\bullet$ intermediate. Furthermore, a highly nanostructured Ag is likely able to create a high local pH near the catalyst surface, which may also facilitate the catalytic activity for the reduction of CO$_2$ with suppressed H$_2$ evolution.

Graphical Abstract
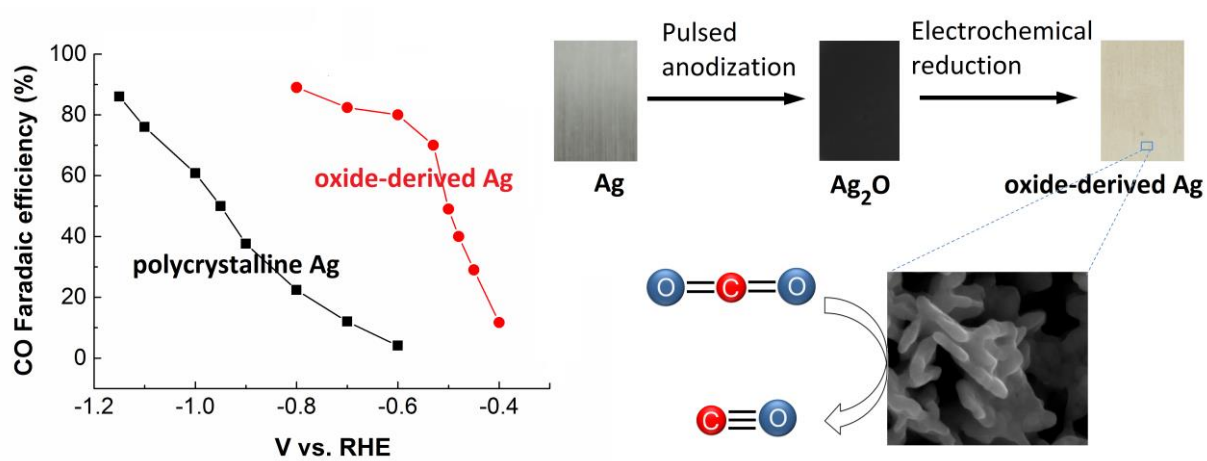
3.1 Introduction

The electrochemical conversion of CO_2 into carbon-based fuels is an attractive strategy for utilizing CO_2 captured at large emission sources.[1–5] In order to close the anthropogenic carbon cycle, the electrocatalytic reduction of CO_2 to fuels should be powered by a renewable electricity source.[6] For achieving this goal, the essential step is to develop a cheap, stable, and efficient catalyst with high selectivity for a desired product. Over the past few decades, several catalyst materials with the capability of reducing CO_2 electrochemically in CO_2 saturated-aqueous solutions have been identified.[3,7–18] It has been demonstrated that polycrystalline Au is capable of reducing CO_2 to CO with a high faradaic efficiency (FE) of ~ 87% at -0.74 versus the reversible hydrogen electrode (RHE).[5] While Au is currently the most efficient electrocatalytic surface for CO_2 reduction to CO, the low abundance and high cost of Au may prevent its large-scale applications. To find a cost-effective and stable catalyst with high selectivity and efficiency remains a challenge for achieving practical utilization of CO_2 reduction to CO.

Metallic Ag has attracted considerable attention due to its significantly lower cost compared to Au and high selectivity for CO_2 to CO conversion.[7,11] However, the high overpotential (> 0.9 V) on Ag catalysts is required for driving the electrocatalytic reduction of CO_2 efficiently and selectively with suppressed H_2O reduction.[5] The large overpotential required for the reduction of CO_2 is attributed to the hindrance for the initial electron transfer to a CO_2 molecule.[2,19–21] Lu *et al.*[19] reported that a nanoporous Ag catalyst with a fast initial electron transfer prepared by the de-alloying of an Ag-Al prescursor is capable of reducing CO_2 electrochemically to CO efficiently and selectively at reduced overpotential. Recently, Kanan *et al.*[21,22] discovered that oxide-derived Cu and Au nanoparticle films exhibit dramatically improved selectivity for reduction CO_2 to CO at low overpotential and high resistance to catalytic deactivation compared to polycrystalline metals.

This study is the first exploration of the catalytic activity of the electrochemical reduction of CO_2 on oxide-derived nanostructured Ag catalysts (OD-Ag). Here we demonstrate that a nanostructured Ag electrode resulting from silver oxide is capable of electrochemically reducing CO_2 to CO with high selectivity at much lower overpotential compared to that of the polycrystalline Ag, and the increased catalytic activity is linked to the improved stabilization of the COOH$^\bullet$ intermediate.

3.2 Experimental section

The thermal oxidation of Ag foils is prohibited because the decomposition of silver oxide becomes significant at temperatures above 200 °C.[23] Here, we used a simple and scalable electrochemical method for oxidizing Ag electrodes. Potential anodization in alkaline solutions was an effective and simple method for the formation of Ag oxide on Ag electrodes.[24–28] Here, an electrode made of a polycrystalline Ag foil was immersed in 0.2 M NaOH solutions in a two-compartment cell with a Pt counter electrode and an Ag/AgCl reference electrode (cyclic voltammetry of Ag in 0.2 M NaOH is shown in Figure S3.1). The two-compartment cell was separated by a Nafion-115 proton exchange membrane to avoid Pt deposition on Ag electrodes during the electrochemical synthesis. Symmetric 50 Hz square-wave pulsed potential was applied on Ag electrodes to synthesize Ag oxide layers. We found that the fabricated Ag oxide layers exhibit a porous structure, as shown in Figure S3.2. The resulting Ag oxide electrodes were directly utilized in the electrochemical reduction of CO_2, and were electrochemically reduced to metallic Ag in the early stage of electrolysis.

3.3 Results and discussion

Figure 3.1a and b show scanning electron microscope (SEM) images of electrodes resulting from Ag oxide after the electrocatalytic reduction of CO_2 in CO_2-saturated electrolytes. The SEM images indicate that a porous-like nanostructured Ag surface was formed as a result of the reduction of Ag oxide after electrolysis. The X-ray diffraction (XRD) pattern in Figure 3.1 (c) confirms the presence of Ag_2O on Ag foil synthesized by anodization in alkaline solutions. After CO_2 reduction electrolysis, XRD pattern shows only Ag peaks with no more indication of any remaining Ag oxide. In addition, the Ag foil fabricated by anodization turned a black color (Figure S3.3), which is also indicative of the formation of Ag oxide, and the sample had no remaining black color after CO_2 reduction electrolysis.

To further confirm the composition of the samples before and after electrolysis, X-ray photoelectron spectroscopy (XPS) measurements were performed. The Ag $3d_{5/2}$ peak at 368.2 eV was observed for polycrystalline Ag in Figure 3.1d. For the synthesized Ag oxide, the Ag $3d_{5/2}$ peak shifted to the binding energy of 367.7 eV, which corresponds to the Ag_2O formation according to the Ag $3d_{5/2}$ peak analysis for Ag and Ag oxide in previous work.[29] After electrolysis, the Ag $3d_{5/2}$ peak shifted back to 368.2 eV, implying the surface was

metallic Ag without any Ag oxide.[29] The Ag 3d XPS spectrum analysis is consistent with the results of the XRD patterns, indicating the electroreduction of Ag_2O to metallic Ag was complete within the detection limit of these characterization techniques.
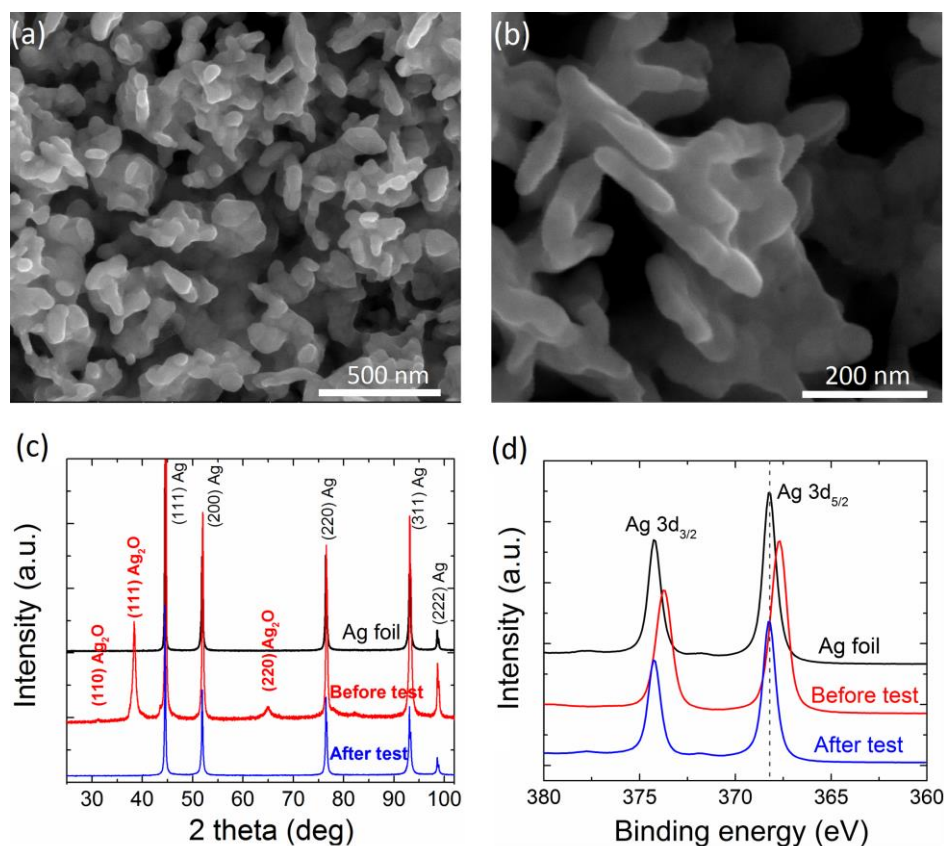
Figure 3.1 (a) and (b) SEM images of oxide-derived Ag. (c) XRD patterns and (d) XPS spectrum of the polycrystalline Ag electrode (black line) and Ag oxide electrode before (red line) and after (blue line) CO_2 reduction electrolysis, respectively.

The electrocatalytic reduction of CO_2 on OD-Ag and polycrystalline Ag were performed in CO_2-saturated 0.1 M $KHCO_3$ (99.95%) electrolytes (pH = 6.83) at ambient temperature and pressure. In the initial period of electrolysis, OD-Ag electrodes were directly formed in situ by the electroreduction of the Ag oxide film formed on the Ag electrode. CO_2 reduction electrolysis experiments were performed in an electrochemical cell consisting of working and counter electrode compartments, separated by a Nafion-115 proton exchange membrane to prevent the oxidation of CO_2 reduction products. The cathodic compartment was continuously purged with CO_2 at a constant flow rate and vented directly into the gas-sampling loop of a gas chromatograph (GC) for the periodic quantification of the gas-phase products. Liquid

products formed in the CO_2 reduction were detected by ^{1}H nuclear magnetic resonance (NMR) after completion of the electrolysis experiments.

The comparison of the CO_2 reduction activity of untreated polycrystalline Ag and OD-Ag is presented in Figure 3.2. The OD-Ag exhibited a high initial current density (j_{tot}) (Figure S3.4), which stems from the reduction of the Ag oxide layer in the initial period of electrolysis. Subsequently, the OD-Ag exhibited a j_{tot} of 1.15 mA/cm^2 with CO faradaic efficiency of 89% at -0.8 V vs. RHE, as shown in Figure 3.2a. At a less negative potential of -0.7 V vs. RHE, a decreased FE of 82.4% for CO formation was observed (Figure 3.2b). Notably, the FE of 80% for CO production was achieved at -0.6 V vs. RHE (Figure 3.2c), corresponding to a modest overpotential (η_{CO}) of 0.49 V relative to the CO_2/CO equilibrium potential of -0.11 V vs. RHE. In contrast, the polycrystalline Ag electrodes experienced low j_{tot}, accompanying with very low FE for CO formation (22.4%, 12% and 4.1% at -0.8 V, -0.7 V and -0.6 V vs. RHE, respectively).
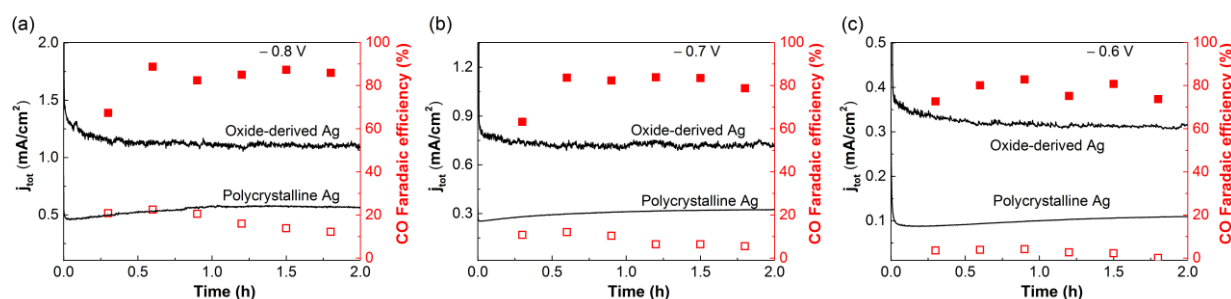
Figure 3.2 CO_2 reduction performance of untreated Ag and oxide-derived Ag. The total current density (left axis) and the CO faradaic efficiency (right axis) on untreated Ag and oxide-derived Ag (■ and □ represent CO faradaic efficiency on oxide-derived Ag and untreated Ag respectively) at (a) -0.8 V and (b) -0.7 V, and (c) -0.6 V vs. RHE in CO_2-saturated 0.1 M KHCO$_3$ electrolytes.

To better understand the catalytic activity for CO_2 reduction, the FE for the major products of CO_2 reduction was plotted at various potentials for the polycrystalline Ag and the OD-Ag (Figure 3.3). As noted in Figure 3.3a, the FE for the electrochemical reduction of CO_2 to CO on both the polycrystalline Ag and the OD-Ag gradually increased with enhancing overpotentials. The increase of the FE for CO corresponds to a decrease in the related FE for H_2 production (Figure 3.3b). In addition, a small amount of formate was only detected at high overpotentials (Figure S3.5). Interestingly, Figure 3.3a shows that the overall FE for CO on

the OD-Ag was shifted by > 400 mV toward the positive potential compared to that of untreated Ag (at the range of FE for CO > 30%). In addition, the current density for CO production as a function of potentials in figure 3.3c implies the onset potential for CO_2 reduction on OD-Ag was -0.4 V vs. RHE (η_{CO} = 0.29 V), which is a positive shift by ~ 200 mV compared to that (-0.6V vs. RHE) of polycrystalline Ag. More importantly, for driving the electrocatalytic reduction of CO_2 to CO with a high FE of 80%, a potential of -0.6 V vs. RHE was required on OD-Ag, which is significantly reduced by 500 mV compared to that of untreated Ag (-1.1 V vs. RHE). These results indicate that OD-Ag acts as an efficient catalyst for the electrocatalytic reduction of CO_2 to CO with significantly suppressed H_2 evolution at decreased overpotentials.
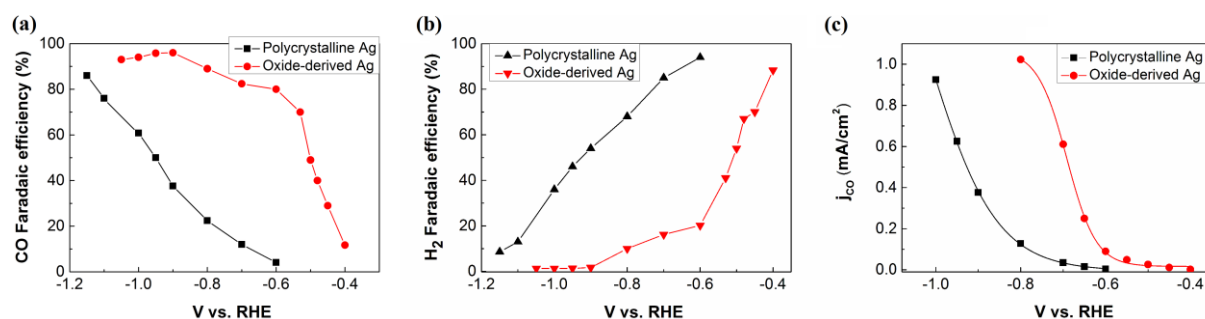
Figure 3.3 Comparison of the electrocatalytic activity of polycrystalline Ag and oxide-derived Ag. Faradaic efficiency for CO (a) and H_2 (b) on polycrystalline Ag and oxide-derived Ag at various potentials in CO_2-saturated 0.1 M $KHCO_3$ (pH= 6.8). (c) Current density for CO at various potentials.

To gain insight into the electrokinetic mechanism of CO_2 reduction on both catalysts, a Tafel plot analysis was performed. Here, Tafel plots of the OD-Ag and the polycrystalline Ag (overpotential versus log of the partial current density for CO production) are shown in Figure 3.4. Hori has proposed that a two-electron transfer is involved in the electrochemical reduction of CO_2 to CO (Scheme 1).[11,30] In addition, most of the computational studies on reaction paths for CO_2 reduction are based on the computational hydrogen electrode (CHE) model, which is assumed that a proton-coupled electron transfer (PCET) takes place at every reaction step.[31–35] Thus, a COOH$^\bullet$ is assumed to be formed via a PCET as the first CO_2 activation step in density funcational theory (DFT) simulations.[31,33–35] However, in some experimental work, it is believed that the adsorbed $CO_2^{\bullet-}$ intermediate is formed on the active sites of metal surface via a one-electron transfer to a CO_2 molecule, and then the COOH$^\bullet$

intermediate is produced after accepting one proton.[19–22,36] Furthermore, it was reported that the first proton donation is from HCO_3^-.[19,21,35] Subsequently, the COOH• intermediate on the surface takes another electron and proton to form a CO and a H_2O molecule. It has been demonstrated that the initial electron transfer for CO_2 activation is the rate determining step (RDS) for the overall process because the first electron transfer requires a much more negative potential compared to the following steps.[2,19–21]
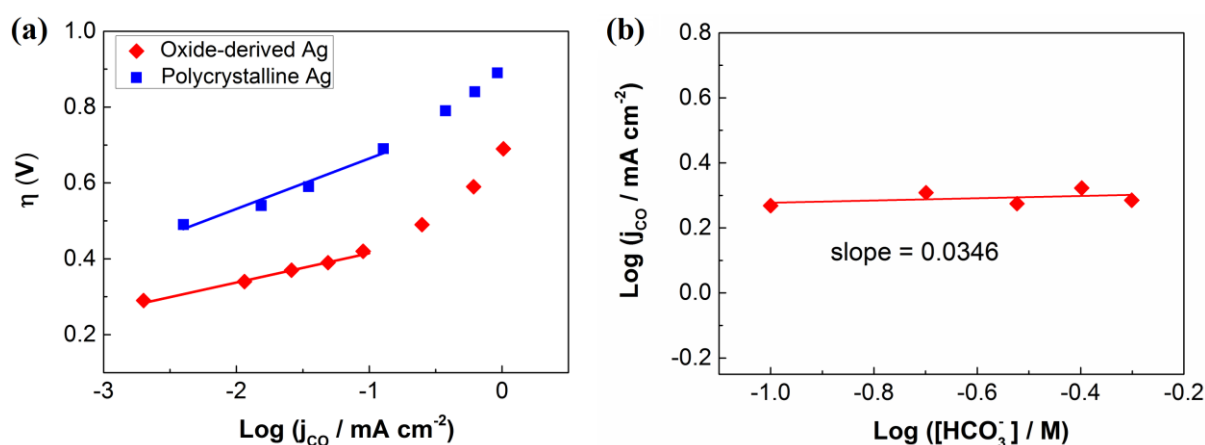
Figure 3.4 (a)Tafel plots of the CO partial current density for polycrystalline Ag and oxide-derived Ag. (b)Bicarbonate concentration at constant potential for oxide-derived Ag.
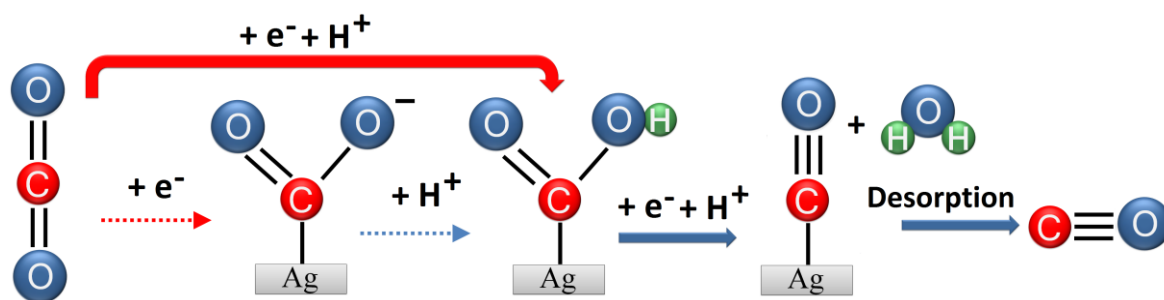
Scheme 1. Proposed reaction paths for electrocatalytic reduction of CO_2 to CO.

A Tafel slope of 133 mV/dec for polycrystalline Ag shown in Figure 3.4a corresponds to a transfer coefficient of 0.44 (Equation S3.2). This slope and the transfer coefficient are consistent with the fact that the rate determining step is the initial electron transfer to CO_2.[11,19] In contrast, OD-Ag exhibited a low Tafel slope of 77 mV/dec at low overpotentials, which indicates a fast initial electron transfer to a CO_2 molecule according to previous

studies[7,19,21,22]. Subsequently, we found a dramatic increases of the Tafel slope for OD-Ag at relatively high overpotentials, indicating the CO_2 electroreduction may reach a mass transport limitation on the porous-like nanostructured Ag.[35] Thus, while the mass transport in a nanostructured Ag catalyst is likely slower than an untreated Ag (flat surface) at relatively high overpotentials, the OD-Ag can offer better stabilization for the $COOH^\bullet$ intermediate than that of untreated Ag, thus decreasing the overpotential needed to drive CO_2 reduction to CO.

To further investigate the electrokinetics of CO_2 reduction on OD-Ag, electrolysis was performed at the HCO_3^- concentrations from 0.5 to 0.1 M. A plot of $\log(j_{CO})$ vs $\log([HCO_3^-])$ in Figure 3.4b shows a zero-order dependence of HCO_3^- concentrations on CO_2 reduction activity, indicating that the donation of a proton from HCO_3^- is not a rate-determining step for CO_2 reduction.[19]

It was reported that the surface of nanostructured Ag catalysts can provide the low-coordinated surface Ag sites, which plays a significant role for stabilizing the $COOH^\bullet$ intermediate through reducing the activation energy barrier of the initial electron transfer.[35] In addition, Kanan et al. proposed a grain boundary effect for OD-Cu[37] and OD-Au[38]. Here we propose a local pH effect to offer a new insight into the correlation of nanostructured Ag catalysts with the catalytic activity for CO_2 reduction. The pH rises locally at the electrode/electrolyte interface because of releasing OH^- in the cathodic reactions (equation S (3.4-3.5)).[39] Thus, the pH close to the electrode (local pH) is higher than the bulk pH. To understand the local pH effect, CO_2 reduction was performed on flat Ag and OD-Ag in 0.1 M K_2HPO_4 and 0.1 M $KHCO_3$, respectively. The FE for CO on flat Ag was significantly reduced (Figure 3.5a) with dramatically enhanced FE for H_2 (Figure 3.5c) in CO_2-saturated 0.1 M K_2HPO_4, which is consistent with the Hori's work on flat Cu (FE for H_2 is 72.4% and 10.9% in 0.1 M K_2HPO_4 and 0.1 M $KHCO_3$, respectively)[11]. This observation is due to the fact that the buffer action of CO_2-saturated 0.1 M K_2HPO_4 can easily neutralize OH^- generated at the electrode surface, keeping local pH at relatively low value. The low pH value at the electrode/electrolyte interface favors H_2 evolution.[11] To further improve the local pH effect, CO_2 reduction was also measured on flat Ag in 0.1 M $KClO_4$. $KClO_4$ does not have buffer ability, which results in a relatively high local pH at the electrode/electrolytes interface. We found that the FE for CO in CO_2-saturated 0.1 M $KClO_4$ was obviously higher than that of CO_2-saturated 0.1 M $KHCO_3$ (Figure 3.5a). These observations (the FE for CO on flat Ag: $KClO_4 > KHCO_3 > K_2HPO_4$) imply that the local pH may play an important role in CO_2 reduction.
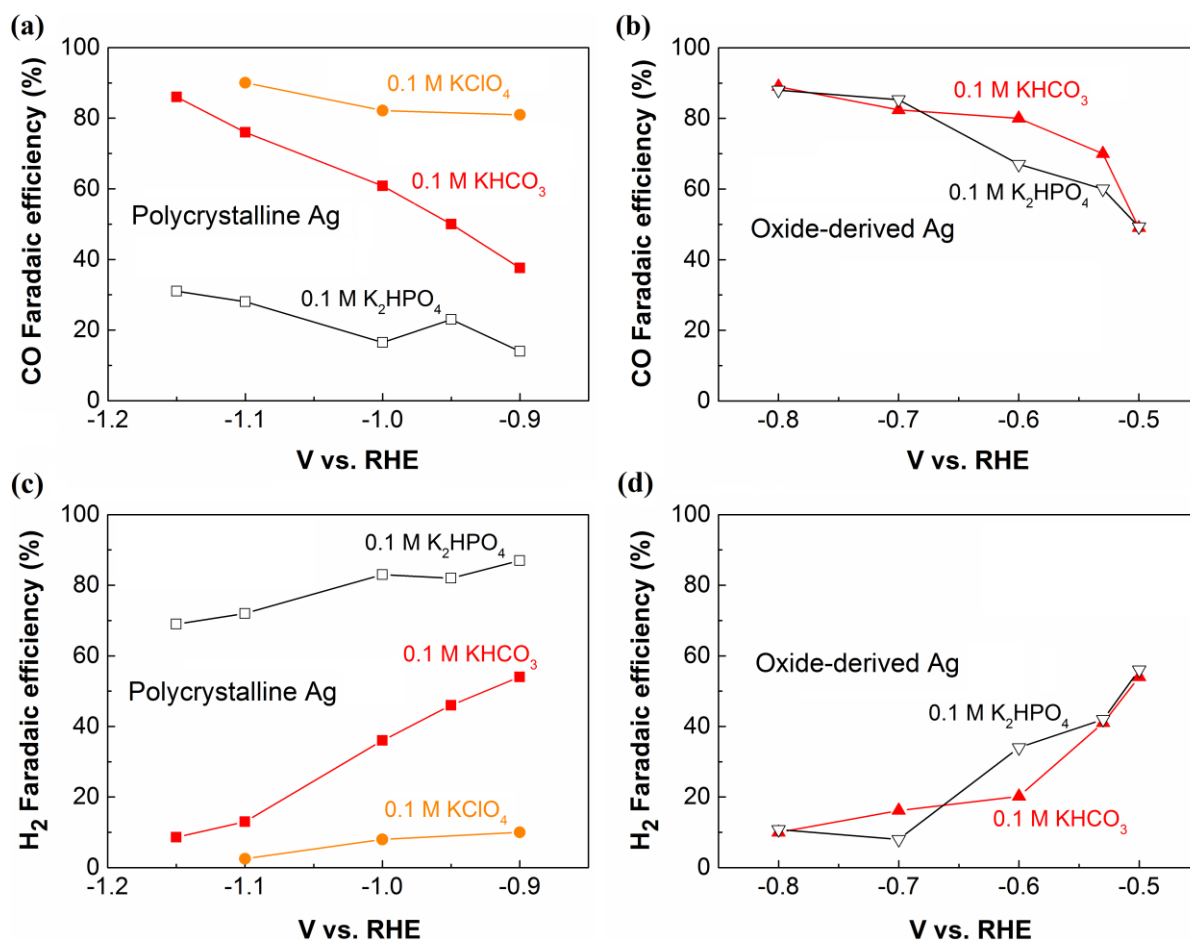
Figure 3.5. Faradaic efficiency for CO and H_2 on polycrystalline Ag (a) (c) and oxide-derived Ag (b) (d) at various potentials in CO_2-saturated 0.1 M K_2HPO_4 and CO_2-saturated 0.1 M $KHCO_3$, respectively. CO_2 reduction on flat Ag was also performed in CO_2-saturated 0.1 M $KClO_4$.

In contrast, we found that FE for CO on OD-Ag was almost equal in the two different electrolytes (Figure 3.5b) at various potentials. This observation may be partly attributed to that the limitation of the diffusion process in nanoporous Ag catalysts (Figure 3.1a and b) causes a decreased amount of the neutralization reaction for OH^- generated near the catalyst surface, resulting in a high local pH in 0.1 M K_2HPO_4. In addition, H_2 evolution is not favorable at the high pH value. Thus, the high local pH created in nanoporous Ag may contribute to the suppressed H_2 evolution (Figure 3.5d) with preferred CO_2 reduction (Figure 3.5b).

3.4 Conclusions

In summary, nanostructured Ag catalysts prepared by electrochemically reducing Ag_2O exhibited an enhanced catalytic activity for the reduction of CO_2, and the high selectivity for CO was shifted by > 400 mV to a lower overpotential than that of untreated polycrystalline Ag. At a moderate overpotential of 0.49 V, the oxide-derived nanostructured Ag was able to reduce CO_2 to CO with ~80% faradaic efficiency, which is dramatically higher compared to that (~4%) of untreated polycrystalline Ag at identical conditions. The dramatically improved catalytic activity and selectivity for CO_2 reduction to CO is likely correlated with the nanostructured surface, resulting in highly active sites for stabilizing $COOH^{\bullet}$ intermediate. In addition, a high local pH generated within the porous-like nanostructured Ag catalysts may also play a role in the improved CO_2 reduction along with suppressed H_2 evolution. This study shows that a selective and cost-effective oxide-derived Ag catalyst can efficiently and selectively reduce CO_2 to CO. While the catalytic activity of this oxide-derived Ag catalyst is not as high as the recent oxide-derived Au, its cost is significantly lower, and thus this catalyst and synthetic approach may provide a more practical platform for large-scale CO_2 electroreduction.

References

[1] D. T. Whipple, P. J. A. Kenis, *J. Phys. Chem. Lett.* **2010**, *1*, 3451–3458.

[2] Y. Chen, M. W. Kanan, *J. Am. Chem. Soc.* **2012**, *134*, 1986–1989.

[3] J. Qiao, Y. Liu, F. Hong, J. Zhang, *J. Chem. Soc. Rev.* **2014**, *43*, 631–675.

[4] N. Kornienko, Y. Zhao, C. S. Kley, C. Zhu, D. Kim, S. Lin, C. J. Chang, O. M. Yaghi, P. Yang, *J. Am. Chem. Soc.* **2015**, *137*, 14129–14135.

[5] K. P. Kuhl, T. Hatsukade, E. R. Cave, D. N. Abram, J. Kibsgaard, T. F. Jaramillo, *J. Am. Chem. Soc.* **2014**, *136*, 14107–14113.

[6] M. Ma, K. Djanashvili, W. A. Smith, *Phys. Chem. Chem. Phys.* **2015**, *17*, 20861–20867.

[7] M. Gattrell, N. Gupta, A. Co, *J. Electroanal. Chem.* **2006**, *594*, 1–19.

[8] K. P. Kuhl, E. R. Cave, D. N. Abram, T. F. Jaramillo, *Energy Environ. Sci.* **2012**, *5*, 7050–7059.

[9] K. Manthiram, B. J. Beberwyck, A. P. Alivisatos, *J. Am. Chem. Soc.* **2014**, *136*, 13319–13325.

[10] Y. Hori, R. Takahashi, Y. Yoshinami, A. Murata, *J. Phys. Chem. B* **1997**, *101*, 7075–7081.

[11] Y. Hori in *Modern Aspects of Electrochemistry, Vol. 42* (Eds: C. G. Vayenas, R. E. White, M. E. Gamboa-Aldeco), Springer, New York, **2008**, pp. 89 – 189.

[12] S. Zhang, P. Kang, S. Ubnoske, M. K. Brennaman, N. Song, R. L. House, J. T. Glass, T. J. Meyer, *J. Am. Chem. Soc.* **2014**, *136*, 7845–7848.

[13] J. Tamura, A. Ono, Y. Sugano, C. Huang, H. Nishizawa, S. Mikoshiba, Phys. Chem. Chem. Phys. **2015**, 17, 26072–26078.

[14] D. A. Torelli, S. A. Francis, J. C. Crompton, A. Javier, J. R. Thompson, B. S. Brunschwig, M. P. Soriaga, N. S. Lewis, *ACS Catal.* **2016**, 6, 2100–2104.

[15] M. Ma, K. Djanashvili, W. A. Smith, *Angew. Chem. Int. Ed.* **2016**, *55*, 6680–6684.

[16] S. Rasul, D. H. Anjum, A. Jedidi, Y. Minenkov, L. Cavallo, K. Takanabe, *Angew. Chem. Int. Ed.* **2015**, 54, 2146–2150.

[17] A. Loiudice, P. Lobaccaro, E. A. Kamali, T. Thao, B. H. Huang, J. W. Ager, R. Buonsanti, *Angew. Chem. Int. Ed.* **2016**, 94720, 5789–5792.

[18] R. Kas, K. K. Hummadi, R. Kortlever, P. de Wit, A. Milbrat, M. W. J. Luiten-Olieman, N. E. Benes, M. T. M. Koper, G. Mul, *Nat. Commun.* **2016**, 7, 10748.

[19] Q. Lu, J. Rosen, Y. Zhou, G. S. Hutchings, Y. C. Kimmel, J. G. Chen, F. Jiao, *Nat. Commun.* **2014**, *5*, 3242.

[20] Q. Lu, J. Rosen, F. Jiao, *ChemCatChem* **2015**, *7*, 38–47.

[21] Y. Chen, C. W. Li, M. W. Kanan, *J. Am. Chem. Soc.* **2012**, *134*, 19969–19972.

[22] C. W. Li, M. W. Kanan, *J. Am. Chem. Soc.* **2012**, *134*, 7231–7234.

[23] G. B. Hoflund, Z. F. Hazos, *Phys. Rev. B* **2000**, *62*, 11126–11133.

[24] T. P. Dirkse, *Electrochim. Acta.* **1990**, *35*, 1445–1449.

[25] V. Maurice, L. Klein, H.-H. Strehblow, P. Marcus, *J. Phys. Chem. C.* **2007**, *111*, 16351–16361.

[26] J. M. M. Droog, F. Huisman, *Journal of Electroanalytical Chemistry and Interfacial Electrochemistry* **1980**, *115*, 211–224.

[27] J. Gomez Becerra, R. C. Salvarezza, A. J. Arvia, *Electrochim. Acta.* **1988**, *33*, 1431–1437.

[28] J. Ambrose, R. G. Barradas, *Electrochim. Acta.* **1974**, *19*, 781–786.

[29] X.-Y. Gao, S.-Y. Wang, J. Li, Y.-X. Zheng, R.-J. Zhang, P. Zhou, Y.-M. Yang, L.-Y. Chen, *Thin Solid Films* **2004**, *455-456*, 438–442.

[30] Y. Hori, H. Wakebe, T. Tsukamoto, O. Koga, *Electrochim. Acta.* **1994**, *39*, 1833–1839.

[31] R. Kortlever, J. Shen, K. J. P. Schouten, F. Calle-Vallejo, M. T. M. Koper, *J. Phys. Chem. Lett.* **2015**, 6, 4073–4082.

[32] F. Calle-Vallejo, M. T. M. Koper, *Angew. Chem. Int. Ed.* **2013**, 125, 7423–7426.

[33] A. a. Peterson, F. Abild-Pedersen, F. Studt, J. Rossmeisl, J. K. Nørskov, *Energy Environ. Sci.* **2010**, 3, 1311.

[34] H. A. Hansen, J. B. Varley, A. A. Peterson, J. K. Nørskov, *J. Phys. Chem. Lett.* **2013**, *4*, 388–392.

[35] J. Rosen, G. S. Hutchings, Q. Lu, S. Rivera, Y. Zhou, D. G. Vlachos, F. Jiao, *ACS Catal.* **2015**, *5*, 4293–4299.

[36] C. H. Lee, M. W. Kanan, *ACS Catal.* **2015**, 5, 465–469.

[37] C. W. Li, J. Ciston, M. W. Kanan, *Nature* **2014**, *508*, 504–507.

[38] X. Feng, K. Jiang, S. Fan, M. W. Kanan, *J. Am. Chem. Soc.* **2015**, *137*, 4606–4609.

[39] Y. Hori, A. Murata, R. Takahashi, *J. Chem. Soc., Farad. Trans. 1* **1989**, *85*, 2309.

Supplementary information for Chapter 3

Materials

NaOH (99.99%), KHCO$_3$ ($\geq$99.95%), K$_2$HPO$_4$ ($\geq$99.999%), KClO$_4$ ($\geq$99.99%) and KCl ($\geq$99%) were purchased from Sigma Aldrich. All chemicals were used in this study without further purification. Silver foil (99.998%, 0.25 mm thick, hard) were purchased from Alfa Aesar. The silver foils were ultrasonically cleaned in acetone and ethanol. The cleaned silver foils were dried with nitrogen.

Fabrication of Silver Oxide

Figure S3.1 is a typical cyclic voltammetry (CV) for a silver electrode in 0.2 M NaOH. The oxidation peaks (a) and (b) in the anodic sweep are related to the formation of Ag oxide. The cathodic peaks (c) and (d) represent the reduction of AgO and Ag$_2$O, respectively.[1,2] A piece of Ag foil was immersed in 0.2 M NaOH solutions in a two-compartment cell (the two-compartment cell was separated by a Nafion-115 proton exchange membrane) with a Pt count electrode and an Ag/AgCl reference electrode (XR300, saturated KCl + AgCl solution (KS120), Radiometer Analytical). A symmetric 50 Hz square-wave pulse between 1 V and 2.2 V (vs. RHE) were applied for 5 hours (900000 cycles).
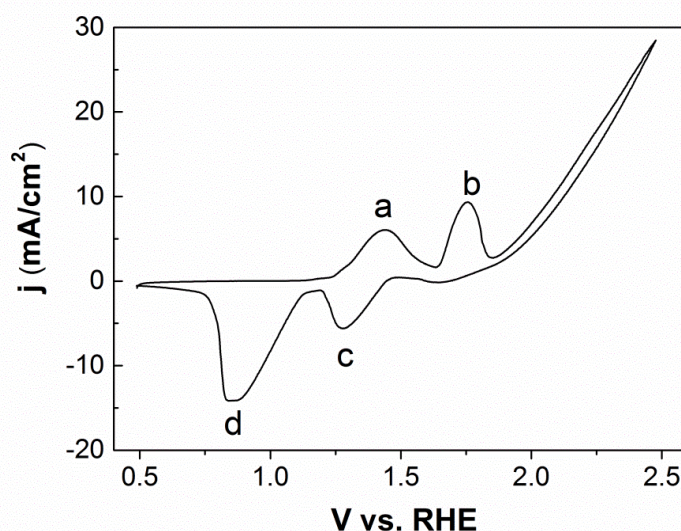
Figure S3.1 Cyclic voltammetry of polycrystalline Ag foils in 0.2 M NaOH electrolytes at ambient temperature and pressure (scan rate is 0.02 V/s).
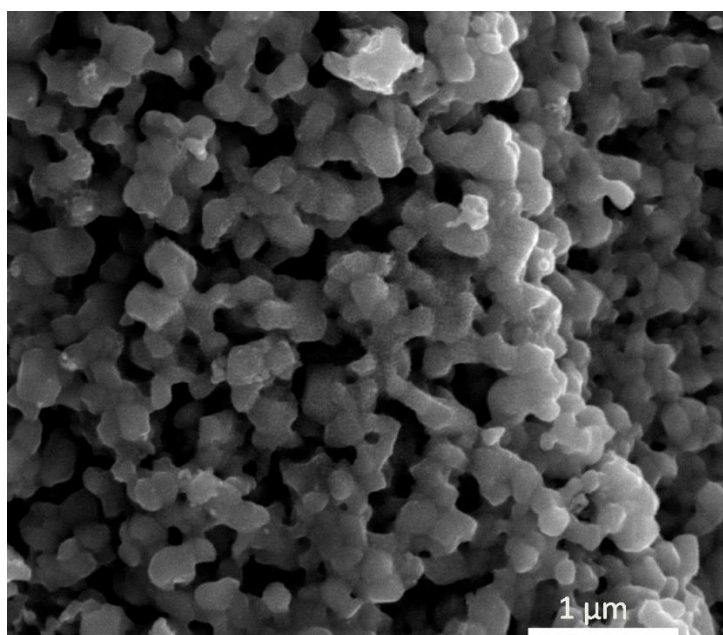
Figure S3.2 SEM images of Ag oxide on Ag foil synthesized by anodization in 0.2 M NaOH solutions.
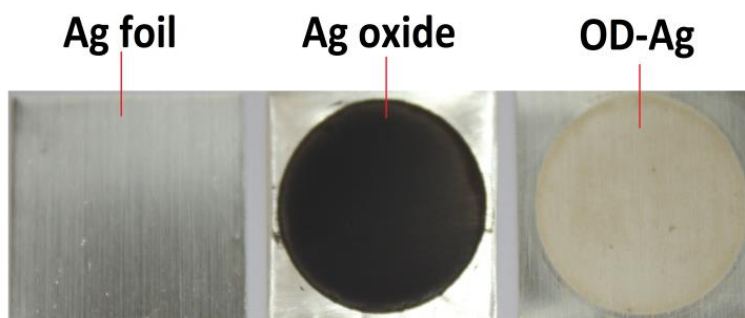
Figure S3.3 Digital images of the polycrystalline Ag foil (left image), the Ag oxide film synthesized on Ag foil before (middle image) and after (right image) CO_2 reduction electrolysis, respectively.
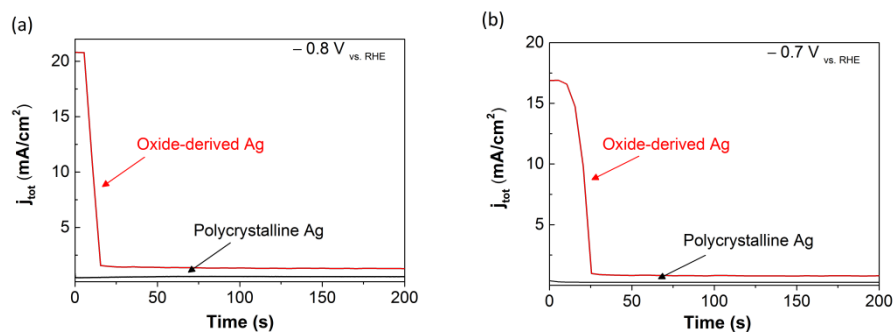
Figure S3.4 Current density as a function of time for the untreated Ag and the oxide-derived Ag at -0.8 and -0.7 V vs. RHE in CO_2-saturated 0.1 M $KHCO_3$ electrolytes.

.

Physical Characterization

The morphology and nanostructure of the samples were characterized by using scanning electron microscope (SEM, Philips/FEI XL 40 FEG). The X-ray diffraction (XRD) patterns of the samples were obtained by using a diffractometer (Bruker AXS GmbH-D8 Discover) with Cu-Kα radiation (λ = 1.5406 Å). X-ray photoelectron spectroscopy (XPS, Thermo Scientific™ K-Alpha™) was utilized to confirm the oxidation states of Ag in the samples before and after the electrolysis.

Liquid product measurement

NMR measurements were performed at Agilent MR400DD2 NMR spectrometer operating at 400 MHz. Samples were prepared by mixing 450 µL of the electrolyte solutions with 50 µL of D_2O containing a known concentration of internal reference t-BuOH. ^{1}H NMR spectra were acquired by applying a hard pulse solvent pre-saturation pulse sequence with 2 s saturation delay, 2 s relaxation delay, 2.5 s acquisition time, and spectral window of 6400 Hz. Typically, 8 scans were collected and the peak areas were integrated for calculating the concentration of the solutes by taking into account the difference in the number of protons in the reference compound with respect to the product.
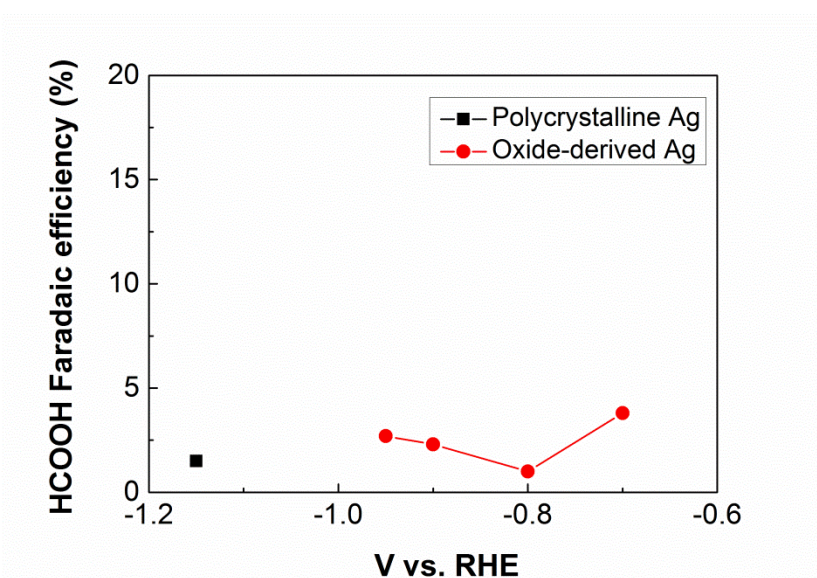
Figure S3.5 Faradaic efficiency for HCOOH at various potentials in CO_2-saturated 0.1 M $KHCO_3$ electrolytes at ambient temperature and pressure.

The Tafel slope is given by the partial derivative of the overpotential with respect to the log of the current as follow:

$$s = \left(\frac{\partial \eta}{\partial \log i_{co}} \right) \tag{S3.1}$$

where η is the overpotential for the reduction CO_2 to CO. i_{co} is CO current density. Here, a correlation between the Tafel slope and the transfer coefficient can be written as[3]:

$$\alpha \left(\frac{\partial \eta}{\partial \log i_{co}} \right) = \frac{2.3RT}{F} \tag{S3.2}$$

where F, R, T and α are Faraday constant, the gas constant, the absolute temperature and the transfer coefficient, respectively. Here, $\frac{2.3RT}{F}$ is ~59 mV/decade.

Partial current density

The partial current density for CO is calculated at a given potential as follow:

$$J_{CO} = f \times j_{tot} \tag{S3.3}$$

where J_{CO} and f are the partial current density and faradaic efficiency for CO production. j_{tot} is the total current during electrolysis. In our study the current density used for CO_2 reduction (without H_2 evolution) is considered to be equal to the partial current density for CO due to a very small amount of formate was only detected at high overpotentials (Figure S3.5).

Similar to the partial current density for CO, the partial current density for H_2 was plotted as a function of potentials on the polycrystalline Ag and oxide-derived Ag, as shown in the below figure S3.6. The polycrystalline Ag exhibited a dramatic increase in the partial current density for H_2 with enhancing overpotentials. In contrast, the oxide-derived Ag catalysts had an obviously suppressed partial current density for H_2 with increasing overpotentials. In addition, at the potential range from -0.4 → -0.8 V vs. RHE, the partial current density for CO on the OD-Ag catalyst increased to over 1 mA/cm^2 (Figure 3.3c), while the partial current density for H_2 production in the same range stayed below 0.11 mA/cm^2, indicating that as CO production is increased on this catalyst, H_2 production is sufficiently suppressed. All these observations further imply that OD-Ag acts as an efficient catalyst for the electrocatalytic reduction of CO_2 (Figure 3.3) with significantly suppressed H_2 evolution.
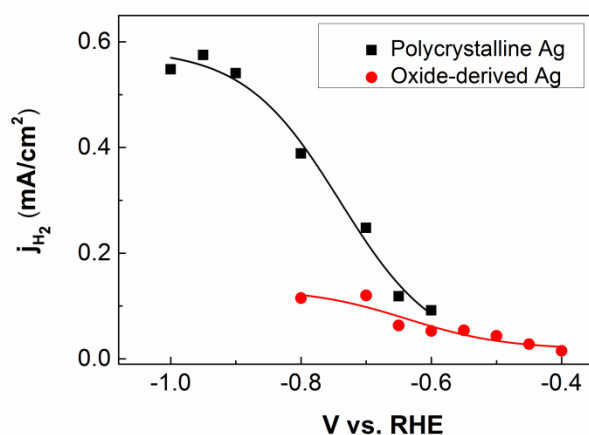
Figure S3.6 Current density for H_2 on polycrystalline Ag and oxide-derived Ag at various potentials in CO_2-saturated 0.1 M $KHCO_3$ (pH= 6.8).

$KHCO_3$ concentration effect

The electrochemical reduction of CO_2 to CO were performed at a constant applied potential (-0.6 V vs. RHE) at $KHCO_3$ concentrations ranging from 0.5 to 0.1 M. KCl was added to the low $KHCO_3$ concentration solutions to keep a total concentration of 0.5 M, maintaining ionic strength. Partial current density for CO formation as a function of the $\log([HCO_3^-])$ is presented in Figure S3.7.
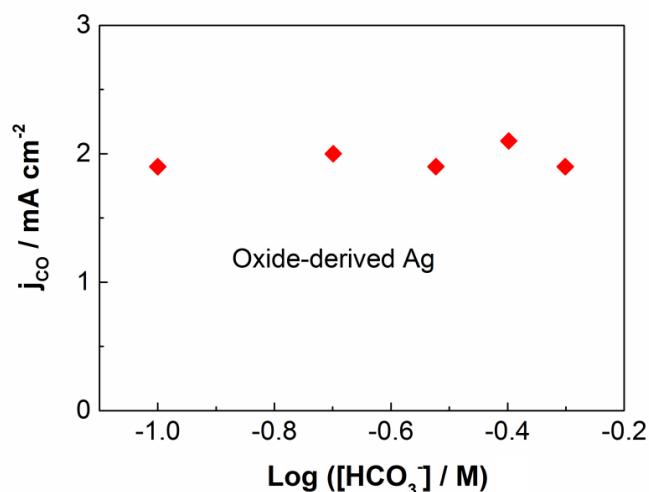
Figure S3.7 Partial current density for CO as a function of the $KHCO_3$ concentration at a constant potential.

Local pH

The electrochemical reduction of CO_2 to CO in CO_2-saturated aqueous solutions can be expressed by the following reaction:

$$CO_2 + H_2O + 2e^- \rightarrow CO + 2OH^- \qquad\qquad \text{(-0.11 V vs. RHE)} \qquad\qquad \text{(S3.4)}$$

H_2 evolution is a competing reaction with CO_2 reduction on Ag catalysts in CO_2-saturated electrolytes. Thus, H_2O could be electrochemically reduced to H_2 on Ag catalysts according to the below reaction:

$$2H_2O + 2e^- \rightarrow H_2 + 2OH^- \qquad\qquad \text{(0 V vs. RHE)} \qquad\qquad \text{(S3.5)}$$

OH^- ions are generated at the electrode in cathodic reactions according to the above reactions, resulting in the fact that the pH rises locally at the electrode/electrolyte interface.[4,5] Thus, the actual pH near the electrode is higher that of the bulk owing to the release of OH^- in the cathode electrode.[4,5]

Buffer action:

The pH of a phosphate buffer solution changes from the original fresh solution by bubbling with CO_2 due to the reaction as follow[5]:

$$HPO_4^{2-} + CO_2 + H_2O \rightarrow H_2PO_4^- + HCO_3^- \tag{S3.6}$$

The CO_2-saturated 0.1 M K_2HPO_4 (pH=6.5) is equal to a total electrolytes of 0.2 M (KH_2PO_4 + $KHCO_3$). After saturation and equilibrium with CO_2, 0.1 M K_2HPO_4 is converted into 0.1 M KH_2PO_4 and 0.1 M $KHCO_3$. Thus, the buffer ability in CO_2-saturated 0.1 M K_2HPO_4 (pH=6.5) is better than CO_2-saturated 0.1 M $KHCO_3$ (pH=6.8).

The pH also can be influenced by the below dissociation reactions:

$$H_2PO_4^- \leftrightarrow HPO_4^{2-} + H^+ \qquad pK_a = 7.2 \tag{S3.7}$$

$$HCO_3^- \leftrightarrow CO_3^{2-} + H^+ \qquad pK_a = 10.2 \tag{S3.8}$$

Where, pKa is the acid dissociation constant, which is a measure of the strength of an acid in solution.

Therefore, the buffer action (for neutralizing OH^-) of CO_2-saturated 0.1 M K_2HPO_4 (pH=6.5) is stronger than CO_2-saturated 0.1 M $KHCO_3$ (pH=6.8).
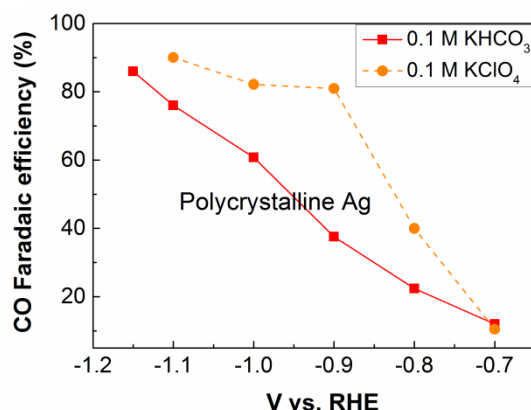
Figure S3.8 Faradaic efficiency for CO on polycrystalline Ag at various potentials in CO_2-saturated 0.1 M $KClO_4$ ($KClO_4$ does not have buffer ability) and CO_2-saturated 0.1 M $KHCO_3$, respectively.

References

[1]   T. P. Dirkse, *Electrochimica Acta* **1990**, *35*, 1445–1449.

[2]   J. M. M. Droog, F. Huisman, *Journal of Electroanalytical Chemistry and Interfacial Electrochemistry* **1980**, *115*, 211–224.

[3]   M. Ma, K. Djanashvili, W. A. Smith, *Phys. Chem. Chem. Phys.* **2015**, *17*, 20861–20867.

[4]   Y. Hori, A. Murata, R. Takahashi, *Journal of the Chemical Society, Faraday Transactions 1: Physical Chemistry in Condensed Phases* **1989**, *85*, 2309.

[5]   Y. Hori, in *Electrochemical CO2 Reduction on Metal Electrodes* (Ed.: E. Vayenas, C. G., White, R. E., Gamboa-Aldeco, M. E.), Springer New York, **2008**, p. Vol. 42, p 89.

4. Electronic Effects on the Electrochemical Reduction of CO_2 on Compositionally Variant Au-Pt Bimetallic Thin Films

The electrocatalytic reduction of CO_2 on Au-Pt bimetallic catalysts with different compositions was evaluated, offering a platform for uncovering the correlation between the catalytic activity and the composition of bimetallic electrocatalysts. The Au-Pt alloy films were synthesized by a magnetron sputtering co-deposition technique with tunable composition. It was found that the syngas ratio ($CO:H_2$) on the Au-Pt films is able to be tuned by systematically controlling the binary composition. This tunable catalytic selectivity is attributed to the variation of binding strength of COOH and CO intermediates, influenced by the surface electronic structure (d-band center energy) which is linked to the surface composition of the bimetallic films. Notably, a gradual shift of the d-band center away from the Fermi level was observed with increasing the Au content, which correspondingly reduces the binding strength of the COOH and CO intermediates, leading to the distinct catalytic activity for the reduction of CO_2 on the compositionally variant Au-Pt bimetallic films. In addition, the binding strength of the intermediates on the Au-Pt bimetallic films is correlated linearly with the variation of the binary composition, indicating that only the electronic effect in the bimetallic system is unable to break the scaling relation to significantly improve the catalytic activity and selectivity for CO_2 reduction to CO.

Ming Ma, Heine A. Hansen, Marco Valenti, Zegao Wang, Anping Cao, Mingdong Dong and Wilson A. Smith
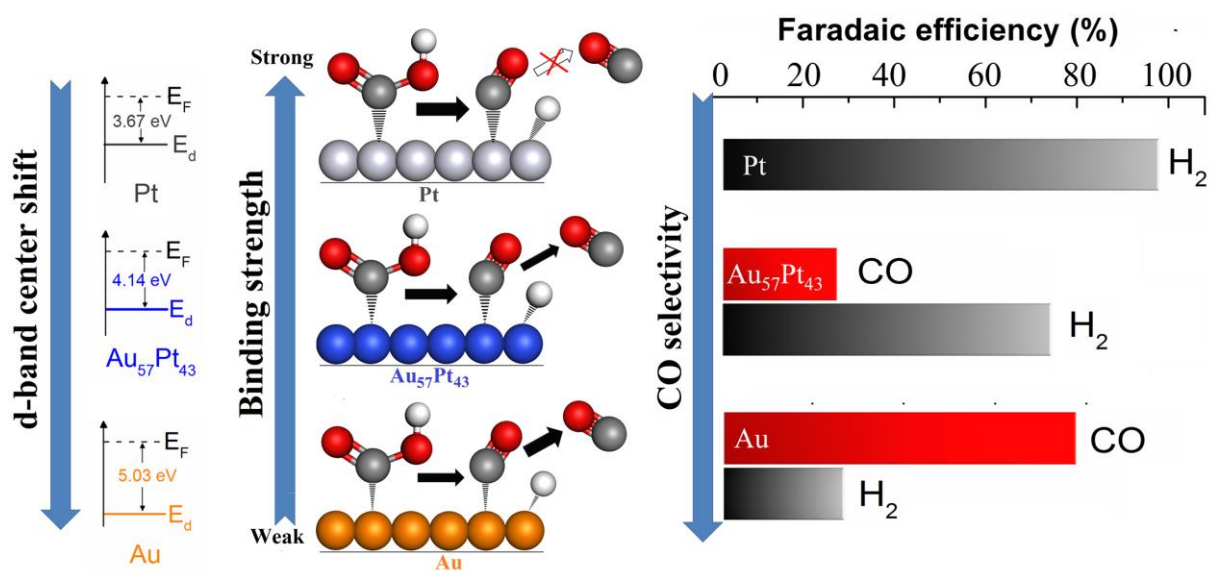
Graphical Abstract

4.1 Introduction

Converting CO_2 electrochemically into fuels and valuable chemicals has great potential for the utilization of captured CO_2.[1–6] For a sustainable production of fuels and value-added chemicals with zero carbon emission, renewable electricity sources can be used to power the electrocatalytic reduction of CO_2.[1,7] The main challenge for achieving this goal is to develop a cost-effective electrocatalyst which is capable of reducing CO_2 efficiently with controllable selectivity and long-term stability. Researchers have previously investigated various polycrystalline metallic materials for the electrochemical reduction of CO_2 in aqueous electrolyte.[2,3,8–11] While several polycrystalline metal catalysts have been identified with the capability to electrocatalytically reduce CO_2, the high overpotential required for driving selective CO_2 reduction with suppressed H_2 evolution and the fast catalytic deactivation in favor of H_2O reduction significantly limit the potential for large-scale applications.[12,13]

The electrocatalytic reduction of CO_2 is a complex reaction process with various adsorbed intermediates (such as COOH$^•$ and CO$^•$) and the binding strength of intermediates on the catalyst surface plays a key role in the formation of final products.[14–17] Recently, bimetallic alloy electrocatalysts has attracted considerable attention as an alternatively promising approach for dramatically improving the catalytic activity and selectivity of CO_2 reduction.[18–24] Alloying two metals alters the binding strength of intermediates on the catalyst surface in the reduction of CO_2 due to electronic effect and geometric effect.[19,25] Density functional theory (DFT) has been utilized for calculating the binding energy of multiple intermediates on various alloys, giving a theoretical basis for developing suitable bimetallic alloy catalysts with high catalytic activity for a desired product.[14,15,26,16]

Experimentally, it has been demonstrated that the interaction of the two different metal atoms in a bimetallic alloy could significantly influence the catalytic activity and selectivity in the electroreduction of CO_2. Recently, Koper *et al.*[27] reported that bimetallic Pd-Pt alloy nanoparticles exhibit a very low onset potential for the reduction of CO2 to HCOOH of ~ 0 V vs. the reversible hydrogen electrode (RHE) and a high faradaic efficiency (FE) of 88% for HCOOH formation at -0.4 V vs. RHE. In addition, Takanabe *et al.*[18] discovered that a nanostructured Cu-In bimetallic alloy prepared by the in situ electrochemical reduction of Cu_2O in $InSO_4$ electrolytes is able to reduce CO_2 to CO with a FE of 85% at -0.6 V vs. RHE. Furthermore, the dramatically improved FE for the reduction of CO_2 to CO has also been achieved on nanostructured Cu-Sn and Cu-Pd bimetallic catalysts at reduced

overpotentials.[20,28] While impressive progress has been made on the improvement of the catalytic activity and selectivity for the reduction of CO_2 on alloy catalysts, the fundamental understanding of the correlation of the composition of bimetallic catalysts with the catalytic activity remains unclear. This discrepancy largely comes from the fact that mostly studied catalysts for CO_2 reduction are nanostructured materials, which make it difficult to distinguish the effects of bimetallic composition and surface morphology (each of which can contribute to altered CO_2 reduction performance).

Au is the most active metal electrocatalysts for the reduction of CO_2 to CO, however, the catalytic activity on Au is still limited by the activation of CO_2 to stabilize $COOH^{\bullet}$.[17] In contrast, Pt provides favorable activation and conversion of CO_2 to adsorbed CO (limiting step is CO desorption).[17] Herein, we present the first exploration of the electrocatalytic reduction of CO_2 on Au-Pt bimetallic thin films with controllable compositions and planar morphology. These bimetallic planar films provide an ideal platform for investigating the electronic effect on the binding strength of intermediates and the formation of final products by tuning the composition of bimetallic catalysts while keeping the surface morphology consistent. A systematic experimental and theoretical investigation elaborates the mechanism of the effect of binary catalyst composition on the catalytic activity and selectivity of CO_2 reduction, revealing an important correlation of the electronic structure of the alloys with the binding strength of reaction intermediates that determines the final product distribution.

4.2 Experimental section

4.2.1 Fabrication and characterization of bimetallic Au-Pt films

For obtaining high purity Au-Pt bimetallic films, Au-Pt films were deposited by a magnetron sputtering co-deposition technique (separated targets) at an argon pressure of 0.3 Pa, as shown in figure S4.1. In this co-deposition process, the deposition rates of the two target materials (Au and Pt) were manipulated by adjusting the deposition power, respectively, for synthesizing the controllable compositions of binary metals. The composition of binary films will be hereafter expressed by the atomic ratio of Au and Pt ($Au_{100-n}Pt_n$, $0 \leq n \leq 100$). In

addition, the thickness of the Au-Pt films were controlled by deposition time, and the cross-sectional scanning electron microscopy (SEM) image (Figure S4.3) indicates that the Au-Pt binary electrocatalyst was comprised of ~ 60-70 nm thick film.
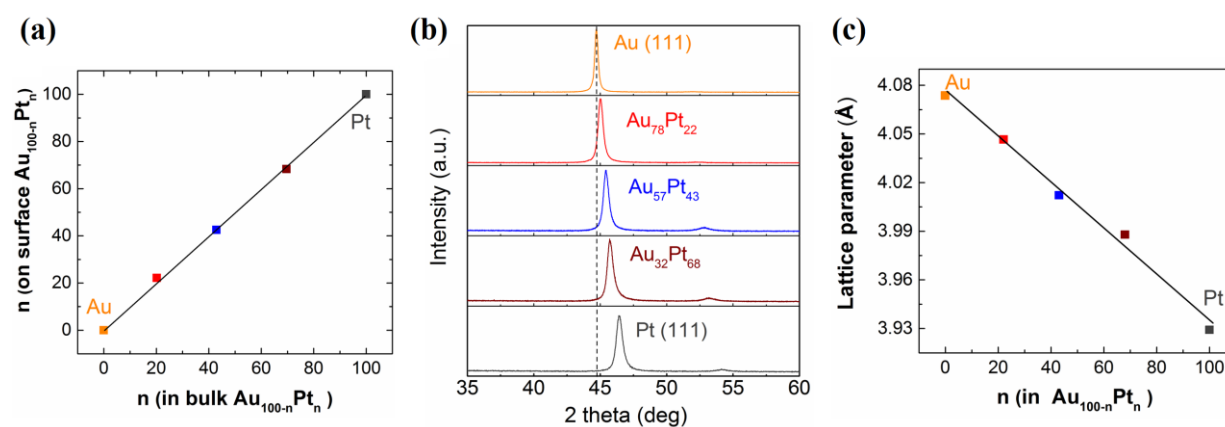
Figure 4.1 Characterization of Au-Pt bimetallic films. (a) A comparison of surface composition with bulk composition of AuPt film measured by XPS and EDS, respectively. (b) XRD patterns of pure Au (orange line), pure Pt (gray line) and $Au_{100-n}Pt_n$ bimetallic films. (c) Variation of the lattice parameter of the Au-Pt bimetallic alloys as a function of the Pt content.

To confirm the surface composition of the deposited Au-Pt bimetallic films, X-ray photoelectron spectroscopy (XPS) measurements were performed. It was found that the surface atomic ratio of Au to Pt in the Au-Pt bimetallic film was tuned by altering the deposition rate of magnetron sputtering (Table S4.1). It has been reported that Au could segregate to the surface of binary films, which is caused by the low surface free energy of Au, resulting in slightly enriched Au in binary film.[29] Here, the bulk composition (Table S4.2) of the deposited Au-Pt bimetallic films were characterized by Energy-dispersive X-ray spectroscopy (EDS). The comparison of the bulk and surface composition of binary films is presented in Figure 4.1a, which reveals the bulk composition of the Au-Pt binary films was consistently identical to the surface composition of the films, indicating no obvious Au segregation at the surface of the binary films prepared by magnetron sputtering. The observation of no Au segregation at the surface is consistent with the previous work on Au-Pt bimetallic films fabricated using pulsed laser deposition.[30] Importantly, the surface composition of the Au-Pt films was maintained even after 2 hours of electrolysis (Table S4.3).

X-ray diffraction (XRD) measurements were conducted for verifying the formation of the Au-Pt alloys. As noted in the XRD patterns (Figure 4.1b), all compositions of the samples exhibited only one dominant diffraction peak which can be assigned to the diffraction of the (111) plane from the fcc crystal structure and the (111) peak position gradually shifted to larger 2θ with an increase of Pt content, indicating the formation of the Au-Pt bimetallic alloys.[29] The shift of the (111) peak towards larger 2θ with increasing Pt content is attributed to the reduced lattice parameter of Au-Pt alloy caused by the incorporation of Pt (the lattice parameter of the alloy is between the pure Au and Pure Pt). Here, the lattice parameter of Au-Pt alloys (Table S4.4) was extracted according to the XRD patterns and Bragg's law (Equation S4.1). A plot of the lattice parameter as a function of Pt content in the Au-Pt bimetallic films is displayed in Figure 4.1c, which includes the lattice parameter of pure Au (0.40736 nm) and pure Pt (0.39290 nm) for comparison. A linear relationship between lattice parameter and the Pt content of Au-Pt films was observed (Figure 4.1c), which is the typical characteristic of alloying based on Vegard's law.[30,31] These results indicate that Au-Pt alloys were formed over the whole composition range without Au segregation at the surface.

4.2.2 Electrocatalytic CO$_2$ reduction activity

The electrochemical reduction of CO$_2$ on the Au-Pt bimetallic films with different compositions were performed in a CO$_2$-saturated 0.1 M KHCO$_3$ (99.95%) electrolyte (pH = 6.83) at room temperature and atmospheric pressure. The CO$_2$ electroreduction was conducted in an electrochemical cell, which is separated into working and counter electrode compartments by a Nafion-115 proton exchange membrane for preventing the oxidation of the CO$_2$ reduction products. The cathodic compartment was continuously purged with CO$_2$ at a constant flow rate, venting directly into the gas-sampling loop of a gas chromatograph (GC) for periodically quantifying the gas-phase products. To analyze liquid products produced in the CO$_2$ reduction, the CO$_2$ reduction electrolyte was collected after completion of the electrolysis experiments and then detected by ^{1}H nuclear magnetic resonance (NMR).[32]

4.3 Results and discussion

The comparison of the electrocatalytic activity of the Au-Pt bimetallic alloys with different compositions is presented in Figure 4.2. CO and H_2 were detected as the major products of CO_2 reduction on these Au-Pt bimetallic alloys (Figure 4.2). At a fixed potential of 0.65 V vs. RHE, CO formation was not detected on pure Pt, and the highest CO faradaic efficiency of ~77% was observed on pure Au. Interestingly, the Au-Pt bimetallic alloys exhibited a gradually enhanced FE for CO formation as the Au content increased, simultaneously accompanying with decreased FE for H_2 evolution, which reveals that the syngas ratio (CO:H_2) could be tailored in the electroreduction of CO_2 at a fixed potential by systematically tuning the composition of the Au-Pt bimetallic films.
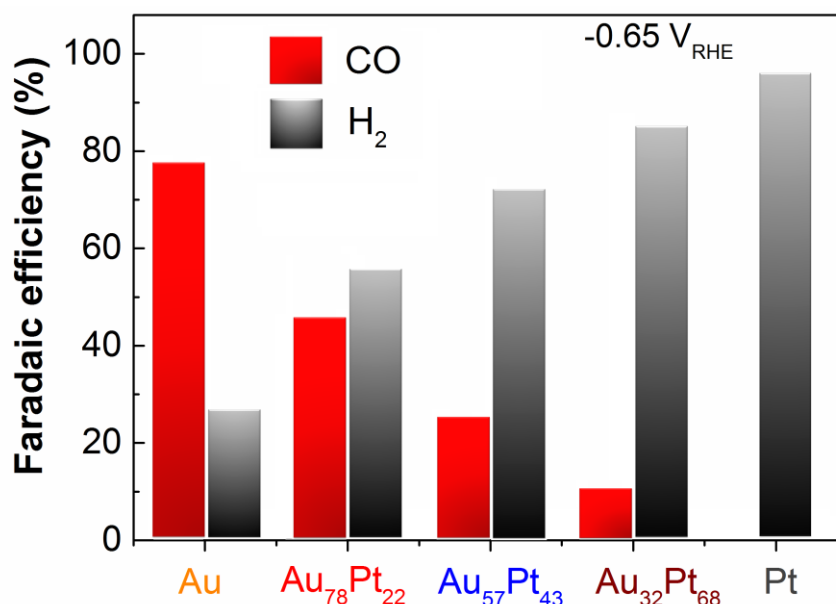
Figure 4.2 Faradaic efficiency for CO on Au-Pt bimetallic alloys with different compositions at 0.65 V versus RHE in CO_2-saturated 0.1 M $KHCO_3$ electrolyte (pH= 6.8).
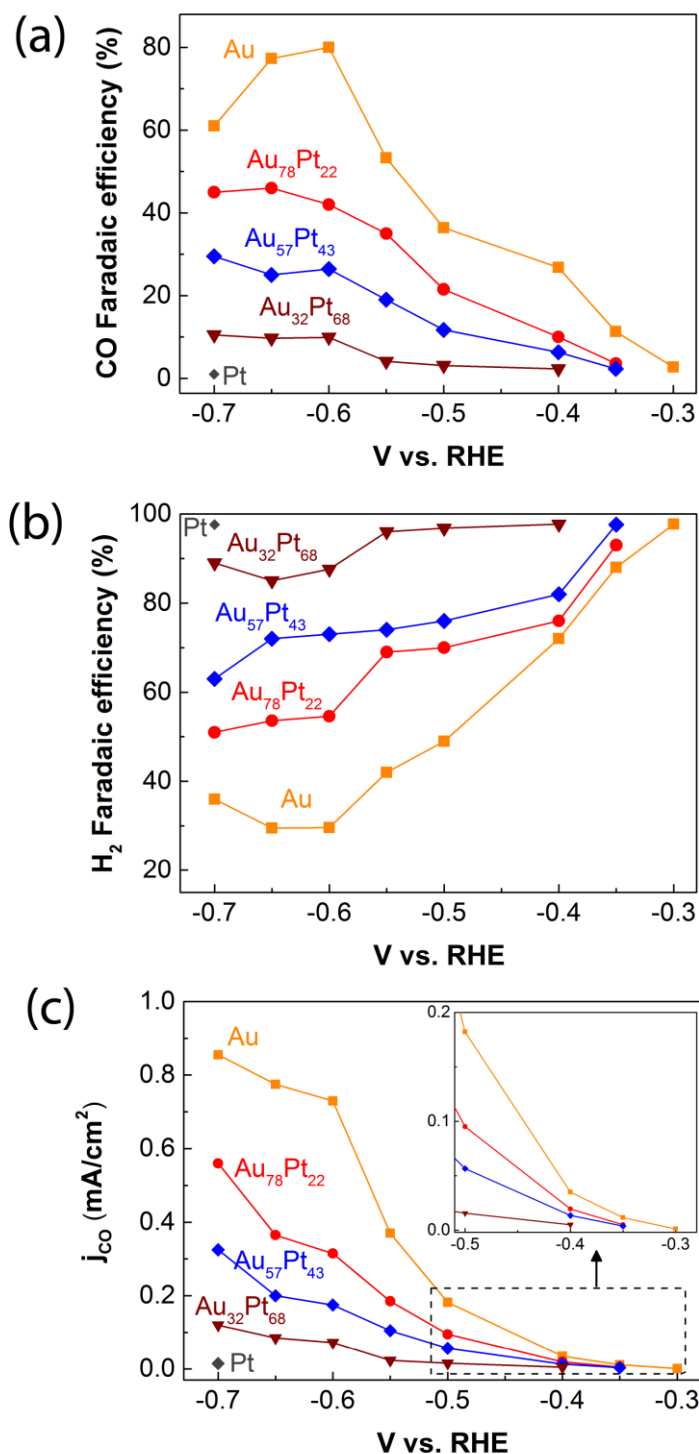
Figure 4.3 Comparison of the electrocatalytic performance of AuPt bimetallic alloys with different compositions. Faradaic efficiency for CO (a) and H_2 (b) on AuPt bimetallic alloys with different compositions at various potentials in CO_2-saturated 0.1 M $KHCO_3$ electrolyte (pH= 6.8). (c) Partial current density for CO at various potentials. No detected CO formation on Pt film.

To gain a deeper understanding of the trend of the electrocatalytic activity of CO_2 reduction on Au-Pt alloys with different compositions, the FE for the major products was plotted at various potentials (Figure 4.3). With increasing overpotentials, the Au-Pt bimetallic catalysts with various compositions all experienced a gradually increased FE for the reduction of CO_2 to CO, while the peak FE for CO on pure Au was achieved at -0.6 V vs. RHE and then a gradual decease in the FE for CO was detected with further increasing overpotentials. In addition, the opposite tendency in FE for CO and H_2 was also observed on the Au-Pt bimetallic films with different compositions at various potentials. As displayed in Figure 4.3a and 3b, the increase in the FE for CO formation followed the correspondingly reduced FE for H_2 evolution with increasing Au incorporation at various potentials. In this study, during the various potential tests for CO_2 reduction, CO formation on Pt was only detected at 0.7 V vs. RHE with a very low FE of 1%, and the CO formation on $Au_{32}Pt_{68}$, $Au_{57}Pt_{43}$ and pure Au was able to be detected at 0.4 V, 0.35 and 0.3 V vs. RHE, respectively, which implies the decreased overpotential for the reduction of CO_2 to CO with increasing Au content of Au-Pt bimetallic catalysts (Figure 4.3a). Furthermore, a plot of the partial current density for CO formation as a function of potential in Figure 4.3c also reveals a positive shift for the onset potential in the reduction of CO_2 to CO with incorporating more Au into binary films. These results indicate that the catalytic activity for the reduction of CO_2 to CO and the competing H_2 evolution can be tuned on the Au-Pt bimetallic films by systematically controlling the atomic ratio of Au/Pt.

In addition to the observed major products, formate was also detected as a liquid product. As presented in Figure 4.4, the formation of HCOOH (FE of 1.4%) started to be detected on pure Au at -0.6 V vs. RHE, and at a less negative potential of -0.55 V vs. RHE, a FE of 2% for HCOOH was observed on $Au_{78}Pt_{22}$ (Figure 4.4). Notably, for driving the electrocatalytic reduction of CO_2 to HCOOH, a potential of -0.5 vs. RHE was required on the $Au_{57}Pt_{43}$, which is a positive shift of 100 mV and 50 mV in comparison with pure Au and $Au_{78}Pt_{22}$, respectively. These findings imply that the Pt content (<50 at.%) in Au-Pt bimetallic catalysts may facilitate the electrocatalytic reduction of CO_2 to HCOOH formation at a reduced overpotential. With further increasing the Pt composition, the potential required for driving the reduction of CO_2 to HCOOH formation shifted back to a more negative potential (0.6 V and 0.65 V vs. RHE were required for $Au_{32}Pt_{68}$ and Pt, respectively). All the above results indicate the catalytic activity and selectivity for CO_2 reduction is strongly linked to the composition of the Au-Pt bimetallic alloys.
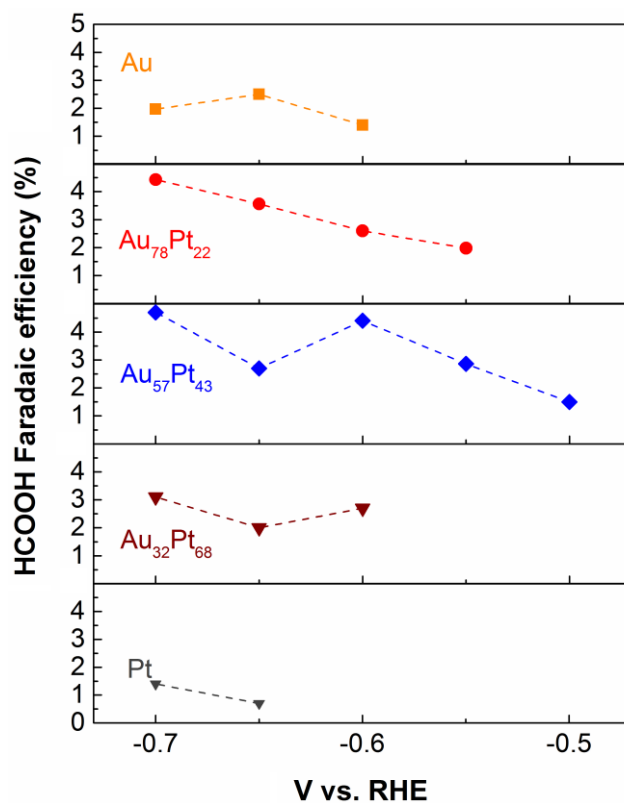
Figure 4.4 Faradaic efficiency for HCOOH formation at various potentials in CO_2-saturated 0.1 M $KHCO_3$ electrolyte.

To gain further insights into the influence of the binary composition on the catalytic activity of CO_2 reduction, it is critical to distinguish the electronic effect and the geometric effect.[19,25] The electronic effect is linked to the change of electronic structure that is tuned with surface composition of bimetallic catalysts, which results in the variation of the binding strength of intermediates. In addition, the geometric effect that is correlated with the atomic arrangement at the active site which has a significant influence on the interaction between adsorbed species and the surface atoms.[19] In our study, the surface roughness was analyzed by atomic force microscopy (Figure S4.5, all films on polished Si substrates had a roughness of 0.3 - 0.5 nm), showing magnetron sputtering is able to deposit uniform flat surface layer for all different compositional alloys, which implies that the variation of the catalytic activity with changing the bimetallic composition should be only related to the surface electronic effect.
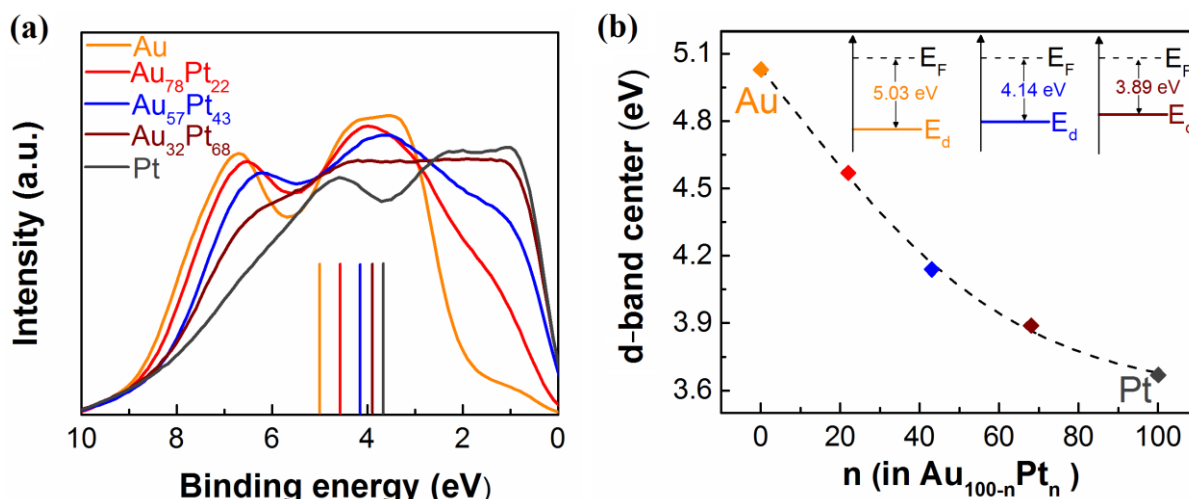
Figure 4.5 Electronic properties of Au-Pt bimetallic films. (a) Comparison of surface valence band XPS spectra of Au-Pt bimetallic films with different composition (the binding energy is the value of $|E-E_F|$). The color line in the center represents the position of d-band center of the corresponding Au-Pt film. (b) Energy of d-band center as a function of Pt content. The inset shows the d-band center (E_d) position of Au and Au-Pt alloys with respect to the Fermi level.

For the effect of the electronic properties on the catalytic activity and selectivity, d-states (that are close to the Fermi level) of transition metals play an important role in the binding strength of adsorbed species on the surface.[25,31,33] The higher energy of d-states leads to the stronger interaction with adsorbed intermediates.[33] Thus, alloying two metals may alter the average energy of the d-electrons of the catalyst surface, which is correlated with the variation of the binding strength of intermediates, leading to the change of catalytic activity and selectivity. Of particular note, it has been reported that value of d-band center can be used to represent the average energy of the d-electrons.[33]

In order to reveal the variation of the average energy of the d-electrons with the bimetallic composition, high-resolution surface valence band XPS measurements were performed on Au-Pt bimetallic films. The surface valence band XPS spectra as a function of composition of the Au-Pt bimetallic films is presented in Figure 4.5a. The position of the d-band center of Au-Pt bimetallic films was determined according to Equation S4.2, and was labeled with colored vertical lines in Figure 4.5a, which indicates an obvious change of the d-band center with different atomic ratios of Au/Pt. The energy of the d-band center as a function of Pt content shown in Figure 4.5b implies that pure Pt has the closest d-band center (E_d=3.67 eV)

relative to the Fermi level (E_F). Notably, the d-band center of Au-Pt bimetallic films was shifted away from the Fermi level (E_F) with gradually increasing Au content, correspondingly weakening the binding strength of intermediates on the surface, which is consistent with the reported bimetallic Au-Pt alloys.[31]
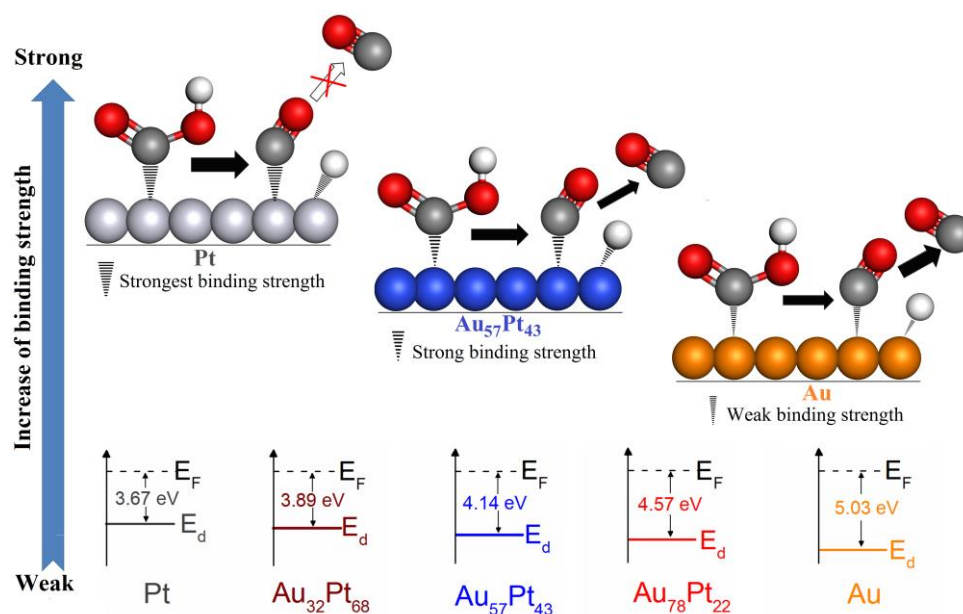
Figure 4.6 Schematic illustration of binding strength of COOH, CO and H intermediates on Au-Pt bimetallic catalysts as a function of the d-band center position.

Based on the catalytic CO_2 reduction performance of Au-Pt bimetallic films, we propose a mechanism to correlate the binding strength of COOH, CO and H intermediates on Au-Pt bimetallic films with the d-band center position relative to the Fermi level, as displayed in Figure 4.6. For Pt, the E_d is very lose to E_F (3.67 eV), which corresponds to the strongest binding strength of COOH$^\bullet$ and CO$^\bullet$, indicating that the CO_2 activation for stabilizing COOH$^\bullet$ intermediate and the formation of adsorbed CO are facile. However, the desorption of CO from the surface is limited due to the strongest binding strength of CO on Pt (Figure 4.6), which corresponds to the very low catalytic activity for the reduction of CO_2 to CO (Figure 4.3a). This result is consistent with DFT simulation work for CO_2 reduction on Pt.[17] With increasing Au composition of Au-Pt bimetallic films, the E_d moves away from E_F by getting more d-electrons from Au,[31] which reduces the binding strength of COOH$^\bullet$ and CO$^\bullet$ with gradually increasing Au content, resulting in gradually increased catalytic conversion of CO_2 to CO. The highest value of E_d (5.03 eV) was detected on pure Au, which offers weaker

binding strength for COOH$^\bullet$ and CO$^\bullet$, which is the optimum binding strength among transition metals for the reduction of CO$_2$ to CO,[17] corresponding to highest catalytic activity for CO$_2$ reduction to CO.

The above discussion indicates that the binding strength at a mixed site is the average of the properties of the constituents, which likely implies that the binding strength for intermediates on the Au-Pt bimetallic films are correlated linearly with each other with tuning the binary composition, corresponding to the gradually enhanced catalytic activity for the reduction CO$_2$ to CO with increasing the Au content.

The binding energies of the reaction intermediates on Au-Pt bimetallic surface were further investigated by DFT simulation.[17] The binding energies of COOH and CO intermediates on the Au-Pt alloys are shown in Figure 4.7a together with the rate of CO$_2$ reduction to CO based on a previously published micro-kinetic model.[17] According to this model, optimum activity for CO production is obtained for appropriate binding energies of COOH$^\bullet$ and CO$^\bullet$, which simultaneously allow facile CO$_2$ activation and CO release. The catalytic activity on late transition metal and coinage metal surfaces is limited by a correlation between COOH$^\bullet$ and CO$^\bullet$ binding energies. The Au-Pt alloys studied here follow the same correlation between COOH$^\bullet$ and CO$^\bullet$ binding energies as discovered previously.[17] In addition, the variation in catalyst activity for CO production is linked to the change of hydrogen binding energy that is responsible for H$_2$ production,[34] due to a correlation between CO$^\bullet$ and H$^\bullet$ binding energies as presented in Figure 4.7b. Furthermore, the variation of electronic properties on bimetallic surfaces are induced by strain and ligand effects.[35] We find no correlation between alloy lattice constants and binding energies of COOH$^\bullet$, CO$^\bullet$, H$^\bullet$ on Au-Pt alloy (Figure S4.6). However, the electronic ligand effect plays a significant role, which may lead to Au atoms in Au-Pt alloys binding intermediates stronger than pure Au and Pt binding intermediates weaker than pure Pt, implying that the binding energies of intermediates on the Au-Pt alloy films lie in between pure Pt and pure Au. This result is consistent with our experimental work (the binding strength at a mixed site is the average of the properties of the constituents). In addition, the shift of the d-band center away from the Fermi level with increasing Au composition is also found from DFT calculation (Figure S4.7).
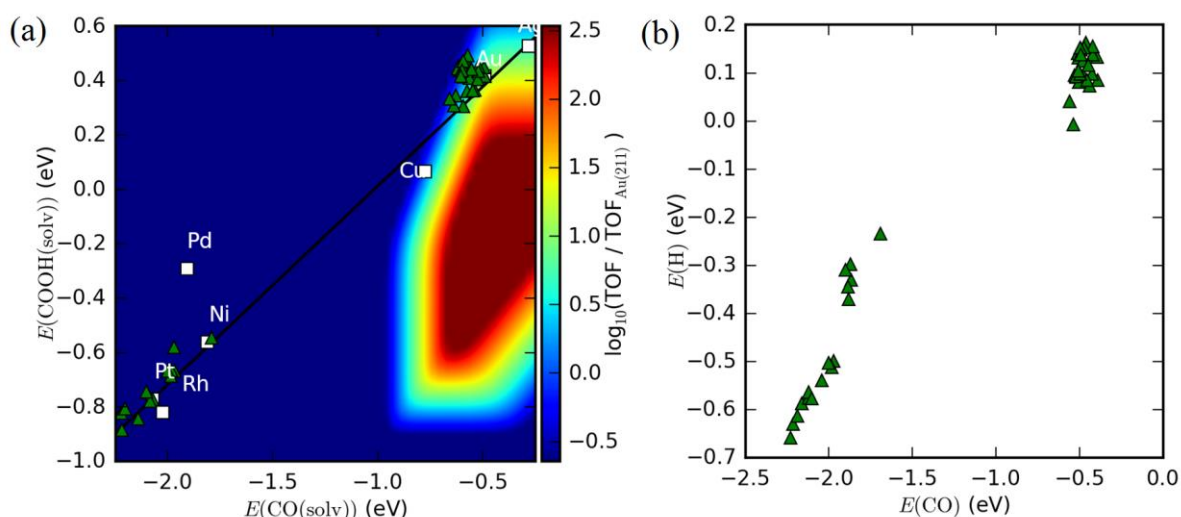
Figure 4.7 (a) COOH and CO binding energies of Au-Pt (211) steps calculated from DFT shown over an activity map for CO production. (b) Correlation of CO and H binding energies on Au-Pt (211) steps.

This exploration of the electronic effect on the catalytic activity for CO_2 reduction in the bimetallic system suggests that the binding strength for intermediates on Au-Pt bimetallic films likely follows the scaling relation, which is also in agreement with the previous DFT simulation work for Au-Pd alloy surfaces (a linear relationship is obtained between the adsorption strength of intermediates and the composition of alloy).[25] In addition, it was reported that although the dramatically improved FE for the reduction of CO_2 to CO is achieved on nanostructured Cu-In and Cu-Sn bimetallic catalysts at the reduced overpotentials, In and Sn deposited on flat Cu catalysts experienced a predominant H_2 evolution under similar conditions.[18,20] The significantly improved catalytic activity for CO_2 reduction only observed on the nanostructured Cu-In and Cu-Sn bimetallic surfaces is mainly ascribed to the synergistic geometric and electronic effects. It has been demonstrated that the geometric effect which could lead catalysts to deviate from the scaling relation has a significant effect on the adsorption of intermediates.[19,25] Thereby, it seems that a solely electronic effect of bimetallic alloys may not be enough to significantly break the scaling relation for dramatically improving the electrocatalytic reduction of CO_2. The atomic arrangement (nanostructure) should be also considered to design a bimetallic catalyst for the electroreduction of CO_2, which may be attributed to the synergistic geometric and electronic effects that contributes to the high-performance of bimetallic catalysts.

4.4 Conclusions

In summary, Au-Pt bimetallic thin films with tunable compositions were prepared with a uniform morphology, offering a platform for understanding the electronic effect on the catalytic activity for CO_2 reduction in a bimetallic system. The Au-Pt binary films exhibited a gradually improved catalytic activity for the reduction of CO_2 to CO with increasing the Au content, which is attributed to the variation of electronic properties caused by changing binary composition. We show that the d-band center was gradually shifted away from the Fermi level with increasing the Au content, which weakens the binding strength of $COOH^\bullet$ and $CO^\bullet$, resulting in the corresponding variation in catalytic activity for CO_2 reduction. In addition, with increasing the Au composition, the binding strength of intermediates on the Au-Pt bimetallic films may still follow the scaling relation, which reveals that electronic effect alone in bimetallic catalysts is likely unable to break the scaling relation to freely tune the binding strength of a certain intermediate without affecting others for achieving a high CO_2 reduction performance. This study shows that a single electronic effect in bimetallic system could not reduce the required overpotential for the dramatically improved catalytic activity for CO_2 reduction to CO, and the atomic arrangement also needs to be taken into account to design a bimetallic catalyst for driving highly selective and efficient CO_2 reduction to CO at the reduced overpotential. In addition, this study does not contain more complicated intermediates and reaction pathways which are involved in hydrocarbon formations, thus systematic studies of bimetallic films with a fixed morphology are still needed to determine the role of the electronic effect on the catalytic activity and selectivity for CO_2 electroreduction to more complex products.

References

[1]   D. T. Whipple, P. J. a. Kenis, *J. Phys. Chem. Lett.* **2010**, *1*, 3451–3458.

[2]   K. P. Kuhl, T. Hatsukade, E. R. Cave, D. N. Abram, J. Kibsgaard, T. F. Jaramillo, *J. Am. Chem. Soc.* **2014**, *136*, 14107–14113.

[3]   J. Qiao, Y. Liu, F. Hong, J. Zhang, *Chem. Soc. Rev.* **2014**, *43*, 631–675.

[4]   N. Kornienko, Y. Zhao, C. S. Kley, C. Zhu, D. Kim, S. Lin, C. J. Chang, O. M. Yaghi, P. Yang, *J. Am. Chem. Soc.* **2015**, *137*, 14129–14135.

[5]   M. Ma, K. Djanashvili, W. A. Smith, *Angew. Chemie Int. Ed.* **2016**, *55*, 6680–6684.

[6]   R. Kas, K. K. Hummadi, R. Kortlever, P. de Wit, A. Milbrat, M. W. J. Luiten-Olieman, N. E. Benes, M. T. M. Koper, G. Mul, *Nat. Commun.* **2016**, *7*, 10748.

[7]   M. Mikkelsen, M. Jørgensen, F. C. Krebs, *Energy Environ. Sci.* **2010**, *3*, 43–81.

[8]   M. Gattrell, N. Gupta, A. Co, *J. Electroanal. Chem.* **2006**, *594*, 1–19.

[9]   K. P. Kuhl, E. R. Cave, D. N. Abram, T. F. Jaramillo, *Energy Environ. Sci.* **2012**, *5*, 7050–7059.

[10]   Y. Hori, R. Takahashi, Y. Yoshinami, A. Murata, *J. Phys. Chem. B* **1997**, *101*, 7075–7081.

[11]   Y. Hori, in *Electrochem. CO2 Reduct. Met. Electrodes* (Ed.: E. Vayenas, C. G., White, R. E., Gamboa-Aldeco, M. E.), Springer New York, **2008**, p. Vol. 42, p 89.

[12]   Y. Chen, C. W. Li, M. W. Kanan, *J. Am. Chem. Soc.* **2012**, *134*, 19969–19972.

[13]   C. W. Li, M. W. Kanan, *J. Am. Chem. Soc.* **2012**, *134*, 7231–7234.

[14]   A. A. Peterson, J. K. Nørskov, *J. Phys. Chem. Lett.* **2012**, *3*, 251–258.

[15]   P. Hirunsit, W. Soodsawang, J. Limtrakul, *J. Phys. Chem. C* **2015**, *119*, 8238–8249.

[16]   H. A. Hansen, C. Shi, A. C. Lausche, A. A. Peterson, J. K. Nørskov, *Phys. Chem. Chem. Phys.* **2016**, *18*, 9194–9201.

[17]   H. A. Hansen, J. B. Varley, A. A. Peterson, J. K. Nørskov, *J. Phys. Chem. Lett.* **2013**, *4*,

388–392.

[18] S. Rasul, D. H. Anjum, A. Jedidi, Y. Minenkov, L. Cavallo, K. Takanabe, *Angew. Chemie Int. Ed.* **2015**, *54*, 2146–2150.

[19] D. Kim, J. Resasco, Y. Yu, A. M. Asiri, P. Yang, *Nat. Commun.* **2014**, *5*, 4948.

[20] S. Sarfraz, A. T. Garcia-Esparza, A. Jedidi, L. Cavallo, K. Takanabe, *ACS Catal.* **2016**, *6*, 2842–2851.

[21] Y. Zhao, C. Wang, G. G. Wallace, *J. Mater. Chem. A* **2016**, *4*, 10710–10718.

[22] M. Li, J. Wang, P. Li, K. Chang, C. Li, T. Wang, B. Jiang, H. Zhang, H. Liu, Y. Yamauchi, et al., *J. Mater. Chem. A* **2016**, *4*, 4776–4782.

[23] Z. Yin, D. Gao, S. Yao, B. Zhao, F. Cai, L. Lin, P. Tang, P. Zhai, G. Wang, D. Ma, et al., *Nano Energy* **2016**, *27*, 35–43.

[24] D. A. Torelli, S. A. Francis, J. C. Crompton, A. Javier, J. R. Thompson, B. S. Brunschwig, M. P. Soriaga, N. S. Lewis, *ACS Catal.* **2016**, *6*, 2100–2104.

[25] P. Liu, J. K. Nørskov, *Phys. Chem. Chem. Phys.* **2001**, *3*, 3814–3818.

[26] J. Ko, B.-K. Kim, J. W. Han, *J. Phys. Chem. C* **2016**, *120*, 3438–3447.

[27] R. Kortlever, I. Peters, S. Koper, M. T. M. Koper, *ACS Catal.* **2015**, *5*, 3916–3923.

[28] M. Li, J. Wang, P. Li, K. Chang, C. Li, T. Wang, B. Jiang, H. Zhang, H. Liu, Y. Yamauchi, et al., *J. Mater. Chem. A* **2016**, *4*, 4776–4782.

[29] C. Hahn, D. N. Abram, H. A. Hansen, T. Hatsukade, A. Jackson, N. C. Johnson, T. R. Hellstern, K. P. Kuhl, E. R. Cave, J. T. Feaster, et al., *J. Mater. Chem. A* **2015**, *3*, 20185–20194.

[30] E. Irissou, F. Laplante, S. Garbarino, M. Chaker, D. Guay, *J. Phys. Chem. C* **2010**, *114*, 2192–2199.

[31] F. Chang, S. Shan, V. Petkov, Z. Skeete, A. Lu, J. Ravid, J. Wu, J. Luo, G. Yu, Y. Ren, et al., *J. Am. Chem. Soc.* **2016**, *138*, 12166–12175.

[32] M. Ma, K. Djanashvili, W. A. Smith, *Phys. Chem. Chem. Phys.* **2015**, *17*, 20861–

20867.

[33]   J. K. Nørskov, T. Bligaard, J. Rossmeisl, C. H. Christensen, *Nat. Chem.* **2009**, *1*, 37–46.

[34]   J. K. Nørskov, T. Bligaard, A. Logadottir, J. R. Kitchin, J. G. Chen, S. Pandelov, U. Stimming, *J. Electrochem. Soc.* **2005**, *152*, 23–26.

[35]   J. R. Kitchin, J. K. Nørskov, M. A. Barteau, J. G. Chen, *Phys. Rev. Lett.* **2004**, *93*, 156801.

[36]   T. P. Dirkse, *Electrochim. Acta* **1990**, *35*, 1445–1449.

[37]   J. M. M. Droog, F. Huisman, *J. Electroanal. Chem. Interfacial Electrochem.* **1980**, *115*, 211–224.

[38]   Y. Hori, A. Murata, R. Takahashi, *J. Chem. Soc. Faraday Trans. 1 Phys. Chem. Condens. Phases* **1989**, *85*, 2309.

Supplementary information for Chapter 4

Materials

0.1 M KHCO$_3$ (Sigma Aldrich, ≥99.95%) was made from de-ionized water with resistivity of 18.2 MΩ cm from Milli-Q$^®$ Integral unltrapure water (Merck Millipore), and directly used in this study without any purification. The Ti foils (Sigma Aldrich ,99.7%, 0.25 mm thick) and Si (n-type, phosphorus doping, one-side polished, (100)-oriented, resistivity 5~10 Ω cm) were ultrasonically cleaned in acetone and ethanol, and subsequently dried with nitrogen.

Fabrication of Au-Pt alloy with sputtering

Au-Pt alloys films were prepared on flat Ti foils by a co-deposition, which consists of a radio frequency (RF) magnetron sputtering from pure Pt target (MaTecK GmbH, 99.99%) and a direct current (DC) magnetron sputtering from pure Au target (MaTecK GmbH, 99.99%). Figure S4.1 shows a typical schematic illustration of magnetron sputtering with co-deposition technique under an argon (Ar) ambient. Ar$^+$ bombardment takes place on a target (cathode) due to the energetic Ar$^+$ ions generated in a glow discharge plasma, and the bombardment process leads to the removal of target atoms, which condenses on a substrate to form a thin film.
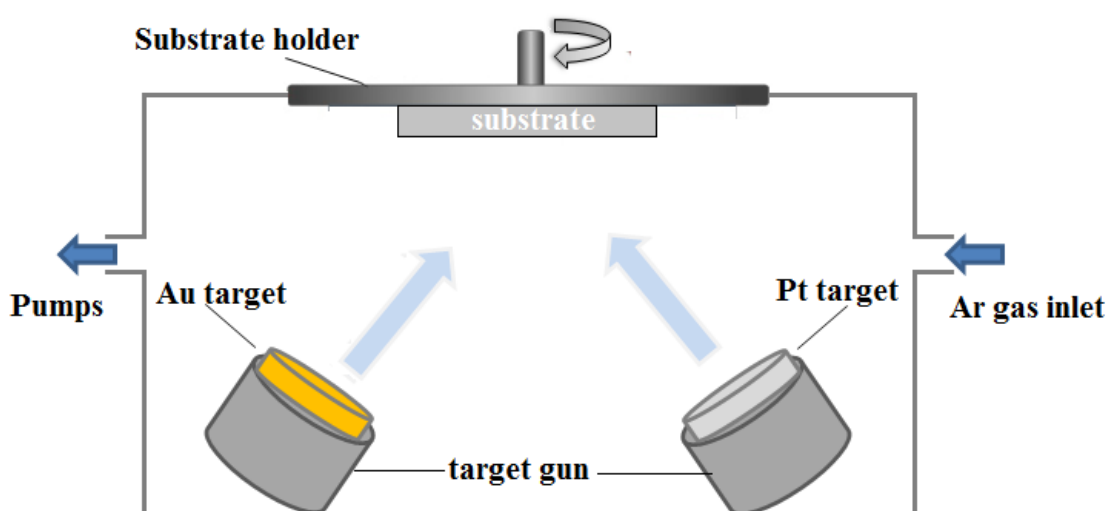
Figure S4.1 Schematic illustration of the magnetron sputtering co-deposition with Au and Pt targets.
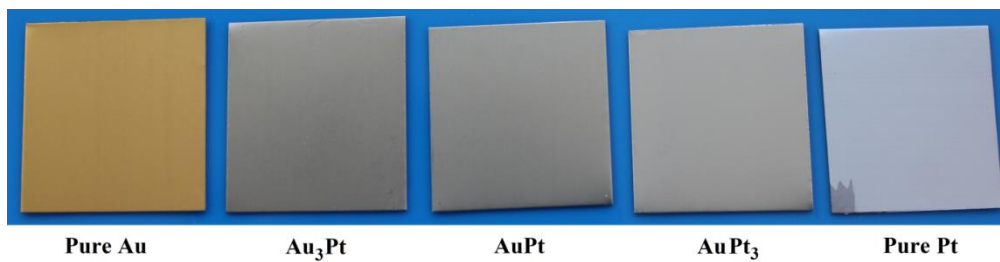
Figure S4.2 Digital pictures of the Au-Pt samples fabricated by magnetron sputtering.
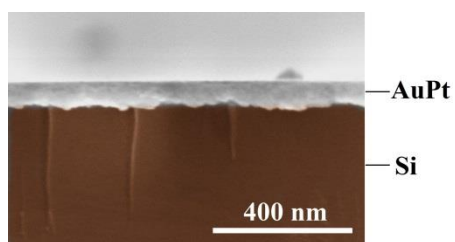
Figure S4.3 Cross-sectional SEM image of Au-Pt bimetallic film fabricated by magnetron sputtering.

Composition of Au-Pt bimetallic films

The surface and bulk composition of the Au-Pt alloys were detected by X-ray photoelectron spectroscopy (XPS, Thermo Scientific™ K-Alpha™) and Energy-dispersive X-ray spectroscopy (EDS, JEOL JSM-6010LA), respectively.

Table S4.1 The surface Au/Pt atomic ratio determined by XPS analysis.

Atomic ratio	Au (at. %)	Pt (at.%)
Pure Au		
AuPt sample 1	77.88%	22.12%
AuPt sample 2	57.49%	42.51%
AuPt sample 3	31.75%	68.25%
Pure Pt		

Table S4.2 The bulk compositions (at. %) of the Au-Pt alloys measured from EDS analysis.

Atomic ratio	Au (at. %)	Pt (at.%)
Pure Au		
AuPt sample 1	79.81 %	20.19%
AuPt sample 2	57.06%	42.94%
AuPt sample 3	30.34%	69.66%
Pure Pt		

Table S4.3 The surface Au/Pt atomic ratio from XPS analysis after CO_2 electrolysis.

Atomic ratio	Au (at. %)	Pt (at.%)
Pure Au		
AuPt sample 1	77.59%	22.41%
AuPt sample 2	57.58%	42.42%
AuPt sample 3	31.67%	68.33%
Pure Pt		

XPS spectra of Au-Pt bimetallic films
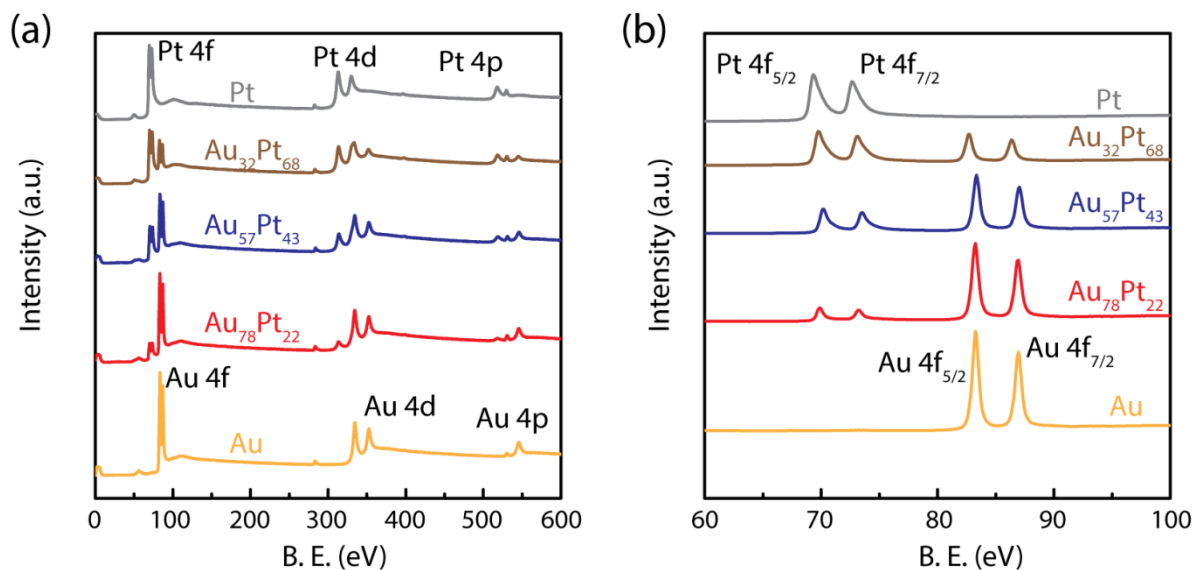
Figure S4.4 XPS spectra of Au-Pt bimetallic films with different composition at the binding energy range of 0 ~ 500 eV (a) and 60 ~100 eV, respectively.

Electrochemical characterization and product analysis

CO_2 reduction electrolysis was performed in an customized electrochemical cell which consists of two compartments (working and counter electrode compartments) separated by a proton exchange membrane (Nafion-115) with a three electrode configuration at room temperature and atmospheric pressure. In the three-electrode configuration measurement, platinum gauze (Alfa Aesar, 99.9%, 25x312.5 mm, 52 mesh woven from 0.1mm dia wire) and An Ag/AgCl electrode (XR300, saturated KCl + AgCl solution (KS120), Radiometer Analytical) were used as the counter electrode and the reference electrode, respectively. In addition, the both compartments were filled with a CO_2-saturated 0.1 M $KHCO_3$ (pH = 6.83) electrolyte, with continuously purging with CO_2 at a constant flow rate.

During the electrolysis, gas chromatograph (GC, Interscience) equipped with two thermal conductivity detectors (TCD) was used to periodically detect CO and H_2 generated in CO_2 reduction. In addition, liquid products was analyzed by nuclear magnetic resonance (NMR) after completion of the electrolysis. An Agilent MR400DD2 NMR spectrometer operating at 400 MHz was used for the measurement, and the detailed measurement process has been reported in our previous work.[1,2]

Surface roughness

The surface roughness of Au-Pt bimetallic films deposited on polished Si substrates by magnetron sputtering were characterized with atomic force microscopy (AFM, commercial Dimension Icon AFM, Bruker) operating in tapping mode in air. Analysis of AFM images was done with Scanning Probe Image Processor software (SPIPTM, Image Metrology ApS).
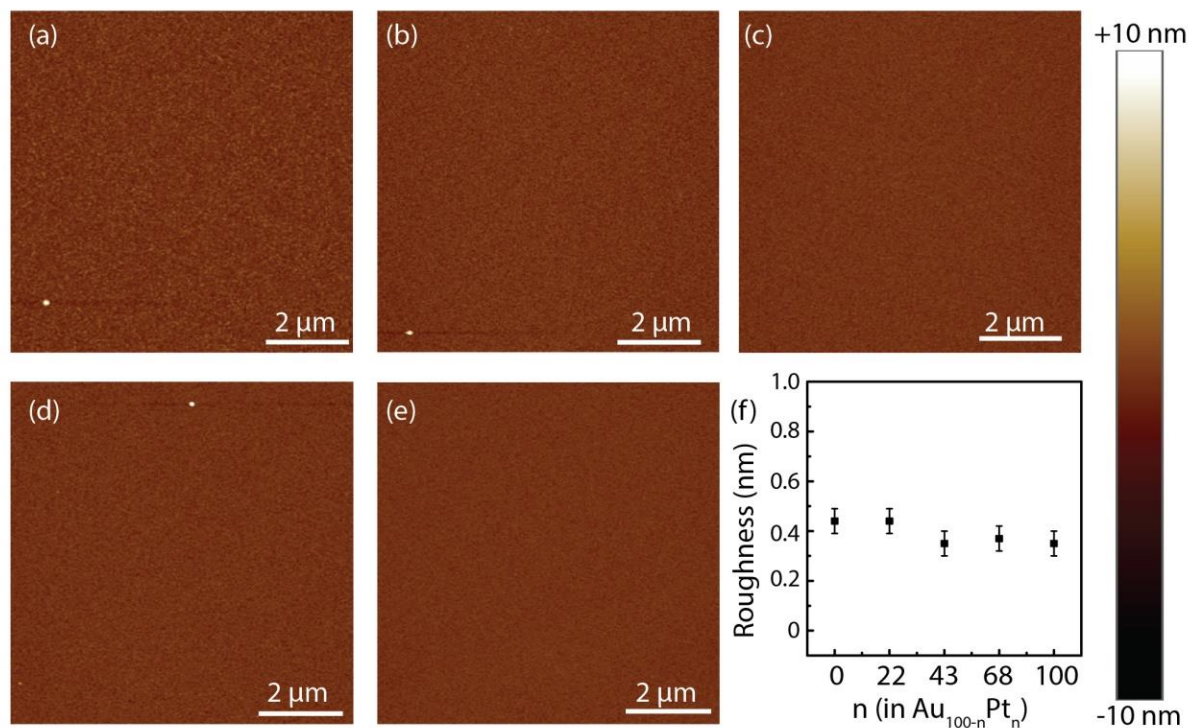
Figure S4.5 AFM images of Au (a), $Au_{78}Pt_{22}$ (b), $Au_{57}Pt_{43}$ (c), $Au_{32}Pt_{68}$ (d) and Pt (e) on polished Si substrates. (f) Surface roughness of the Au-Pt bimetallic alloys with different compositions measured by AFM (the root mean square average (RMS) of height deviation taken from the mean image data plane was used to denote the surface roughness).

Lattice parameter calculation

From the bragg's law and the crystal face (111), the lattice parameter of FCC structure of the Au-Pt bimetallic alloys can be expressed as:

$$a = \frac{\sqrt{3}\lambda_{cobalt}}{2\sin\theta}$$ (S4.1)

where, λ_{cobalt} is 0.178897 nm. θ is the angle between the incident X-ray and the scattering planes.

Table S4.4 The calculated lattice parameter of FCC structure of pure Au, Pt and Au-Pt bimetallic alloy.

Sample	2θ (deg) for (111) Crystal face	Lattice parameter (Å)
Pure Au	44.708	4.07357
Au$_{78}$Pt$_{22}$ alloy	45.022	4.0466
Au$_{57}$Pt$_{43}$ alloy	45.429	4.01226
Au$_{32}$Pt$_{68}$ alloy	45.713	3.988
Pure Pt	46.447	3.92904

d-band center determination

The d-band center determination of surface valence band XPS measurements were performed with a Thermo Scientific K-alpha apparatus using an Al K-ray source and a flood Gun. 50 scans in the valence band binding energy range (0-30 eV) were carried out with a spot size of 400 μm, pass energy of 50 eV, dwell time of 50 ms and a step size of 0.1 eV. For comparison of all valence band XPS spectra, the background was subtracted. The position of the d-band center (E$_d$), equation can be calculated by equation[3,4]

$$E_d = \frac{\int N(\varepsilon)\varepsilon d\varepsilon}{\int N(\varepsilon)d\varepsilon}$$ (S4.2)

where, E$_d$ is the energy of d-band center, and N(ε) is the density of state. For the integration, the range of the binding energy was fixed from 0 to 9.0 eV.[3,4]

Computational details

Density functional theory calculations are performed using the Dacapo DFT code with the ASE package.[5] Ionic cores are described using Vanderbilt ultrasoft pseudopotentials and the Kohn-Sham wavefunctions are expanded in planewaves with kinetic energy below 340 eV, while the electron density is expanded in planewaves with a cutoff corresponding to 500 eV.[6] Effects of exchange and correlation are approximated by the RPBE functional.[7] The catalyst surface is modeled using slabs oriented in the (211) direction with 10 (211) layers corresponding to about 3 closepacked (111) layers. The bottom 6 layers are fixed in the bulk fcc position with a lattice parameter obtained from Vegard's law and the topmost 4 layers and any adsorbate are optimized until the maximum force component is below 0.03 eV/Å.

Periodically repeated slabs are separated by at least 15 Å of vacuum and the dipole correction have been applied to remove the electrostatic dipole interaction between repeated slabs.[8] A rectangular surface cell with 3 step atoms is used and the first Brilluin zone is sampled using a (4,4,1) Monkhorst-Pack grid of special k-points.[9]

Adsorbate formation energies are here reported as the reaction energies of the reactions

$$CO_2(g) + \tfrac{1}{2} H_2(g) \rightarrow COOH^\bullet \qquad\qquad (S4.3)$$

$$CO^\bullet \rightarrow CO(g) + {}^\bullet \qquad\qquad (S4.4)$$

$$\tfrac{1}{2} H_2(g) + {}^\bullet \rightarrow H^\bullet \qquad\qquad (S4.5)$$

Where $^\bullet$ denotes a step site on the catalyst. A + 0.45 eV destabilization of the CO_2 molecule is applied to correct for systematic errors with the RPBE functional, and $COOH^\bullet$ and $CO^\bullet$ is corrected by 0.25 eV and 0.1 eV respectively to account for stabilization due to solvation from hydrogen binding from the aqueous electrolyte.[10]

Surfaces are constructed with lattice constants corresponding to bulk compositions

Au, $Au_{78}Pt_{22}$, $Au_{75}Pt_{25}$, $Au_{57}Pt_{43}$, $Au_{50}Pt_{50}$, $Au_{32}Pt_{68}$, $Au_{25}Pt_{75}$, and Pt. Due to the limited size of the slab model containing a total of 30 atoms, actual compositions realized in the simulations are, however, Au, $Au_{77}Pt_{23}$, $Au_{77}Pt_{23}$, $Au_{57}Pt_{43}$, $Au_{50}Pt_{50}$, $Au_{33}Pt_{67}$, $Au_{27}Pt_{73}$, and Pt.
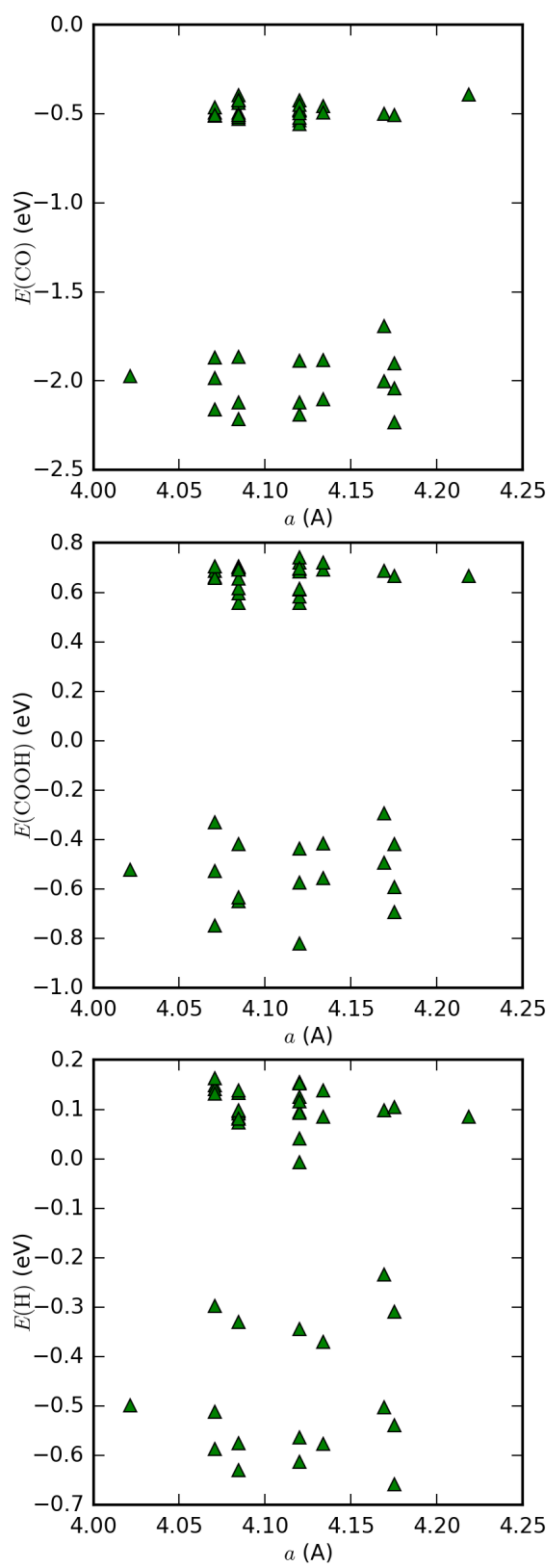
Figure S4.6 Scatter plots of binding energies of CO, COOH and H on PtAu(211) alloys versus the lattice parameter.
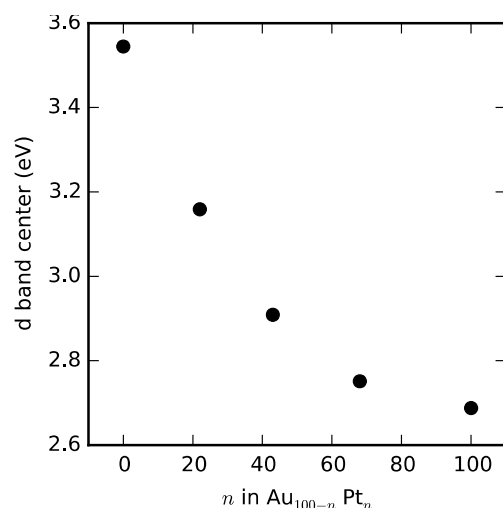
Figure S4.7 Distance from the d band center to the Fermi level obtained by projected density of states from DFT model surfaces.

References

[1]   M. Ma, K. Djanashvili, W. A. Smith, *Phys. Chem. Chem. Phys.* **2015**, *17*, 20861–20867.

[2]   M. Ma, K. Djanashvili, W. A. Smith, *Angew. Chemie Int. Ed.* **2016**, *55*, 6680–6684.

[3]   G.-R. Zhang, D. Zhao, Y.-Y. Feng, B. Zhang, D. S. Su, G. Liu, B.-Q. Xu, *ACS Nano* **2012**, *6*, 2226–2236.

[4]   D. Kim, J. Resasco, Y. Yu, A. M. Asiri, P. Yang, *Nat. Commun.* **2014**, *5*, 4948.

[5]   ASE and Dacapo are open source codes available at wiki.fysik.dtu.dk.

[6]   D. Vanderbilt, *Phys. Rev. B* **1990**, *41*, 7892–7895.

[7]   B. Hammer, L. Hansen, J. K. Nørskov, *Phys. Rev. B* **1999**, *59*, 7413–7421.

[8]   L. Bengtsson, *Phys. Rev. B* **1999**, *59*, 12301–12304.

[9]   H. J. Monkhorst, J. D. Pack, *Phys. Rev. B* **1976**, *13*, 5188–5192.

[10]   A. a. Peterson, F. Abild-Pedersen, F. Studt, J. Rossmeisl, J. K. Nørskov, *Energy Environ. Sci.* **2010**, *3*, 1311.

5. Summary and Outlook

The electrocatalytic conversion of CO_2 into fuel and valuable chemicals by coupling with a renewable electricity source is a promising strategy for closing the anthropogenic carbon cycle. The critical step for achieving this practical CO_2 utilization is to find a suitable electrocatalyst that is capable of reducing CO_2 in a cost-effective process with high efficiency, stability and selectivity for a desired product.

We developed a simple and scalable method for synthesizing Cu nanowire (NW) arrays, which were prepared through a two-step fabrication of $Cu(OH)_2$ NW arrays and CuO NW arrays on Cu foils and a subsequent electroreduction of CuO NW arrays to Cu NW arrays. The Cu NW arrays were utilized for the electrocatalytic reduction of CO_2. In the first part of the chapter 2, the Cu NW arrays with fixed NW length and density as a function of potential was studied, discovering that Cu NW array electrodes are capable of catalytically reducing CO_2 to CO and HCOOH with selectivity of ~ 50% and ~ 30%, respectively, at an applied potential of -0.6 V vs. RHE, which are much higher in comparison with polycrystalline Cu. The high catalytic activity for the reduction of CO_2 may be due to the more active sites on the high surface area of Cu NW, and the enhanced catalytic selectivity for the conversion of CO_2 into CO on Cu NW arrays is attributed that the fast initial electron transfer for CO_2 activation step on Cu NW arrays.

At more negative potentials, hydrocarbon gas phase products were detected from the electroreduction of CO_2 on Cu NW arrays. In the second part of chapter 2, the effect of Cu nanowires morphology on the catalytic selectivity of hydrocarbon formation were explored by systematically varying the nanowire length and density of Cu NW arrays. The catalytic selectivity for hydrocarbon products at a fixed potential can be tuned through systematically controlling the length and density of Cu NW. On the Cu nanowire length ($\geq 2.4 \pm 0.56$ µm), the formation of n-propanol was detected along with CO, HCOOH and C_2H_4. With further increasing the length of Cu nanowire ($\geq 7.3 \pm 1.3$ µm), C_2H_6 was observed on Cu NW arrays, accompanying with the formation of ethanol. The formation of C_2H_6 has never been reported for the electroreduction of CO_2 on polycrystalline Cu. We propose a possible pathway for C_2H_6 from the intermediate (CH_3CH_2O) in the CO dimerization pathway. Interestingly, an

enhancement in the selectivity for C_2H_4 formation was presented with increasing the Cu nanowire length and density, which is linked to an enhanced local pH in the Cu nanowire arrays that contributes to the formation of C_2H_4 through a CO coupling mechanism. Thus, the selectivity for the conversion of CO_2 into hydrocarbons could be tuned on Cu nanowire arrays by tailoring the Cu nanowire morphology, which offers a promising way for systematically controlling the formation of hydrocarbons through the electrocatalytic reduction of CO_2.

Ag is also a highly interesting metal catalyst in the field of CO_2 reduction due to its high selectivity for the electrochemical conversion of CO_2 into CO. In this thesis, nanostructured Ag catalysts were prepared by the electrochemical reduction of Ag_2O layers which was formed by pulsed potential anodization of Ag electrodes in alkaline solutions. The oxide-derived nanostructured Ag catalysts were investigated for the electrocatalytic reduction of CO_2, revealing that the high catalytic selectivity for the reduction of CO_2 to CO was shifted by more than 400 mV towards a lower overpotential compared to untreated Ag. Notably, nanostructured Ag synthesized from Ag oxide is capable of electrochemically converting CO_2 into CO with ~80% catalytic selectivity at a moderate overpotential of 0.49 V, which is dramatically higher than the untreated Ag under identical conditions. Electrokinetic studies indicate that the improved catalytic activity and selectivity for the reduction of CO_2 to CO is likely correlated with an enhanced stabilization for $COOH^\bullet$ intermediate (CO_2 activation) on the highly active sites of the oxide-derived nanostructured Ag. In addition, we proposed a local pH effect for the catalytic activity of the reduction of CO_2 on oxide-derived nanostructured metallic catalysts. The porous-like nanostructured Ag hinders the neutralization reaction for OH^- generated near catalyst surface due to the limitation of the diffusion process, which results in a high local pH within the porous-like nanostructured Ag, likely playing a significant role in the improved catalytic activity of the reduction of CO_2 along with suppressed H_2 evolution.

The formation and adsorption of intermediates on catalyst surfaces play a significant role in the catalytic activity for CO_2 reduction. Alloying two different metals is able to change the binding energies of intermediates that are related to the formation of final products in the CO_2 reduction reaction. In this thesis, Au-Pt bimetallic thin films were synthesized with tunable compositions (uniform morphology), which offers a platform for investigating the binary composition effect on the catalytic activity for CO_2 reduction in a bimetallic system. A gradual rise of syngas ratio ($CO:H_2$) in the reduction of CO_2 was observed with increasing the Au content. This variation of catalytic activity is strongly linked to the changed electronic

properties caused by tuning binary composition. With increasing the Au content, the d-band center was gradually shifted away from the Fermi level, which gradually reduces the binding strength of $COOH^\bullet$ and $CO^\bullet$, correspondingly enhancing catalytic activity for the reduction of CO_2 to CO. The binding strength of intermediates followed the scaling relation with binary compositions, indicating that electronic effect alone in bimetallic catalysts may be unable to freely vary the binding strength of certain intermediates without influencing others for achieving a high catalytic performance in CO_2 reduction. The geometric effect (atomic arrangement) also should be taken into account for developing a bimetallic catalyst that can drive highly selective and efficient CO_2 reduction to CO.

Overall, nanostructured metal catalysts were prepared for the electrochemical reduction of CO_2, and a fundamental understanding of the local environment effect in highly nanostructured surfaces was demonstrated in this thesis. In addition, this thesis also presents a well-defined platform for a better understanding of the correlation between CO_2 reduction activity and binary composition of a catalyst.

For commercial electrochemical CO_2 conversion, it is essential to fulfill the following requirements: high selectivity for desired products, low overpotential needed for driving this reaction and long-term stability. Thus, further improved nanostructured catalysts are highly significant for approaching this target. This thesis offers a local environment effect on the detailed reaction mechanism in nanostructured surfaces, and further investigation of CO_2 reduction mechanism has to be continued. A deeper understanding of reaction mechanism could help to rationally design high-performance nanostructured electrocatalysts for practical application of CO_2 reduction. In addition, the catalytic performance of nanostructured catalysts may be further improved by the strategy of alloying two elements (bimetallic surfaces). Furthermore, gas diffusion cells should be utilized by combining with highly active nanostructured catalysts to achieve high current densities, which can dramatically enhance the reaction rate.

Samenvatting en vooruitzicht

De elektrokatalytische conversie van CO_2 naar brandstoffen en waardevolle chemicaliën door deze te koppelen met een duurzame elektriciteitsbron is een veelbelovende strategie om de antropogene koolstofcyclus te kunnen sluiten. De meest kritische stap om praktisch CO_2 gebruik haalbaar te maken is het vinden van een geschikte elektrokatalysator die CO_2 op een kosteneffectieve manier kan reduceren met een hoge efficiëntie, selectiviteit en stabiliteit.

Wij hebben een simpele en schaalbare methode ontwikkeld om Cu nanodraden (NWs) te produceren. Deze werden gemaakt middels een 2-stap fabricage waarbij eerst ofwel $Cu(OH)_2$ NWs ofwel CuO NWs op Cu folie werden gevormd en vervolgens een elektroreductie stap van CuO NWs naar Cu NWs werd uitgevoerd. De Cu NWs werden gebruikt voor de elektroreductie van CO_2. In het eerste deel van hoofdstuk 2 zijn Cu NWs van een vaste lengte en dichtheid bestudeerd als functie van de aangelegde spanning. Hierbij werd ontdekt dat Cu NWs CO_2 katalytisch kunnen reduceren naar CO en HCOOH met een selectiviteit van respectievelijk ~50% en ~30% bij een aangelegde spanning van -0.6 V vs. RHE, dit is een veel hogere selectiviteit in vergelijking met polykristallijn koper. De hoge katalytische activiteit voor de reductie van CO_2 zou veroorzaakt kunnen worden doordat er meer actieve atoom posities te vinden zijn op het vergrote oppervlak van Cu NWs ten opzichte van polykristallijn koper. De verbeterde selectiviteit voor de conversie naar CO is toe te schrijven aan de snelle initiële elektron overdracht als activatie stap van de CO_2 reductie.

Bij negatievere aangelegde spanningen werden er ook koolwaterstoffen in de gasfase waargenomen uit de reductie van CO_2 aan Cu NWs. In de tweede helft van hoofdstuk 2 is het effect van de morfologie van Cu NWs op de katalytische selectiviteit van koolwaterstof vorming uitgezocht door systematisch de lengte en dichtheid van de NWs te variëren. De katalytische selectiviteit voor gasvormige koolwaterstoffen bij een vaste aangelegde spanning kan worden afgestemd door systematisch de lengte en dichtheid van Cu NWs te controleren. Bij een NW lengte groter of gelijk aan 2.4 ± 0.56 µm werd n-propanol gevormd naast CO, HCOOH en C_2H_4. Bij langere Cu NWs ($\geq$ 7.3 ± 1.3 µm), werden C_2H_6 en ethanol gevormd. De vorming van C_2H_6 was nooit eerder gerapporteerd als product van de elektrokatalytische reductie van CO_2 aan polykristallijn Cu. Wij presenteren een mogelijk reactie mechanisme voor de vorming van C_2H_6 uit de intermediair CH_3CH_2O in het CO-dimerisatie mechanisme.

Belangwekkend genoeg is dat een verbetering in de selectiviteit voor C_2H_4 werd gevonden bij de verlenging en verdichting van de Cu NWs. Dit wordt toegeschreven aan een verhoogde lokale pH tussen de Cu NWs die bijdragen aan de vorming van C_2H_4 middels een CO koppelmechanisme. Oftewel: men kan de selectiviteit voor de conversie van CO_2 naar koolwaterstoffen afstemmen door de morfologie van de Cu NWs te manipuleren, dit biedt een veelbelovende route voor het systematisch controleren van de vorming van koolwaterstoffen door de elektrokatalytische reductie van CO_2.

Zilver is ook een zeer interessant metaal als katalysator voor CO_2 reductie dankzij zijn hoge selectiviteit voor de elektrochemische conversie van CO_2 naar CO. In deze thesis zijn nanogestructureerde Ag katalysators gemaakt middels de elektrochemische reductie van lagen van Ag_2O die worden gevormd door gepulseerde spanningsanodisatie van Ag elektrodes in basische oplossing. De oxide afgeleide nanogestructureerde Ag katalysators werden onderzocht voor de reductie van CO_2. Dit leverde een hoge selectiviteit en een reductie van ruim 400 mV in benodigde aangelegde spanning op ten opzichte van onbehandeld Ag voor de reductie van CO_2 naar CO. Opmerkelijk genoeg kan nanogestructureerd Ag, wanneer gemaakt uit zilver oxide, CO_2 met 80% efficiëntie omzetten in CO bij de zeer gematigde aangelegde spanning van 0.49 V. Deze efficiëntie is veel hoger dan voor onbehandeld zilver onder dezelfde condities. Elektrokinetische studies wijzen erop dat de verbeterede katalytische activiteit en selectiviteit voor de reductie van CO_2 naar CO zeer waarschijnlijk te correleren vallen met een verbeterde stabilisatie van het $COOH^{\bullet}$ intermediair (CO_2 activatie) op de zeer actieve atoom posities van het oxide afgeleide Ag. Ook stellen wij dat er een lokaal pH effect optreedt bij de reductie van CO_2 aan nanogestructureerde metaal katalysators. Het poreuze nanogestuctureerde Ag hindert de neutralisatie reactie van OH^- ionen die gevormd zijn aan het katalysator oppervlak als gevolg van een gehinderde diffusie. Dit resulteert in een hoge lokale pH binnen het poreuze nanogestructureerde Ag, dit speelt waarschijnlijk een belangrijke rol in de verbeterde katalytische activiteit van de reductie van CO_2 in combinatie met een onderdrukte H_2 formatie.

De vorming en adsorptie van intermediairen aan de katalysator oppervlakte spelen een belangrijke rol in de katalytische activiteit voor CO_2 reductie. Het legeren van twee verschillende metalen kan de bindingsenergie van CO_2 reductie intermediairen veranderen. In deze thesis werden er Au-Pt intermetallische dunne films gemaakt met aanpasbare compositie (van uniforme morfologie). Deze dunne films bieden een platform om het effect van binaire composities op de katalytische activiteit voor CO_2 reductie te testen. Een geleidelijke stijging

van de syngas ratio (CO:H$_2$) als product van CO$_2$ reductie werd geobserveerd wanneer het Au gehalte van de dunne films werd vergroot. Deze variatie in katalytische activiteit is sterk gelieerd aan de veranderende elektronische eigenschappen van de intermetallische katalysator als functie van de compositie. Door het vergroten van het Au gehalte schuift het d-band centrum geleidelijk weg van het Fermi niveau, dit reduceert de bindingsenergie voor COOH$^\bullet$ en CO$^\bullet$ geleidelijk, waardoor de katalytische activiteit voor CO$_2$ reductie wordt vergroot. De bindingsenergie van intermediairen volgt waarschijnlijk de gewogen relatie van binaire composities, wat betekent dat het elektronische effect op zichzelf niet genoeg is om vrijelijk de bindingsenergie van bepaalde intermediairen te veranderen zonder daarbij andere intermediairen ook te veranderen. Het geometrische effect (atomische reorganisatie) zou ook meegenomen moeten worden wanneer men een intermetallische katalysator zou willen ontwikkelen die een zeer selectieve en efficiënte reductie van CO$_2$ naar CO behaalt.

In deze thesis zijn nanogestructureerde metaal katalysators gemaakt voor de elektrochemische reductie van CO$_2$ naar CO, hierbij is een fundamenteel begrip van het lokaal pH effect in zeer nanogestructureerde oppervlaktes gedemonstreerd. Verder presenteert deze thesis ook een goed gedefinieerd platform voor een beter begrip van de korrelatie tussen CO$_2$ reductie activiteit en de binaire compositie van een katalysator.

Voor commerciële elektrochemische CO$_2$ conversie is het essentieel om aan de volgende eisen te voldoen: een hoge selectiviteit voor het beoogde product, een lage benodigde aangelegde spanning om deze reactie uit te voeren en stabiliteit op de lange termijn. Dus om dit doel te behalen zijn verder verbeterde nanogestructureerde katalysators zeer belangrijk. Deze thesis biedt met het directe omgeving effect (lokale pH) een verklaring voor het reactie mechanisme van nanogestructureerde katalysators maar verder onderzoek naar het CO$_2$ reductie mechanisme is nodig. Een groter begrip van het reactie mechanisme kan helpen bij een rationeel ontwerp van zeer goede nanogestructureerde katalysators voor praktisch haalbare CO$_2$ reductie. Verder kan de katalytische activiteit van nanogestructureerde katalysators mogelijk verder vergroot worden door het gebruik van intermetallische legeringen. Ook zouden gas diffusie cellen gebruikt moeten worden in combinatie met zeer actieve nanogestructureerde katalysators om een hogere stroom dichtheid te behalen; dit zou de reactiesnelheid enorm kunnen verbeteren.

Acknowledgements

My PhD study in the Netherlands will be the most memorable journey of my life which is filled with both pain and happiness. During this journey, there are many people who helped and supported me, contributing to the realization of this project. Without their assistance and support, I could not complete this work.

Initially, I would like to sincerely thank my daily supervisor **Dr. Wilson Smith** and promoter **Prof. dr. Bernard Dam**, who offered me the opportunity for pursuing my PhD degree in TU Delft. Half a year after coming to Delft, we started the new topic of CO_2 electroreduction, which was a completely new line of research within the group. There were so many challenges and difficulties at the beginning, and I even had doubts about the possibility of completing the project. Here, my great and heartfelt gratitude goes to **Wilson**, who guided me through this tough journey. Because of his excellent supervision, endless help and strong support, this project became possible. I really enjoy working with him due to his efficient way of working and enthusiasm about science. His rigorous requirements helped me unlock my potential, which makes me confident to confront more difficulties in the future. **Bernard**, I really appreciate him for giving many valuable suggestions and guidance during my PhD study. I'm truly grateful to him for the scientific questions he posed and fruitful discussions during our PEC meeting in the past three years.

I would like to express my sincere gratitude to the skillful technicians in our group, **Joost** and **Herman,** for their kind help and valuable technical support. With their help, the CO_2 reduction system was built, contributing to several excellent results that constructed this thesis. I am thankful to our very friendly group secretary, **Heleen**, for her kind assistance. I also would like to thank her for organizing some activities such as ice skating and Christmas dinner, which made MECS people get the chance to know each other more in addition to our academic life.

It is my great honor to work in the MECS with so many nice people. I would like to specially thank **Digda**, **Bartek** and **Moreno** for creating a happy atmosphere in our scientific life. There are so many unforgettable memories and funny stories we have made in the past few years. Thanks to them for always correcting my English pronunciations. Of course, many thanks to these guys for their help in my research, and in life. **Marco**, thanks for playing table

tennis with me, and I really enjoyed many amazing competitions with you at the basement of our old ChemE building. I also wish to thank **Prof. dr. Hans Geerlings**, **Prof. dr. Fokko Mulder** and **Prof. dr. Andreas Schmidt-Ott** for posing some questions which led to a lot of interesting discussions during our group meetings. Special thanks are also to **Nienke**, luckily who is not only a CO_2 reduction expert but also a Dutch girl, for translating the summary of my thesis into Dutch. My dear officemates: **Steffen** and **Divya**, thanks to them for creating a friendly office atmosphere with a lot of talks and discussion about science, politics and life. I also want to thank **Fahimeh** for plenty of fun talks we had in the past few years.

I am grateful to **Diana**, one of the former MECS members, who initially trained me how to operate the lab equipment when I just joined the group. There are some other former MECS members I wish to acknowledge. **David**, my former officemate, thanks to him for many helpful discussions about the CO_2 reduction field and sharing some Dutch culture with me. Dr. **Wim Haije**, I really like his humor and I would like to thank him for funny talks during our coffee break and borrel. **Kota**, a nice Japanese guy, we had a lot of interesting talks about China.

Through my PhD, I also would like to thank a lot of people outside MECS group. Particularly, I would like to thank **Dr. Kristina Djanashvili** for assistance in the NMR experiments and guidance in the related data analysis. For technical support, I also want to thank **Ben** and **Bart** for teaching me XRD measurement and discussing surface valence band XPS, respectively. Special thanks go to **Marcel** for teaching me AFM, and spending so much time in KPFM with me together.

Related to this thesis, I also would like to thank **all the committee members** for spending their precious time in reading and evaluating this thesis.

For studying in the Netherlands, I have to acknowledge the some important people in this journey. Special thanks to **Dr. Jianrong Gao** for introducing me to this fantastic country. I also would like to express my great thanks to my master supervisor, **Prof. dr. Qingzhong Xue**, who initially took me into this academia world. Thanks to him for ongoing help and encouragement thought my entire PhD study. Significant thanks to **Rui Kong** for her trust, support and encouragement at some difficult times during this journey. Many thanks go to my friend, **Srinath**, for his support and help during the most difficult moments at the beginning of my PhD journey. I also wish to thank **Richard** and **Jurgen** for their kind help.

A small Chinese community built at Delft brought me so much joy. I wish to deeply thank **Jicheng Feng**, **Kai Liu**, **Wuyuan Zhang**, **Yaolin Xu, Liangjun Yin, Liangyong Chu**, **Anping Cao**, **Xiaohui Sun**, **Meixian Shan, Kai Zhang, Zhen Liu, Yujie Zhao, Jing Guo, Riming Wang, Yiming Wang, Quan Pan and Jinyu Tang.** My flat mates, **Zhaolong Li** and **Beien Wang,** thanks to them for cooking for me. I also thank my old flat mates, **Zhi Zhou** and **Mubiao Xie**. Outside Delft, I also want to thank some other Chinese friends, **Shiqiang Zhang**, **Jie Xie, Huapeng Sui**, **Lin Xu, Yang Zhang**, **Yingchao Cui**, **Yonghui Li**, **Zhaochun Liu, Shengnan Lu, Bowen Wang and Yizhi Wu,** for all the joyful time we had together.

Most importantly, **my parents**, I miss them so much during this long-time PhD study overseas, really expecting a family reunion soon. Their unconditional love is always the source of my power. In this tough journey, they always strongly support and encourage me. There is no doubt that my family deserves my deepest gratitude and love.

Ming Ma (马明)

Department of Chemical Engineering,

Delft University of Technology

March, 2017

Publications

Peer-Reviewed Journals

1) **M. Ma**, B. J. Trześniewski, J. Xie, and W. A. Smith*, Selective and Efficient Reduction of CO_2 to CO on Oxide-Derived Nanostructured Ag Electrocatalysts, *Angew. Chem. Int. Ed.* 2016, 55 (33), 9748-9752.

2) **M. Ma,** K. Djanashvili, W. A. Smith*, Controllable Hydrocarbon Formation from the Electrochemical Reduction of CO_2 over Cu Nanowire Arrays, *Angew. Chem. Int. Ed.* 2016, 55(23), 6680–6684.

3) **M. Ma**, K. Djanashvili, W. A. Smith*, Selective Electrochemical Reduction of CO_2 to CO on CuO-derived Cu Nanowires, *Phys. Chem. Chem. Phys.* 2015, *17*, 20861–20867.

4) **M. Ma**, H. A. Hansen, M. Valenti, Z. Wang, A. Cao, M. Dong and W. A. Smith*, Correlation of CO_2 Reduction Activity and Selectivity with Compositionally Variant Bimetallic Electrocatalysts, 2017, Nano Energy (conditional acceptance).

5) I. A. Digdaya, P. P. Rodriguez, **M. Ma**, G. W. P. Adhyaksa, E. C. Garnett, A. H. M. Smets, W. A. Smith*, Engineering the kinetics and interfacial energetics of Ni/Ni–Mo catalyzed amorphous silicon carbide photocathodes in alkaline media, *J. Mater. Chem. A* 2016, 4, 6842-6852.

6) C. M. Caskey, J. A. Seabold, V. Stevanovic, **M. Ma**, W. A. Smith, D. S. Ginley, N. R. Neale, R. M. Richards, S. Lany and A. Zakutayev*, Semiconducting properties of spinel tin nitride and other IV_3N_4 polymorphs, *J. Mater. Chem. C*, 2015, 3, 1389-1396.

7) **M. Ma**, Q. Xue*, H. Chen, X. Zhou, D. Xia, C. Lv, and J. Xie, Photovoltaic characteristics of Pd doped amorphous carbon film/SiO_2/Si, *Appl. Phys. Lett.* 2010, 97, 061902.

8) **M. Ma**, Q. Xue*, J. Li, Y. Zhen, and S. Wang, Light-induced resistance effect of Pd doped carbon film/SiO_2/Si, *J. Appl. Phys.* 2011, 110, 054503.

9) Q. Xue, **M. Ma***, Y. Zhen, X. Zhou, S. Wang, Large photoconductivity of Pd doped amorphous carbon film/SiO_2/Si, *Diamond & Related Materials,* 2012, 21, 24.

10) C. Lv, Q. Xue*, D. Xia, **M. Ma**, Effect of chemisorption structure on the interfacial bonding characteristics of graphene-polymer composites, *Applied Surface Science,* 2012 258, 2077.

11) X. Zhou, Q. Xue*, **M. Ma** and J. Li, Effect of Si substrate on ethanol gas sensing properties of ZnO films, *Thin Solid Films*, 2011, 519, 6151.

12) X. Zhou, J. Li, **M. Ma** and Q. Xue[*], Effect of ethanol gas on the electrical properties of ZnO nanorods, *Physica E*, 2011, 43, 1056.

13) X. Zhou, **M. Ma**, Q. Xue*, Gas sensing properties of ZnO thin film/Si heterojunction to alcohols, *Materials Science Forum*, 2011, 687, 798.

14) H. Chen, Q. Xue[*], **M. Ma**, X. Zhou, Capacitive humidity sensor based on amorphous carbon film/n-Si heterojunctions, *Sensors & Actuators: B. Chemical*, 2010, 150, 487.

15) C. Lv, Q. Xue*, D. Xia, **M. Ma**, J. Xie, H. Chen, Effect of chemisorption on the interfacial bonding characteristics of graphene-polymer composites, *J. Phys. Chem. C*, 2010, 114, 6588.

16) J. Xie, Q. Xue*, H. Chen, D. Xia, C. Lv, and **M. Ma**, Influence of Solid Surface and Functional Group on the Collapse of Carbon Nanotubes, *J. Phys. Chem. C*, 2010, 114, 2100.

Patents

✧ Photovoltaic characteristics of Pd doped amorphous carbon film material. Q. Xue*, **M. Ma**, H. Chen, C. Lv, D. Xia. Application No: 201010140443.2 (China Patent).

✧ Hydrogen sensitivity of amorphous Pd/C/Si structure material. Q. Xue*, J. Li, H. Chen, **M. Ma**, X. Zhou, S. Wang. Application No: 201010287043.4 (China Patent).

✧ Photoconductivity of Pd doped amorphous carbon film/SiO$_2$/Si. S. Wang, Q. Xue*, **M. Ma**, Jianpeng Li, Yuhua Zhen. Application No: 201110095822.9 (China Patent).

Book Chapter

✧ **M. Ma** and W. A. Smith, Nanostructured Catalysts for the Electrochemical Reduction of CO$_2$, Anisotropic and Shape-Selective Nanomaterials, 337-373, Springer (2017).

Curriculum Vitae

Ming Ma (马明) was born on October 6, 1984 in Shandong Province, China. He received his Master degree in Materials Science and Engineering (MSc) in 2011 at China University of Petroleum. After that, he joined at Department of Applied Physics, Eindhoven University of Technology, working on CO_2 dissociation in a dielectric barrier discharge. In 2013, he started his research at Department of Chemical Engineering, Delft University of Technology, working under Dr. Wilson Smith and Prof. dr. Bernard Dam. He finished his PhD project on heterogeneous nanostructured catalysts for the electrochemical reduction of CO_2, including the fabrication, characterization, catalytic performance and reaction mechanism investigation of nanostructured metallic catalysts.